

Important Notice

This copy may be used only for the purposes of research and private study, and any use of the copy for a purpose other than research or private study may require the authorization of the copyright owner of the work in question. Responsibility regarding questions of copyright that may arise in the use of this copy is assumed by the recipient.

UNIVERSITY OF CALGARY

Novel orbital seismic sources at a CO₂ storage monitoring site, Newell County, Alberta

by

Tyler William Spackman

A THESIS

SUBMITTED TO THE FACULTY OF GRADUATE STUDIES
IN PARTIAL FULFILMENT OF THE REQUIREMENTS FOR THE
DEGREE OF MASTER OF SCIENCE

GRADUATE PROGRAM IN GEOLOGY AND GEOPHYSICS

CALGARY, ALBERTA

APRIL, 2019

© Tyler William Spackman 2019

Abstract

Time-lapse seismic surveys are often performed on large time scales and can suffer from repeatability problems arising from variations in source and receiver geometries. Novel orbital seismic sources have been developed and were permanently installed along with a permanent receiver array at a small carbon sequestration site in Newell County, Alberta. Baseline datasets encourage the use of these sources in conjunction with both geophone and fibre optic receivers by confirming the relationship between signal to noise ratio and source effort. Initial testing of the sources indicates promising transfer of the theoretical source signature through the subsurface to surface receivers. Due to the absence of a measurement of the true source signature, pre-processing workflows were developed incorporating pilot trace correlation and Gabor deconvolution. Resultant corridor stacks are comparable to baseline datasets. Testing of surface vibrator sources reveal severe issues with the current source deployment.

Acknowledgements

My sincerest gratitude goes to my supervisor, Don Lawton, for his guidance and mentorship, and for allowing me to be a part of such an exciting project. I have learned so much and have improved incredibly as a geoscientist because of his leadership.

I am grateful to Kevin Hall, Kevin Bertram, Malcolm Bertram, and Marie Macquet for making my experience in the field enjoyable, even when temperatures hit -40°C . For the safety of those around me, I will always remember to turn on the warning light when driving the Vibe truck.

I would like to thank my fellow CREWES students for making my grad school experience one to remember: Tim Cary, Matt Eaid, Adriana Gordon, Bobby Gunning, Scott Keating, Andrew Mills, and Eric Rops.

I thank the industrial sponsors of CREWES and of the CaMI FRS JIP for financial support of this work. I also thank the Government of Alberta and the Canadian Society of Exploration Geophysicists Foundation for additional support through scholarships.

I am extremely grateful to my family for their love and support throughout my studies.

Above all, my sincerest thanks to Sarah. Her unwavering support, love, understanding, and kind words have carried me through my studies. This journey would not have been possible without her by my side.

Table of Contents

Abstract.....	ii
Acknowledgements	iii
Table of Contents	iv
List of Tables	vi
List of Figures and Illustrations	vii
List of Symbols, Abbreviations and Nomenclature	xiv
Chapter 1 – Introduction	1
1.1 Project motivations	1
<i>1.1.1 Carbon capture and sequestration</i>	<i>2</i>
<i>1.1.2 Time-lapse seismic monitoring</i>	<i>3</i>
1.2 Containment and Monitoring Institute Field Research Station	7
1.3 Thesis objectives.....	9
1.4 Data used	9
<i>1.4.1 Well data.....</i>	<i>9</i>
<i>1.4.2 Seismic data.....</i>	<i>10</i>
1.5 Software used	10
Chapter 2 – Theory and State of the Art	11
2.1 Introduction.....	11
2.2 Seismic acquisition.....	11
2.3 SeisMovie	12
2.4 Orbital vibrators	15
<i>2.4.1 Theory.....</i>	<i>15</i>
<i>2.4.2 ACROSS system</i>	<i>20</i>
<i>2.4.3 Surface Orbital Vibrator: The Otway Project.....</i>	<i>22</i>
<i>2.4.4 GPUASA linear vibrators</i>	<i>25</i>
2.5 Distributed acoustic sensing.....	28
Chapter 3 –Source Installation	32
3.1 Introduction.....	32
3.1 Raytracing Experiment	32
<i>3.2.1 Impact on DAS.....</i>	<i>36</i>
3.3 Fluid Substitution	37
<i>3.3.1 Amplitude versus offset (AVO).....</i>	<i>39</i>
3.4 Synthetic Data	41
Chapter 4 – Baseline Data	49
4.1 Introduction.....	49
4.2 May 2017 2D Line	49
4.3 Baseline VSP.....	53
<i>4.3.1 Baseline geophone VSP</i>	<i>54</i>
<i>4.3.2 Baseline DAS VSP</i>	<i>59</i>
4.4 Implications for Permanent Sources.....	66

Chapter 5 – Results of Permanent Source Testing	70
5.1 Introduction.....	70
5.2 Borehole Linear Vibrator	70
5.3 Processing Considerations	76
<i>5.3.1 Correlation</i>	<i>77</i>
<i>5.3.2 Deconvolution</i>	<i>80</i>
<i>5.3.3 Source effort.....</i>	<i>86</i>
5.4 Surface Linear Vibrator.....	90
<i>5.4.1 Source accelerometer measurements</i>	<i>94</i>
Chapter 6 – Conclusions.....	104
6.1 Observations from Baseline Data	104
6.2 Permanent Source Results	105
6.3 Future Work.....	107
References	109

List of Tables

Table 1-1: Summary of seismic data used.	10
Table 2-1: GPUSA linear vibrator parameters.....	25
Table 5-1: Sweep parameters for borehole linear vibrator tests, September 2018	71
Table 5-2: Results of fitting quadratic models to pilot trace amplitude spectra of borehole linear vibrator tests.....	74
Table 5-3: Generalized sweep parameters for large surface linear vibrator source accelerometer tests.	95

List of Figures and Illustrations

Figure 1-1: IEA global policy scenarios and their impact on energy demand and CO ₂ emissions (from IEA, 2018).....	2
Figure 1-2: Contribution of various emissions reduction methods in IEA Sustainable Development Scenario versus New Policies Scenario (from IEA, 2018).....	3
Figure 1-3: Bulk modulus variation with CO ₂ saturation for different methods of saturation calculation (Macquet and Lawton, 2017).	5
Figure 1-4: Interpreted migration of injected CO ₂ plume at Sleipner using time-lapse 3D seismic (Eiken et al., 2011).....	6
Figure 1-5: Change in V _p between 1999-2006 from full waveform inversion and estimated changes in CO ₂ saturation for various saturation methods (after Queißer and Singh, 2013).	6
Figure 1-6: a) Map of Alberta, showing location of Calgary and Brooks; b) Map showing location of FRS relative to Brooks; c) Schematic diagram of FRS (Google, n.d.; Lawton et al., 2017).	8
Figure 2-1: Examples of vertical seismic profile (VSP) source and receiver configurations (after EPGeology, 2014).	12
Figure 2-2: Schematic diagram of SeisMovie acquisition system (CGG, 2008).....	13
Figure 2-3: Travel time variation (left) and amplitude variation (right) for 4D seismic data acquired with the SeisMovie system at Schoonebeek (after Cotton, Laurene and Forgues, 2012).	14
Figure 2-4: Schematic of orbital vibrator seismic source (Daley and Cox, 2001).	16
Figure 2-5: Schematic of orbital vibrator source signature for clockwise and counter-clockwise mass rotation (Daley and Cox, 2001).....	18
Figure 2-6: ACROSS seismic acquisition system installed on concrete foundation (Takanashi, Kato, & Kasahara 2014).....	20
Figure 2-7: Example of time-frequency relationship (left) and amplitude spectrum (right) of ACROSS seismic acquisition system (Nakatsukasa et al., 2018).....	21
Figure 2-8: Location of the CO ₂ CRC Otway Project in Victoria, Australia (CO ₂ CRC, 2019). .	22
Figure 2-9: Schematic of SOV installed with rotation axle perpendicular to trenched DAS fibre at the Otway site (Dou et al., 2016).....	23
Figure 2-10: SOV cemented to the ground at the Otway site (Freifeld et al., 2016).....	23

Figure 2-11: DAS VSP data acquired using SOV. Borehole reverberation (4), downgoing P-wave (5), and tube wave (6) identified. Possible upgoing P-wave shown by arrows (after Freifeld et al., 2016).	24
Figure 2-12: GPUSA large surface linear vibrator.	26
Figure 2-13: GPUSA borehole linear vibrator prior to installation.	26
Figure 2-14: Schematic of GPUSA surface linear vibrator mounted on steel helical pile (Wilkinson, 2017).	27
Figure 2-15: Example of DAS broadside insensitivity. Incident seismic waves are recorded with zero amplitude when normal to fibre (Mateeva et al., 2012).	30
Figure 2-16: Schematic diagram of DAS fibre loop at the CaMI FRS (Lawton, Osadetz, & Saeedfar, 2016).	31
Figure 3-1: Map of the CaMI FRS showing locations of observation and injection wells and surface infrastructure. Classroom in blue, instrumentation shack in purple.	33
Figure 3-2: CaMI FRS P-wave velocity model derived from 10-22 well logs. Gamma ray and P- and S-wave velocity logs from 10-22 shown.	34
Figure 3-3: Raytracing experiment using FRS velocity model. Well A is the geochemistry well and Well B is the geophysics well. Offset between permanent source and geochemistry well is 110 m.	36
Figure 3-4: Raytracing experiment using FRS velocity model. DAS fibre as the receiver simulated by receivers at 1 m intervals in geophysics well.	37
Figure 3-5: Fluid substitution results using Reuss average to model well logs at various CO ₂ saturation levels (Red: baseline, green: 10% CO ₂ , blue: 30% CO ₂ , yellow: 100% CO ₂).	38
Figure 3-6: Offset synthetic seismograms for the baseline case (top) and 30% CO ₂ saturation case (bottom). BBRs reflector identified by yellow arrow. The stack of all offsets is shown by the traces in the right panel of the displays.	40
Figure 3-7: Offset synthetic seismogram stacks for the a) baseline and b) CO ₂ saturated cases, and the difference (c) between the two stacks. Approximate interval used for FRM identified by red lines.	41
Figure 3-8: AVO curves for baseline case (left) and post-injection case (right).	41
Figure 3-9: Time-frequency relationship (0-150-0 Hz over 50 s) for example synthetic permanent source sweep (a); synthetic sweep scaled by factor of ω^2 (b); positive lags of synthetic sweep autocorrelation (c); synthetic sweep amplitude spectrum (d).	44

Figure 3-10: Comparison of synthetic permanent source sweep autocorrelation (blue) and 150 Hz Ricker wavelet (red).	44
Figure 3-11: CaMI FRS P-wave velocity model with finite-difference simulation acquisition geometry overlain. Source location (yellow star) located 59 m from geophysics well (centre of figure) and 109 m from geochemistry well. Geophones in geophysics well identified by red inverted triangles. DAS receivers identified by black circles.	46
Figure 3-12: Results from finite-difference simulation using FRS P-wave velocity model. Source signature used were a synthetic permanent source sweep (left) and 150 Hz Ricker wavelet (right).	46
Figure 3-13: Upgoing wavefield from synthetic VSP data from finite-difference simulation for synthetic permanent source sweep (left) and 150 Hz Ricker wavelet (right).	47
Figure 3-14: Outside corridor from synthetic VSP data from finite-difference simulation for synthetic permanent source sweep (left) and 150 Hz Ricker wavelet (right).	47
Figure 3-15: Corridor stacks from synthetic VSP data from finite-difference simulation for synthetic permanent source sweep (left) and 150 Hz Ricker wavelet (right). Approximate BBRS interval identified by arrows.	48
Figure 4-1: The CREWES Envirovibe, used as the source for baseline seismic datasets (CREWES, 2011).	50
Figure 4-2: Source and receiver acquisition geometry for May 2017 2D seismic line acquisition. Observation and injection well locations indicated on the map.	50
Figure 4-3: Source and receiver elevations for May 2017 2D line acquisition program.	51
Figure 4-4: Example shot record from station 101 (southwest end of line). Deeper reflections are noticeable at approximately 900 ms. BBRS interval between 250-300 ms.	51
Figure 4-5: Data processing workflow for May 2017 2D line.	52
Figure 4-6: Stacked 2D line from May 2017 after application of 5-point spatial median filter to enhance shallow reflectors. BBRS between 250-300 ms. Shown with synthetic seismogram tie.	52
Figure 4-7: Final migrated 2D line from May 2017 survey.	53
Figure 4-8: Source locations for baseline VSP datasets. Source locations for May 2017 survey (red) and July 2017 survey (blue) shown. Selected source locations for processing identified with stars.	54
Figure 4-9: Vertical component of geophone data from shot point 27110 (approximately 58 m offset). Automatic gain correction (AGC) applied. Noisy traces observed on record.	55

Figure 4-10: Interpolated vertical component of geophone data from shot point 27110. Downgoing wavefield (red) and upgoing wavefield (yellow) identified by arrows.	55
Figure 4-11: Vertical component of geophone data with first break picks overlain (green). Velocity profile shown on right. RMS velocity (blue) and interval velocity (red) displayed.	56
Figure 4-12: Flattened total wavefield (left), flattened downgoing wavefield (centre), and upgoing wavefield (right) from vertical component of geophone data.	57
Figure 4-13: Upgoing wavefield (left) after VSP deconvolution with the downgoing wavefield and F-K filter (right) to remove residual downgoing energy. Data within the shaded region on the F-K plot was passed through the filter.	58
Figure 4-14: Upgoing wavefield after VSP deconvolution and NMO correction. Displayed in TWT.	58
Figure 4-15: Comparison of geophone corridor stack (left) and synthetic seismogram (right), generated with a 10-150 Hz synthetic Vibroseis sweep.	59
Figure 4-16: VSP data processing workflow.	59
Figure 4-17: Seismic data using full DAS fibre loop from shot point 13153. AGC applied.	60
Figure 4-18: DAS seismic data from observation wells. “V”-shape of first breaks from upgoing and downgoing segments of fibre in each well. Noticeable dimming of data on helical fibre data compared to straight fibre. AGC applied.	61
Figure 4-19: Raw DAS data from straight fibre in geophysics well. Depth segment to be removed identified by arrow. Several noisy channels observed.	62
Figure 4-20: Straight fibre VSP in geophysics well with first break picks before median filter (green) and after median filter (red).	63
Figure 4-21: Interpolated straight fibre VSP, resampled to 1.0 m channel spacing intervals.	64
Figure 4-22: Straight fibre VSP upgoing wavefield before (left) and after (right) VSP deconvolution with downgoing wavefield and F-K filter to remove residual downgoing energy.	64
Figure 4-23: Comparison of geophone corridor stack (left), synthetic seismogram (centre), and straight fibre corridor stack (right).	65
Figure 4-24: Straight fibre data from geophysics well (left) and geochemistry well (right). Decreased reflector amplitudes are observed on geochemistry well fibre. AGC applied. ...	66

Figure 4-25: Comparison of straight fibre corridor stacks from geochemistry well (left) and geophysics well (right). Similar character observed, with lower amplitude reflectors and slight time delay for the geochemistry well corridor stack.	66
Figure 4-26: Comparison of 10-fold data (left) and 3-fold data (right) from straight fibre VSP in geophysics well.	68
Figure 4-27: Straight fibre VSP in geophysics well with first break picks before median filter (green) and after median filter (red) overlain.	69
Figure 4-28: Straight fibre VSP in geophysics well with first break picks for 1, 2, 4, and 8-sweep data.	69
Figure 5-1: Traces from surface geophone nearest borehole linear vibrator (Station 36) for the five test sweeps.	71
Figure 5-2: Amplitude spectra of pilot traces for the five borehole linear vibrator test sweeps.	73
Figure 5-3: Amplitude spectra of surface 2D spread of geophones for each of the five borehole linear vibrator test sweeps.	73
Figure 5-4: Results of fitting quadratic models (green) to the envelope (red) of the amplitude spectra (black) of each borehole linear vibrator pilot trace.	74
Figure 5-5: Time-frequency spectra of the pilot traces for each of the five borehole linear vibrator test sweeps.	75
Figure 5-6: Time-frequency spectra of the surface 2D spread of geophones for each of the five borehole linear vibrator test sweeps.	76
Figure 5-7: Time-frequency spectra of the surface 2D spread of geophones for each of the five test sweeps. Each frequency component of the spectra has been normalized.	76
Figure 5-8: Traces used for correlation tests. All traces have a 0-175-0 Hz over 50 s time-frequency relationship. a) Linear sweep with ω^2 quadratic scaling; b) Linear sweep with cosine taper and ω^2 quadratic scaling; c) Pilot trace from sweep 1026.	78
Figure 5-9: Cross-correlation results for quadratic-scaled synthetic sweep and pilot trace. a) Synthetic sweep autocorrelation; b) Pilot trace autocorrelation; c) Cross-correlation between synthetic sweep and pilot trace.	79
Figure 5-10: Borehole geophone data correlated with quadratic-scaled synthetic sweep.	80
Figure 5-11: Borehole geophone data correlated with pilot trace.	80
Figure 5-12: Vertical component of borehole geophones (left) and surface 1C geophones (right). Data correlated with surface pilot trace.	81

Figure 5-13: Vertical component of borehole geophone data, correlated with surface pilot trace. Dead traces have been muted.	81
Figure 5-14: Deconvolution algorithm tests applied to correlated pilot trace. Traces displayed: a) Correlated pilot trace; b) Wiener deconvolution; c) Gabor deconvolution; d) deterministic deconvolution with the pilot trace; e) Deterministic deconvolution with the synthetic sweep.	82
Figure 5-15: Amplitude spectra of correlated trace (black) and traces after Wiener (red) and Gabor (green) deconvolution applied.	84
Figure 5-16: Borehole linear vibrator data with borehole geophone receivers, correlated with surface pilot trace. Wiener deconvolution (left) and Gabor deconvolution (right) applied to correlated data.	85
Figure 5-17: Envirovibe data recorded with borehole geophones at equivalent offset to borehole source. No deconvolution applied.	85
Figure 5-18: Corridor stack comparison between Vibroseis (left) and borehole linear vibrator (right) data.	86
Figure 5-19: VSP data correlated with pilot traces from each sweep. Note the strong horizontal noise bands on Sweeps 7 and 9.	87
Figure 5-20: Stacked VSP gather from 10 borehole linear vibrator sweeps with same sweep parameters.	87
Figure 5-21: Data from ten borehole linear vibrator sweeps. Data were stacked, then correlated with a pilot trace, then Gabor deconvolution was applied.	89
Figure 5-22: Data from ten borehole linear vibrator sweeps. Data were correlated with pilot traces from each sweep, then stacked, then Gabor deconvolution was applied.	90
Figure 5-23: Data from ten borehole linear vibrator sweeps. Data were correlated with pilot traces from each sweep, then Gabor deconvolution was applied, and the deconvolved records were stacked.	90
Figure 5-24: Source and receiver acquisition geometry for large surface linear vibrator testing.	91
Figure 5-25: Near (a), mid (b), and far (c) offset uncorrelated traces from surface geophones for a test sweep of large surface linear vibrator.	93
Figure 5-26: Time-frequency spectra for near (a), mid (b), and far (c) offset traces from surface geophones from a test sweep of large surface linear vibrator.	94
Figure 5-27: Sweeps 1-4 from large surface linear vibrator accelerometer tests.	95

Figure 5-28: Sweeps 5 and 6 from large surface linear vibrator accelerometer tests.	96
Figure 5-29: Sweeps 8, 9, 11, and 12 from large surface linear vibrator accelerometer tests.	96
Figure 5-30: Time-frequency plots for ten large surface linear vibrator accelerometer test sweeps. Sweeps 1-4 (a-d) have a linear and symmetric upswing and downswing. Sweeps 5 and 6 (e and f) have a linear upswing and uncontrolled downswing. Sweeps 8, 9, 11, and 12 have a linear and symmetric upswing and downswing, and hold the vibrator frequency at maximum for approximately 10 s.	97
Figure 5-31: Uncorrelated traces from large surface linear vibrator tests. Source accelerometer (left) and pilot trace (right) shown.	99
Figure 5-32: Time-frequency plots from large surface linear vibrator accelerometer (left) and surface geophone pilot trace (right).	100
Figure 5-33: Normalized amplitude spectra from large surface linear vibrator accelerometer (left) and surface geophone pilot trace (right).	100
Figure 5-34: Amplitude spectrum from geophone pilot trace during large surface linear vibrator testing (blue) with source accelerometer amplitude spectrum overlain.	101
Figure 5-35: Surface spread of geophones correlated with large surface linear vibrator pilot trace.	102
Figure 5-36: Surface spread of geophones correlated with large surface linear vibrator accelerometer recording.	102
Figure 5-37: Surface spread of geophones correlated with large surface linear vibrator pilot trace. Approximate locations of first breaks (red), air blast (yellow), and primary reflections (green) identified.	103

List of Symbols, Abbreviations and Nomenclature

°	Degrees
°C	Degrees Celsius
θ	Angle
μ	Shear modulus
ρ	Density
φ	Porosity
ω	Angular frequency
1C	One component
2D	Two dimensional
3C	Three component (multicomponent)
3D	Three dimensional
4D	Four dimensional
A	Amplitude
a_c	Centripetal acceleration
ACROSS	Accurately Controlled and Routinely Operated Signal System
AGC	Automatic gain correction
AVO	Amplitude variation with offset
BBRS	Basal Belly River Sandstone
CaMI	Containment and Monitoring Institute
CCS	Carbon capture and sequestration
CCW	Counter-clockwise
cm	Centimetre
CW	Clockwise
CREWES	Consortium for Research in Elastic Wave Exploration Seismology
CO ₂	Carbon dioxide
DAS	Distributed acoustic sensing
EOR	Enhanced oil recovery
f	Frequency
F_c	Centripetal force
F-K	Frequency-wavenumber
FRM	Fluid replacement modelling
FRS	Field Research Station
GHG	Greenhouse gas
GPa	Gigapascal
Hz	Hertz
IEA	International Energy Agency
IPCC	Intergovernmental Panel on Climate Change
K	Bulk modulus
km	Kilometre
lbs	Pounds
m	Metre
MMV	Measurement, monitoring, and verification

m/s	Metres per second
ms	Millisecond
NMO	Normal moveout
P-wave	Compressional seismic wave
r	Rotation radius
R^2	Coefficient of determination
RMS	Root-mean-square
S	Saturation
S-wave	Shear seismic wave
SAGD	Steam-assisted gravity drainage
SNR	Signal-to-noise ratio
SOV	Surface orbital vibrator
t	Time
TD	Total depth
TWT	Two-way time
VFD	Variable frequency drive
u	Radial particle displacement
V_p	P wave velocity
V_s	S wave velocity
VSP	Vertical seismic profile
Z	Acoustic impedance

Chapter 1 – Introduction

1.1 Project motivations

Climate change has been described as “the defining issue of our time” (United Nations, 2019), and understanding the science and methods by which the potentially catastrophic effects of climate change can be mitigated is of the utmost importance. In its Fifth Assessment Report, the Intergovernmental Panel on Climate Change (IPCC) concluded that human activities are the primary driver of global climate change (IPCC, 2013). Therefore, human intervention is required to slow down the effects of anthropogenic climate change, including cutting emissions of carbon dioxide (CO₂) from 2010 levels by 45% by the year 2030, with a net-zero CO₂ emission framework in place by 2050 (IPCC, 2018). The International Energy Agency (IEA) has highlighted three different scenarios for the response to future greenhouse gas (GHG) emissions, including CO₂ (International Energy Agency 2018b; Figure 1-1):

1. Current Policies Scenario, where no new action is taken, and no peak in global CO₂ emissions is realized. Levels of atmospheric CO₂ would continue to grow unchecked.
2. New Policies Scenario, where new legislation and policies announced by governments are enacted. In this scenario, global CO₂ emissions are slowed, however no peak in emissions is reached.
3. Sustainable Development Scenario, where a global commitment is made to an accelerated clean energy transition and CO₂ emissions are reduced.

To mitigate, and potentially reverse, the negative consequences of global anthropogenic climate change, action must be taken to reduce emissions of CO₂ and other GHGs. Governments around the world have committed to action, with many ratifying the 2015 Paris Agreement, under which participants will endeavour to limit the increase in mean global temperature to 2°C, with

further goals to limit the increase to 1.5°C (Government of Canada, 2016). There are several pathways forward to achieving these goals of reducing GHG emissions, limiting global temperature increase, and combat the negative consequences of global climate change.

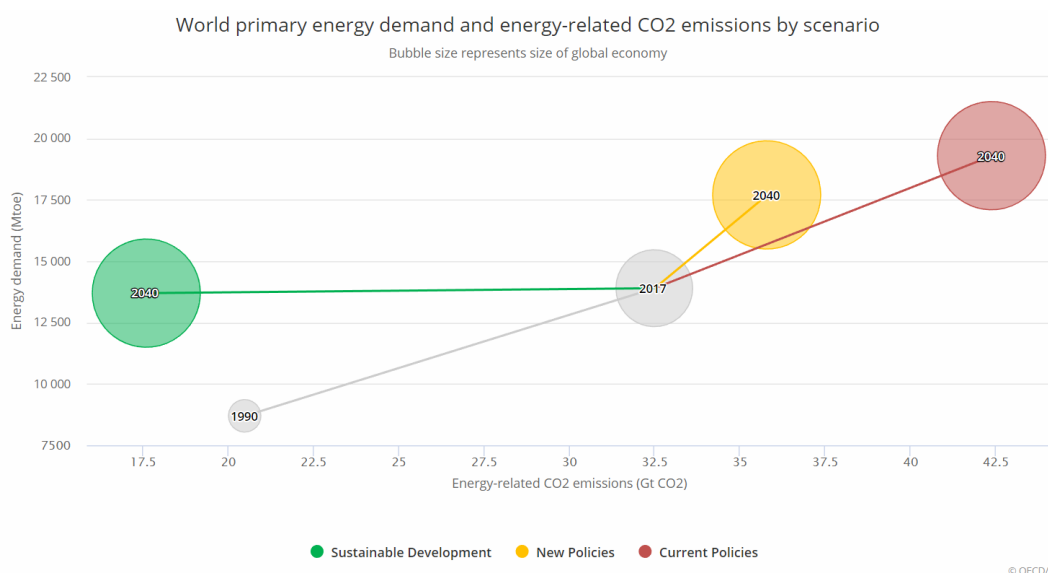


Figure 1-1: IEA global policy scenarios and their impact on energy demand and CO₂ emissions (from IEA, 2018).

1.1.1 Carbon capture and sequestration

One proposed technology to aid in the reduction of global CO₂ emissions is carbon capture and sequestration (CCS). It is anticipated that CCS could account for approximately 7% of global emissions reductions by 2040 in the IEA's (2018) Sustainable Development Scenario as compared to the New Policies Scenario (Figure 1-2). However, this represents an increase in the levels of sequestered carbon of over 75 times the current level of injection (International Energy Agency, 2018a), thus CCS is only one of many tools that can be used to mitigate the effects of global climate change.

In CCS, carbon dioxide is isolated from other compounds through chemical processes and is usually captured from industrial activities or large point emitters, such as power plants (International Energy Agency, 2018a). Captured CO₂ is then transported, usually by truck or pipeline, to a storage site where it is injected into geologic formations in the subsurface.

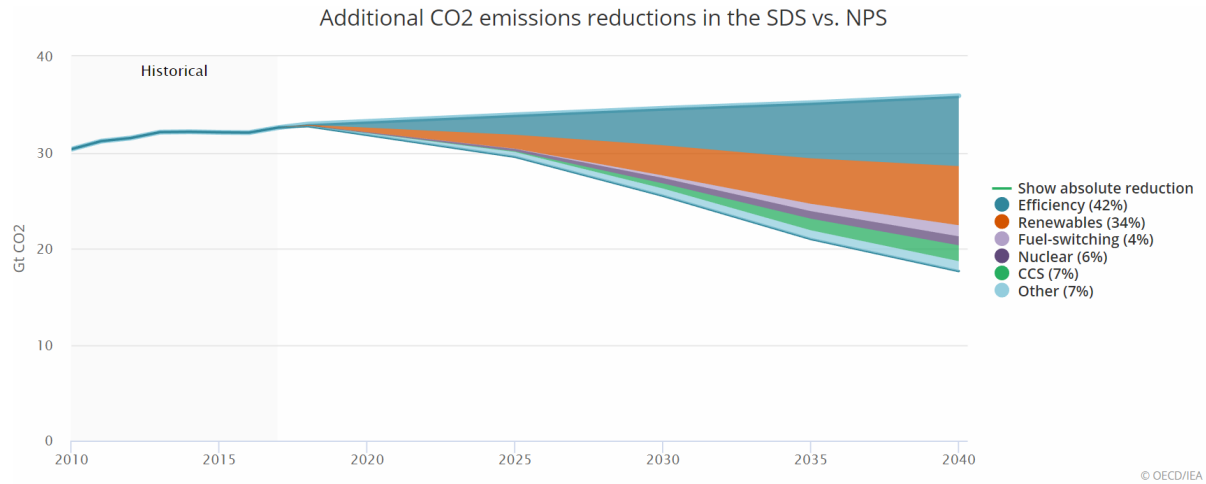


Figure 1-2: Contribution of various emissions reduction methods in IEA Sustainable Development Scenario versus New Policies Scenario (from IEA, 2018).

1.1.2 Time-lapse seismic monitoring

To monitor how injected CO₂ behaves in subsurface reservoirs in sequestration projects, time-lapse, or 4D, seismic is often used. Several existing carbon sequestration projects have used 4D seismic to great success in ensuring injected CO₂ remains in the storage reservoir, and to study how the injected plume migrates through the subsurface (e.g. Arts et al., 2008; Huang et al., 2018; Li, 2003). The success of 4D seismic in discerning the behaviour of injected CO₂ is due to the large contrast in acoustic impedance expected between CO₂ and *in-situ* reservoir fluids, such as brine (Furre et al., 2017). The acoustic impedance, Z , for a given medium is given by:

$$Z = V_p \rho \quad (1.1)$$

Where V_p is the compressional wave, or P wave, velocity of the medium, and ρ is the density. The P-wave velocity is dependent on the density of the medium, as shown by:

$$V_p = \sqrt{\frac{K + \frac{4}{3}\mu}{\rho}} \quad (1.2)$$

Where K is the bulk modulus of the medium, and μ is the shear modulus. Therefore, changes in the density of the medium will also drive changes in its velocity. As injected CO₂ displaces reservoir fluids, the bulk modulus of the reservoir will change, resulting in an observable change in the acoustic impedance. The change in bulk modulus, and thus velocity, due to increased saturation of CO₂ in the reservoir is most noticeable between 0-30% saturation, for most saturation calculation methods (Macquet & Lawton, 2017; Figure 1-3).

One prominent example of the implementation of 4D seismic surveying in monitoring CO₂ sequestration is the Sleipner project, located offshore Norway in the North Sea. In the Sleipner project, CO₂ is captured from produced gas condensate, and injected into a highly porous saline aquifer. Injection began in 1996 and has continued to the present. Since inception, nine 3D seismic monitor surveys, along with a baseline survey in 1994, have been conducted over the Sleipner project (Furre et al., 2017). The vertical and lateral migration of the injected CO₂ has been studied extensively and with great success using this comprehensive seismic dataset (Eiken et al., 2011; Figure 1-4). The lateral extension of the CO₂ plume has been interpreted to have reached up to 1800 m by 2006, and the vertical thickness of the plume has grown from 0 to 8 m (Arts et al., 2008). Additionally, the change in CO₂ saturation in the injection reservoir has been estimated through a full waveform inversion-based approach, whereby inverted P-wave velocity is related to saturation levels (Queißer & Singh, 2013; Figure 1-5).

While time-lapse seismic has proven to be a valuable tool in monitoring CCS projects, there are some key problems that must be addressed. First, the interval between surveys is typically on the order of one or more years, resulting in infrequent data points to understand the conformance and migration of injected CO₂. The value in rapidly acquiring time-lapse data has been demonstrated by Byerly et al. (2018). In their study, it was shown that the 4D effects of individual hydraulic fracturing stages can only be observed for a few days after stimulation and would thus not be measured with typical 4D methods. Second, survey repeatability could be negatively impacted through inaccuracies in the redeployment of sources and receivers. Repeatability refers to how close repeated results agree when the same method is performed on the same test material (Schlumberger, 2019). Therefore, if a seismic experiment was conducted with the same source type, acquisition geometry, field conditions, and data processing workflow, the resultant datasets would be identical. In the case of time-lapse seismic, changes in the resultant datasets that are independent of changes in the subsurface should be minimized as much as possible (Kragh & Christie, 2002).

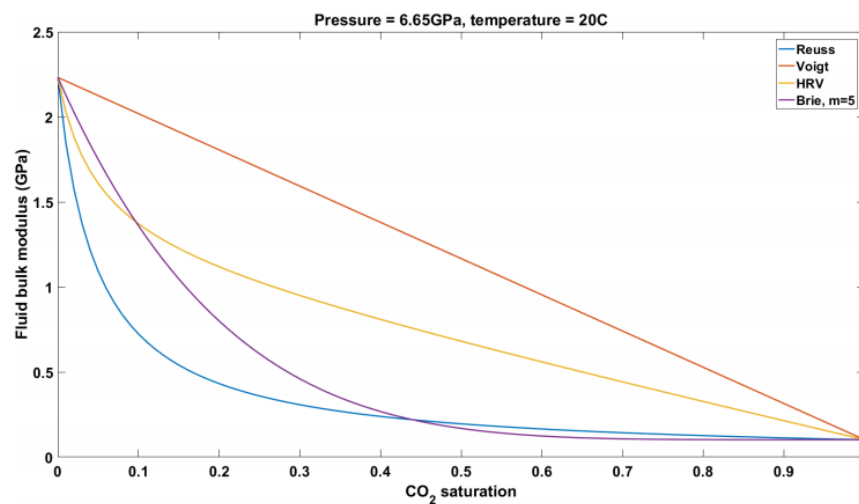


Figure 1-3: Bulk modulus variation with CO₂ saturation for different methods of saturation calculation (Macquet and Lawton, 2017).

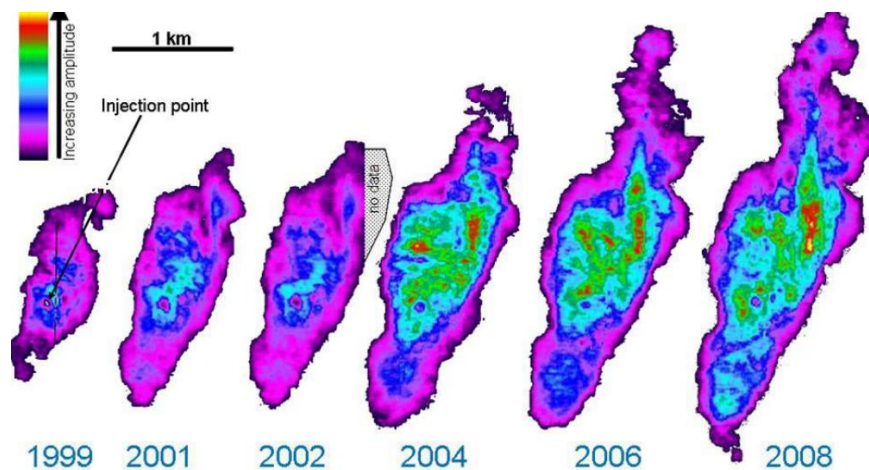


Figure 1-4: Interpreted migration of injected CO₂ plume at Sleipner using time-lapse 3D seismic (Eiken et al., 2011).

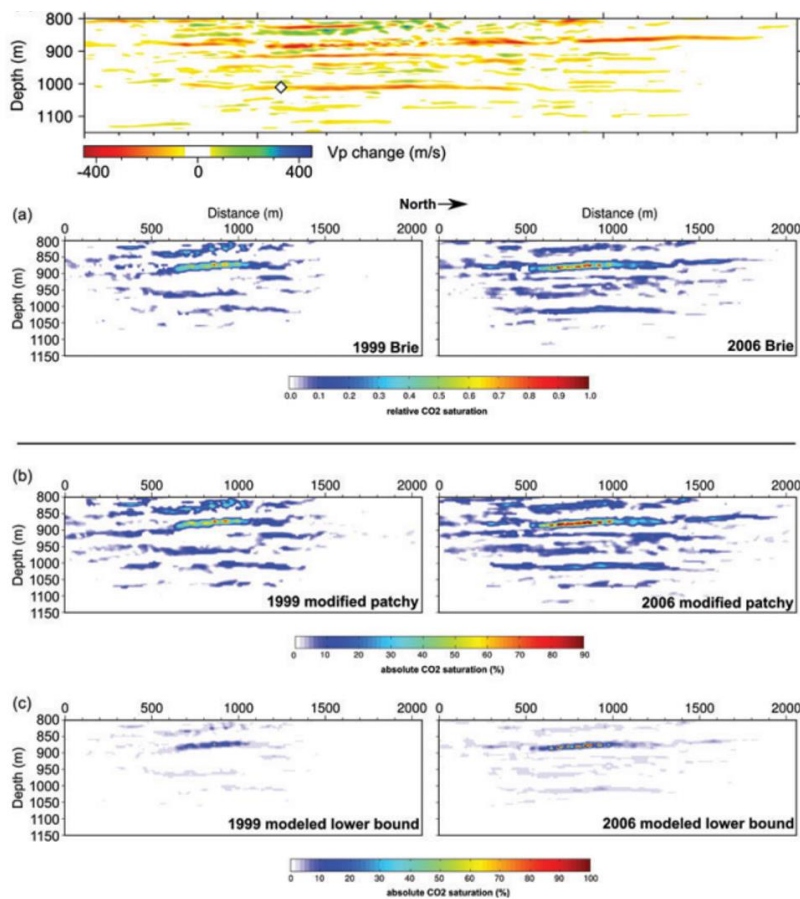


Figure 1-5: Change in V_p between 1999-2006 from full waveform inversion and estimated changes in CO₂ saturation for various saturation methods (after Queier and Singh, 2013).

1.2 Containment and Monitoring Institute Field Research Station

To further investigate the viability of time-lapse seismic, as well as other monitoring technologies, in the context of CCS, the Containment and Monitoring Institute (CaMI) established the Field Research Station (FRS), where all data used in this project were collected. The FRS is located in Newell County, Alberta, approximately 25 km southwest of Brooks, and approximately 200 km southeast of Calgary, the nearest major urban centre (Figure 1-6). The FRS is a small-scale CCS site; however, the primary goal of the site is not the long-term storage of CO₂. Rather, the purpose of the site is to facilitate the research and development of measurement, monitoring, and verification (MMV) technologies for the study of the containment and conformance of injected fluids, with a particular emphasis on CO₂ (Lawton, Osadetz, & Saeedfar, 2017). Numerous geophysical and geochemical MMV technologies are being evaluated for their efficacy in monitoring subsurface fluids, including fibre-optic acoustic and thermal sensing, downhole fluid sampling, and novel approaches to seismic monitoring. While the FRS was constructed in partnership with the University of Calgary, numerous research groups and scientists from around the world are conducting valuable research projects at the site (Containment and Monitoring Institute, 2019).

The FRS is located on the plains of southern Alberta, where there has historically been extensive hydrocarbon exploration and drilling. Therefore, a wealth of information about the regional geology of the site is readily available through existing well logs. More specific geological insights can be gained by studying the well logs of wells drilled at the FRS. To date, three vertical wells have been drilled at the FRS itself for injection of CO₂ and the installation of various monitoring tools. The injection well, 100/10-22-017-16W4/00, was drilled to a total depth (TD)

of approximately 550 m and is located roughly at the centre of the site. The two observation wells, 102/10-22-017-16W4/00 and 103/10-22-017-16W4/00, known colloquially as the “geochemistry well” and “geophysics well”, are located approximately 30 m northeast and 20 m southwest, respectively, of the injection well.

Injection of CO₂ at the FRS will take place in two phases, with each phase targeting a different reservoir (Lawton et al., 2017). Phase 1 of injection, currently underway, targets the Basal Belly River Sandstone (BBRS) at approximately 300 m depth. Phase 2 will target the Medicine Hat Formation, at approximately 500 m depth. Both of the target reservoirs are Upper Cretaceous in age. The BBRS is comprised largely of shoreface sandstones and has produced gas in nearby pools (Isaac and Lawton, 2014a). At the FRS, however, the BBRS is saturated with reservoir water. The BBRS, approximately 7 m thick near the FRS, is overlain by silts and coals from a proximal coastal depositional environment (Isaac & Lawton, 2014a), which will serve as excellent sealing units for injected CO₂.

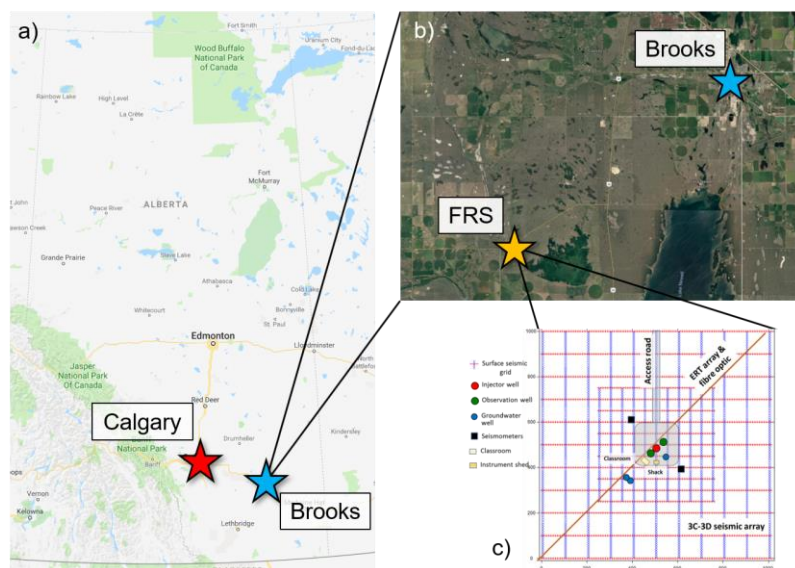


Figure 1-6: a) Map of Alberta, showing location of Calgary and Brooks; b) Map showing location of FRS relative to Brooks; c) Schematic diagram of FRS (Google, n.d.; Lawton et al., 2017).

1.3 Thesis objectives

As previously mentioned, typical seismic surveys in time-lapse projects are usually performed a year or more apart. Therefore, conformance and migration of injected fluids, such as CO₂, can only be inferred on the time scale of time-lapse acquisition. To allow for more rapid study of injected fluids, seismic data should be acquired more frequently, allowing operators to respond quickly to any potential conformance issues that may arise. This thesis will investigate the use of permanent seismic sources in rapidly acquiring time-lapse seismic data in the context of a small carbon sequestration project. As the seismic sources used in this project are still under development by the manufacturer, this thesis will be focused on the unique acquisition and data processing considerations of permanent seismic sources, rather than the interpretation of time-lapse seismic data. Additionally, the amount of CO₂ that has been injected to date would not reveal significant differences on a time-lapse survey. This thesis will assess the potential viability of permanent seismic sources; if permanent sources can be demonstrated to be a reliable alternative to conventional sources, time-lapse seismic surveys can potentially move towards a pseudo-real-time image of the changing subsurface.

1.4 Data used

1.4.1 Well data

Wireline well logs from the injector well and each of the observation wells were used at several stages of the project. While a full suite of well logs was recorded in each well, only the bulk density, compressional sonic, and shear sonic logs were used. Additionally, picked well tops were used to identify geologic formations of interest.

1.4.2 Seismic data

Several different seismic datasets were used throughout the duration of this project. Various different types of sources and receivers were employed, with the ultimate goal of utilizing permanent seismic sources in conjunction with fibre optic distributed acoustic sensing (DAS) as the receiver. DAS data were acquired in partnership with Lawrence Berkeley National Laboratory. A summary of the various seismic experiments is detailed below.

Table 1-1: Summary of seismic data used.

Date	Source type	Receiver type	Survey type
May 2017	CREWES EnviroVibe	1C geophones	2D line
May 2017	CREWES EnviroVibe	DAS fibre loop	Fibre loop
July 2017	CREWES EnviroVibe	DAS fibre loop, 3C geophones	Fibre loop, VSP
September 2018	GPUSA surface linear vibrator	1C geophones	2D line
September 2018	GPUSA borehole linear vibrator	3C borehole geophones, 1C surface geophones	VSP, surface 2D line
November 2018	GPUSA borehole linear vibrator	3C borehole geophones, 1C surface geophones	VSP, surface 2D line

1.5 Software used

Vista (Schlumberger) was used to perform the bulk of the VSP data processing, with additional processing performed in ProMAX (Halliburton). Matlab (Mathworks) was used to create synthetic datasets and for preliminary data interpretation. Hampson-Russell (CGG) was used to perform fluid substitution and modelling. Microsoft Word, PowerPoint, and Excel were used to create reports, presentations, figures, and to organize and analyze data.

Chapter 2 – Theory and State of the Art

2.1 Introduction

This section will describe the basic concepts of seismic acquisition and will motivate the desire to use permanent seismic sources as a monitoring tool, with a particular emphasis on orbital vibrators. Existing permanent seismic monitoring methods, namely the SeisMovie and ACROSS systems, as well as surface orbital vibrators used in the CO2CRC Otway Project, will be discussed and compared with the GPUSA linear vibrators used in the remainder of this project. This section will also discuss the use of distributed acoustic sensing for use in seismic acquisition projects.

2.2 Seismic acquisition

One tool widely used to investigate the subsurface on a large scale is reflection seismology. In reflection seismology, a source, typically dynamite or a Vibroseis truck, excites the earth, causing seismic waves to propagate through the subsurface. These waves pass through various strata in the subsurface, which act as a filter due to their varied acoustic and elastic properties. The seismic waves eventually return to the surface where they are recorded.

There are several types of source and receiver configurations used in seismic acquisition; however, this project will largely focus on vertical seismic profiles (VSP), with additional 2D data acquired with receivers on the surface. VSP surveys incorporate a wellbore and vary based on the configuration of the sources and receivers relative to the wellbore. VSPs play an important role in linking small scale well log measurements at the wellbore to larger scale measurements from typical seismic surveys (Lines & Newrick, 2004), as the seismic response is recorded with a known depth axis. A VSP survey with receivers in the borehole and a single source at the surface near the top of the receiver well is referred to as a zero-offset VSP, whereas a survey with the same receiver

configuration and a number of sources with regular spacing placed in a line away from the wellhead is known as a walk-away VSP (Stewart, 2001). Several walk-away, or multi-offset, and multi-azimuth VSP datasets have been acquired at the CaMI FRS (Gordon & Lawton, 2018; Gordon, Lawton, & Eaton, 2016), and a comprehensive multi-offset, multi-azimuth VSP survey was acquired in 2018 (Hall et al., 2018). This project will discuss examples of zero-offset and near offset VSP data (Figure 2-1) acquired at the CaMI FRS.

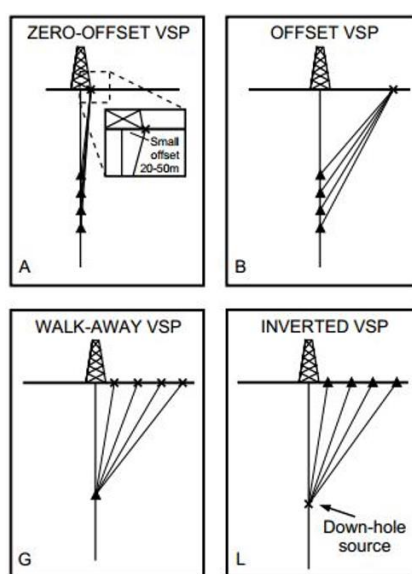


Figure 2-1: Examples of vertical seismic profile (VSP) source and receiver configurations (after EPGeology, 2014).

2.3 SeisMovie

One tool that has demonstrated success in rapidly acquiring time-lapse seismic data in recent years is the SeisMovie system developed by CGG. The SeisMovie system incorporates a permanently-installed array of sources and receivers deployed around the target to be imaged (Figure 2-2). Acquisition and basic processing using the SeisMovie system is automated, resulting in a pseudo-real-time “movie” of the target reservoir (CGG, 2008). Sources and receivers are

buried in the shallow near surface in order to attempt to mitigate the attenuative effects of the near surface, and to improve the repeatability of the system over longer recording periods (Cotton, Forgues, & Hornman, 2012). SeisMovie sources are piezoelectric vibrators, which are low-energy emitters. The piezoelectric effect refers to the property of certain materials whereby a positive and negative charge appear on opposite sides of a nonconducting crystal when the crystal is subjected to an external pressure (Encyclopaedia Britannica, 2018). The converse effect is also observed, where an external electric current applied to a crystal causes it to exert a mechanical stress. Therefore, by controlling the current applied to piezoelectric crystals, the SeisMovie system can run continuously to create high-resolution seismic data (CGG, 2008).

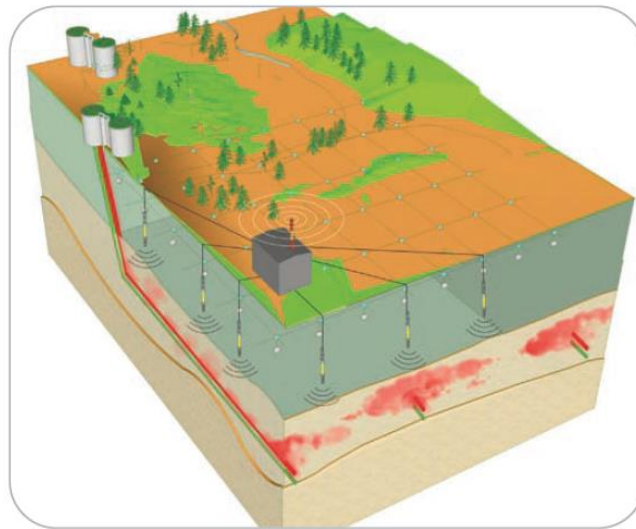


Figure 2-2: Schematic diagram of SeisMovie acquisition system (CGG, 2008).

To compensate for the low-energy nature of SeisMovie sources, they are run for long periods of time to maximize the amount of energy recorded by the receiver array (Bianchi et al., 2004). Shot records with an acceptable signal-to-noise ratio (SNR) can be created by stacking data acquired over a 24-hour period (Cotton et al., 2012).

Two field case studies have been conducted where the SeisMovie system was tested in the context of enhanced oil recovery (EOR) using steam. These case studies are the Schoonebeek heavy oil field in the Netherlands (Cotton et al., 2012), and a steam-assisted gravity drainage (SAGD) heavy oil project in the Peace River region of Alberta (La Follett et al., 2015). In both projects, steam is injected into the reservoir in order to liberate oil from reservoir rock, making it easier to produce. Like CCS projects, time-lapse seismic surveys can be used to monitor the conformance of injected steam due to the density contrast between steam and oil in the reservoir. Both the Schoonebeek and Peace River projects successfully demonstrated the ability of the SeisMovie system to acquire high-resolution seismic data for the monitoring of injected steam (Figure 2-3). However, the requirements of the SeisMovie system inherently carries a relatively high financial and environmental cost, due in part to the sheer number of source and receiver boreholes that must be drilled (Hornman et al., 2015). As the piezoelectric sources are low-energy emitters, a high number of sources must be used, and a source borehole must be drilled for each individual source. Therefore, a need exists for a permanently-installed seismic acquisition system with lower economic and environmental footprints.

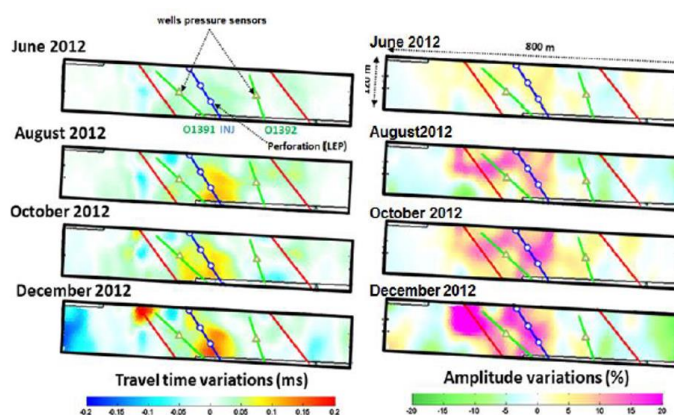


Figure 2-3: Travel time variation (left) and amplitude variation (right) for 4D seismic data acquired with the SeisMovie system at Schoonebeek (after Cotton, Laurene and Forgues, 2012).

2.4 Orbital vibrators

The concept of employing a rotational source for the generation of seismic waves has existed for nearly a century. Stanton was awarded a patent in 1931 for his “geo-oscillator,” which intended to use a semi-circular flywheel, attached to a power source via a belt, to act as an impulsive source to calculate the depth to certain interfaces in the subsurface (Patent No. US1790080A, 1931). In the early 1990’s, there was renewed interest from Conoco in deploying a downhole rotational source for the purpose of acquiring crosswell and reverse VSP datasets (Liu, Crampin, & Queen, 1991). In recent years, there has been further interest in using rotational vibrator sources for permanent reservoir monitoring.

2.4.1 Theory

Orbital vibrators are an attempt to approximate the source signature emitted by a Vibroseis source via a permanently installed rotational source. Orbital vibrators operate by rotating an eccentric, or unbalanced, wedge-shaped mass in a circle about an axle that is coupled to the ground. The centre of mass of the rotating wedge causes a radial particle displacement, u , at every point along the circular orbit as it passes through that point. The vertical and horizontal components of the particle displacement can be described by the angle between an arbitrary horizontal line, and a line connecting the centre of mass of the wedge and the rotation axle (Figure 2-4). This angle, θ , is equal to the product of the angular frequency, ω , and time, t . Therefore, the horizontal and vertical components can be described in Cartesian coordinates for the clockwise rotation direction by (Daley & Cox, 2001; Figure 2-5):

$$\begin{aligned} u_{cwx} &= A \cos(\theta) \\ &= A \cos(\omega t) \end{aligned} \quad (2.1a)$$

$$\begin{aligned} u_{cwy} &= A \sin(\theta) \\ &= A \sin(\omega t) \end{aligned} \quad (2.1b)$$

And for the counter-clockwise rotation direction by:

$$\begin{aligned} u_{ccwx} &= A \cos(-\theta) \\ &= A \cos(-\omega t) \\ &= A \cos(\omega t) \end{aligned} \quad (2.1c)$$

$$\begin{aligned} u_{ccwy} &= A \sin(-\theta) \\ &= A \sin(-\omega t) \\ &= -A \sin(\omega t) \end{aligned} \quad (2.1d)$$

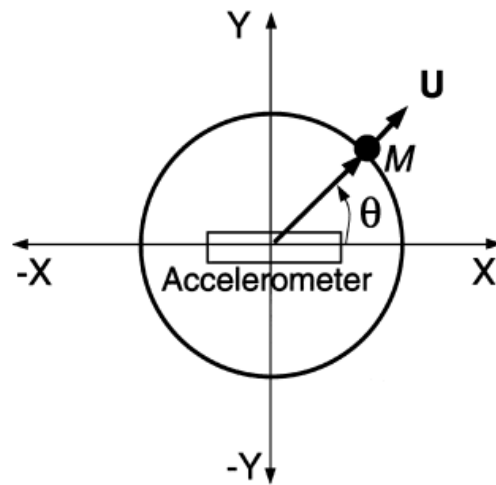


Figure 2-4: Schematic of orbital vibrator seismic source (Daley and Cox, 2001).

It is assumed that the amplitude of the particle displacement, A , remains constant for all angles. Therefore, by reversing the rotation direction of the mass between consecutive sweeps and computing either the sum of, or difference between, the resultant clockwise and counter-clockwise datasets, either the vertical or horizontal component of particle displacement can be cancelled. By taking the sum of the resultant datasets:

$$\begin{aligned}
u_x &= u_{cwx} + u_{ccwx} \\
&= A \cos(\omega t) + A \cos(\omega t) \\
&= 2A \cos(\omega t)
\end{aligned} \tag{2.2a}$$

$$\begin{aligned}
u_y &= u_{cwy} + u_{ccwy} \\
&= A \sin(\omega t) + (-A \sin(\omega t)) \\
&= 0
\end{aligned} \tag{2.2b}$$

Thus, the vertical component will be cancelled, and the orbital vibrator will act as a shear wave source. Similarly, by taking the difference:

$$\begin{aligned}
u_x &= u_{cwx} - u_{ccwx} \\
&= A \cos(\omega t) - A \cos(\omega t) \\
&= 0
\end{aligned} \tag{2.2c}$$

$$\begin{aligned}
u_y &= u_{cwy} - u_{ccwy} \\
&= A \sin(\omega t) - (-A \sin(\omega t)) \\
&= 2A \sin(\omega t)
\end{aligned} \tag{2.2d}$$

The horizontal component of particle displacement will be cancelled, and the source will behave as a P wave source. By decomposing the source signature of an orbital vibrator into horizontal and vertical components, a synthetic sweep signature can generally be described by the equation of a sine wave (Young & Freedman, 2008):

$$y(x, t) = A \cos \left[\omega \left(t - \frac{x}{v} \right) \right] \tag{2.3}$$

The amplitude, A , will be neglected for simplicity in modelling, and x will be set to zero. Recognizing that the cosine function is simply a sine function with a 90° phase shift applied, the following equation will be used to create synthetic sweeps:

$$\begin{aligned}
y &= \sin(\omega t) \\
&= \sin(2\pi f t)
\end{aligned} \tag{2.4}$$

Where f is the desired vibrator frequency.

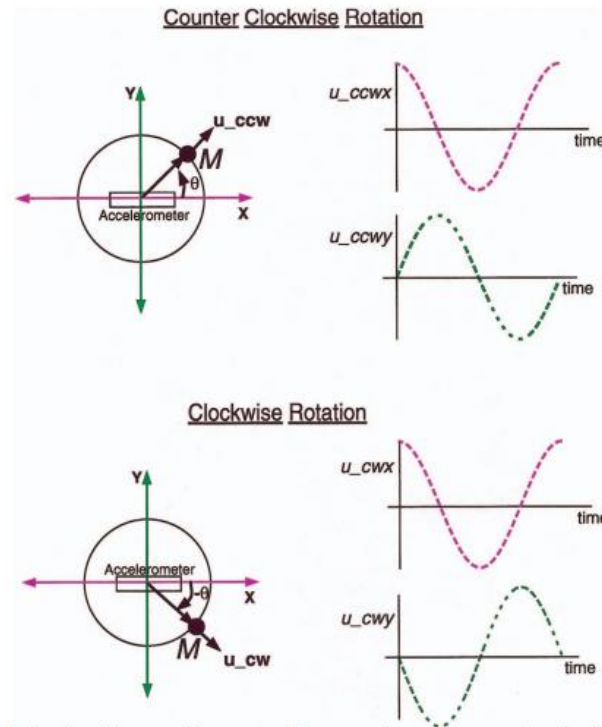


Figure 2-5: Schematic of orbital vibrator source signature for clockwise and counter-clockwise mass rotation (Daley and Cox, 2001).

The desired frequency of the source is controlled by a variable frequency drive (VFD) and is generally allowed to vary linearly. As a result, a general understanding of the force generated by an orbital vibrator can be derived. In rotational dynamics, the centripetal acceleration, \mathbf{a}_c , of a mass orbiting in a circular path is given by:

$$\mathbf{a}_c = r\omega^2 \quad (2.5)$$

Where r is the radius of rotation, measured as the distance between the rotation axis and the centre of mass of the rotating object. Equation (2.5) can be substituted into Newton's Second Law to give the centripetal force, F_c , of the rotating mass, m :

$$\begin{aligned} F_c &= m\mathbf{a}_c \\ &= mr\omega^2 \end{aligned} \quad (2.6)$$

This force acts upon the rotating mass, pointing towards the rotation axis. Therefore, by Newton's Third Law, a force also exists that acts upon the rotation axle, pointing towards the moment of inertia. Due to the coupling between the rotation axle and the ground, this force on the axle causes vibrations to propagate through the subsurface, thus acting as a controlled seismic source.

Consider the analogy common to rotational dynamics of a figure skater spinning, with arms outstretched, at a given angular frequency. While outstretched, the skater's arms increase the radius between the rotation axle and skater's centre of mass. Considering only the centripetal force, calculated using Equation (2.6), the skater will continue to spin at the same angular frequency as long as their arms remain stretched at the same radius. As the skater brings their arms closer to their body, the skater's angular frequency must increase (i.e. they will spin faster) due to the conservation of angular momentum.

However, in the case of orbital vibrators, the orbital radius of the eccentric mass is of fixed length. From Equation (2.6), this implies that the centripetal force is proportional only to the square of the angular frequency, while the rotational radius and the mass of the eccentric wedge are constants. The conservation of angular momentum does not apply in this case, as one stipulation for the conservation of angular momentum is that no external torque is applied (Young & Freedman, 2008). For orbital vibrators, an external torque is applied via the VFD, increasing the angular frequency of the rotating mass. As the centripetal force on the eccentric mass, and therefore the rotation axle, varies with the square of the angular frequency, it is assumed that the amplitude of the seismic signal recorded will also depend on the square of the angular frequency.

Conceptually, orbital vibrator sources behave very similar to conventional Vibroseis sources in the sense that both source types emit a sweep of seismic waves at various frequencies into the subsurface, and that the recorded data must be correlated with a known source sweep

signature before further analysis. This concept, and other data processing considerations, will be expanded upon in Chapter 5.

2.4.2 ACROSS system

One of the first orbital vibrator systems proposed for subsurface investigations is the Accurately Controlled and Routinely Operated Signal System (ACROSS), described by Kumazawa and Takei in 1994 (Kasahara & Hasada, 2017). The seismic ACROSS system very nearly follows the theoretical description of orbital vibrators detailed above, with a single eccentric mass rotating about an axle over a chosen frequency range. The frequency range of the seismic ACROSS source is limited to lower frequencies, approximately 5-50 Hz, and the source seeks to maintain phase consistency (Nakatsukasa et al., 2018; Takanashi, Kato, & Kasahara, 2014). To improve repeatability of the source by mitigating temporal variations, and to improve coupling between the source and the ground, the ACROSS system is typically installed on a thick concrete block (Kasahara & Hasada, 2017; Figure 2-6).



Figure 2-6: ACROSS seismic acquisition system installed on concrete foundation (Takanashi, Kato, & Kasahara 2014).

As described in the previous section, the force output by an orbital vibrator, and therefore the seismic amplitude recorded, is proportional to the square of the angular frequency. To accommodate for the increased force generation at higher frequencies, the ACROSS system utilizes a non-symmetric time-frequency relationship (Kasahara & Hasada, 2017), whereby the sweep duration at lower frequencies is greater than the duration at higher frequencies (Figure 2-7). Additionally, processing seismic data acquired with the ACROSS system differs from conventional data processing in that conventional processing flows utilize different deconvolution algorithms based on suitability to individual datasets, while processing ACROSS data relies on frequency domain source signature deconvolution (Kasahara & Hasada, 2017). Specific seismic data processing concerns for orbital vibrator data acquired in this project will be discussed further in Chapter 5.

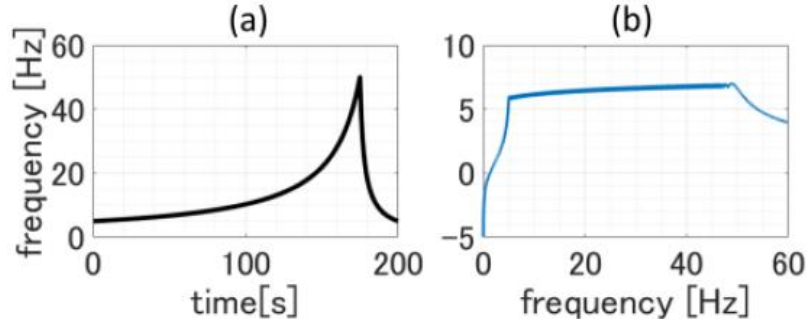


Figure 2-7: Example of time-frequency relationship (left) and amplitude spectrum (right) of ACROSS seismic acquisition system (Nakatsukasa et al., 2018).

While the ACROSS system has demonstrated great success in acquiring reliable datasets using a rotary source (Nakatsukasa et al., 2018; Takanashi et al., 2014), two significant drawbacks exist. As the source is fixed in place on a large cement foundation, the number of source locations is severely restricted, and datasets are therefore sparsely sampled in the spatial domain (Nakatsukasa et al., 2018). The limited number of sources deployed is also due to the significant

cost associated with each source. A more comprehensive and complete dataset could be generated using several source locations.

2.4.3 Surface Orbital Vibrator: The Otway Project

Similar to the CaMI FRS, the CO2CRC Otway Project, located approximately 200 km southwest of Melbourne in Victoria, Australia (Figure 2-8), is a CCS demonstration project, where the viability of CCS and various monitoring technologies is under investigation (CO2CRC, 2019). Among the technologies being tested are a combination of distributed acoustic sensing (DAS) with permanent surface orbital vibrator (SOV) sources. The SOVs deployed at the Otway Project are similar to the seismic ACROSS system, but are able to achieve higher maximum frequencies, up to approximately 100 Hz, largely due to the less complex and more inexpensive electronic control system (Dou et al., 2016). The sources operate in a similar fashion: an eccentric mass is rotated about an axle, with the rotation direction varied between clockwise and counter-clockwise.



Figure 2-8: Location of the CO2CRC Otway Project in Victoria, Australia (CO2CRC, 2019).

At the Otway Project site, an SOV is installed with its rotation axle oriented perpendicular to a distributed acoustic sensing (DAS) cable buried in a shallow trench (Figure 2-9). By orienting the axle perpendicular to the fibre and reversing the rotation direction, the data recorded by the fibre is naturally separated into compressional (P-wave) and vertically-polarized shear (SV-wave) components (Dou et al., 2016). The SOV is cemented on a concrete block on the ground to improve source coupling with the subsurface (Figure 2-10). Calculated repeatability metrics indicate higher sweep-to-sweep repeatability for S-waves than for P-waves, though this may be more strongly linked with the use of DAS as the receiver than with flaws with the source (Dou et al., 2016).

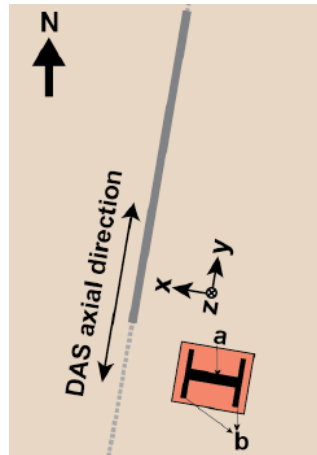


Figure 2-9: Schematic of SOV installed with rotation axle perpendicular to trenched DAS fibre at the Otway site (Dou et al., 2016).



Figure 2-10: SOV cemented to the ground at the Otway site (Freifeld et al., 2016).

A basic initial data processing flow is detailed by Freifeld et al. (2016). Optical noise in DAS data is suppressed by a spatial median filter in the receiver domain, followed by frequency domain source-signature deconvolution using a known sweep signature. Phase differences in deconvolved datasets are resolved by a correlation-based alignment process. Shot records are then combined through a mean stack to eliminate residual noise (Freifeld et al., 2016). This initial processing flow is similar to flows used to analyse ACROSS data and will be used as the basis for seismic data processing workflows during this project.

Applying the initial data processing flow to DAS VSP data from the Otway Project yields promising results (Figure 2-11). The downgoing compressional wavefield is clearly visible, and tube waves along with borehole reverberations have also been identified. Weak upgoing P-waves may be identified, but more work is needed to emphasize the upgoing wavefield.

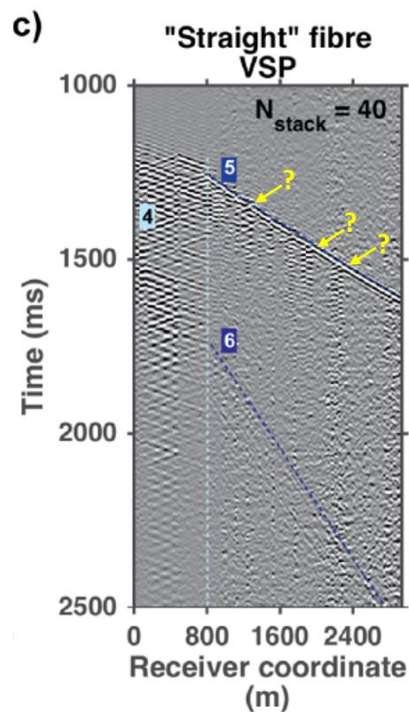


Figure 2-11: DAS VSP data acquired using SOV. Borehole reverberation (4), downgoing P-wave (5), and tube wave (6) identified. Possible upgoing P-wave shown by arrows (after Freifeld et al., 2016).

2.4.4 GPUSA linear vibrators

While both the SeisMovie and ACROSS systems have successfully demonstrated the capability to acquire high-quality 4D seismic datasets, both are not without drawbacks. The SeisMovie system has been shown to have a significant economic and environmental footprint, while the ACROSS system is limited both in the number of source locations and the maximum frequency of the source. SOVs deployed at the Otway site have shown some improvement but are still limited in terms of the number of source locations possible, and limited maximum frequency of the source. Surface and borehole linear vibrators, developed by GPUSA, are orbital vibrators that seek to improve upon the drawbacks of these other systems. These sources are referred to as linear vibrators as the frequency of the source is varied linearly with time.

Three different GPUSA linear vibrators (Table 2-1) will be tested in this project: a larger, more powerful source installed at the surface (Figure 2-12); a smaller source that is cemented in a shallow borehole (Figure 2-13); and a source similar to the borehole source but installed at the surface.

Table 2-1: GPUSA linear vibrator parameters

Source name	Frequency range (Hz)	Peak force (lbs)
Borehole linear vibrator	0-200	4,500
Small surface linear vibrator	0-200	4,500
Large surface linear vibrator ("orange vibe")	0-100	11,000

Both surface and borehole linear vibrators use two eccentric masses rotating about separate axes. The masses are kept in phase with each other using a timing belt. Using two eccentric masses

allows the sources to counter-rotate, thus resulting in a net vertical force, per equations (2-2c) and (2-2d).



Figure 2-12: GPUSA large surface linear vibrator.



Figure 2-13: GPUSA borehole linear vibrator prior to installation.

GPUSA linear vibrators offer a significant improvement over other orbital vibrator sources as the frequency band the sources are capable of sweeping is much broader. Higher frequency content in seismic data leads to shorter seismic wavelengths, which, in general, results in improved vertical resolution (Lines & Newrick, 2004). To mitigate seasonal and temporal variations in the near surface, as well as reduce the attenuative effects of the near surface, surface linear vibrators

are installed on a steel helical pile which is anchored to the bedrock. The source signature will theoretically travel through the pile from the linear vibrator at the surface, then radiate away from the pile at the anchor point (Wilkinson, 2017; Figure 2-14). The helical piles are segmented steel beams with a screw-like tip, allowing for simple and rapid installation. Additionally, several piles can be installed at a site, creating an opportunity for multiple source locations a significant advantage over the ACROSS and Otway SOV sources. A more apt description of GPUSA sources would be semi-permanently installed, as compared to these other permanently installed sources. The piles can also be installed relatively quickly and with minimal site disturbance (Wilkinson, 2017). This allows for reduced environmental impact while improving the spatial sampling of recorded datasets.

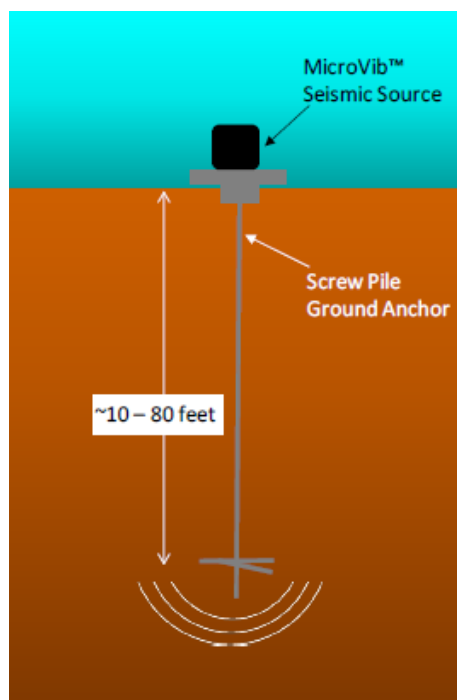


Figure 2-14: Schematic of GPUSA surface linear vibrator mounted on steel helical pile (Wilkinson, 2017).

In June 2018, a helical pile was installed at the CaMI FRS, approximately 80 m southwest of the injector well. The pile was drilled to a depth of approximately 15 m where it was anchored to a hard-packed argillaceous layer below more poorly consolidated glacial till in the shallow near surface. While the pile has not been anchored to the bedrock, which lies at a depth of approximately 30 m, the consolidated argillaceous layer should be sufficient to transfer the source signature through the near surface layer.

In June 2018, a shallow borehole was also drilled, and the borehole linear vibrator was installed in the borehole. The borehole was drilled to a depth of approximately 15 m, where the borehole vibrator was cemented in place. By cementing the source in the borehole, coupling between the source and the subsurface is improved, allowing for more efficient transfer of energy away from the source. Additionally, since the source was installed in a borehole, the impact of the near surface is drastically reduced.

2.5 Distributed acoustic sensing

In typical land seismic acquisition projects, seismic waves are recorded using geophones, measuring ground displacement in one or more directions. However, deploying a geophone array for use in time-lapse studies may face significant challenges in terms of the repeatability, cost, and receiver spacing. Recent advances in distributed acoustic sensing (DAS) may help address all three of these issues.

Eaid, Li and Innanen (2017) describe the physics which allow DAS to be used in seismic acquisition. Put simply, acquiring seismic data with DAS involves deploying fibre optic cable as the receiver, and using a light source, known as an interrogator unit, to emit a pulse of light through the fibre. As the light pulse travels through the fibre, it encounters microscopic impurities in the

fibre, which may cause the light to scatter through a process known as Rayleigh backscattering. Backscattered light is then recorded by the interrogator. As a seismic strain impinges upon the fibre, the fibre stretches and squeezes in the longitudinal direction of the fibre, causing small changes in the distances between impurities, and thus an alteration in the nature of the backscattered light recorded by the interrogator. These alterations are interpreted to be representative of the seismic signature.

DAS has shown to have several applications in various seismic monitoring projects (Mateeva et al., 2013; Molenaar et al., 2012), and has several advantages and disadvantages compared to more conventional receivers, such as geophones. Several of the disadvantages of DAS can be accommodated for with special consideration during either acquisition or processing. For example, the signal-to-noise ratio (SNR) of DAS is lower than geophones, which may pose issues in resolving low-amplitude reflectors. This can potentially be overcome by increasing source effort (i.e. using more sweeps for vibrator sources) (Mateeva et al., 2013). Additionally, DAS suffers from a phenomenon known as broadside insensitivity. This refers to the fact that DAS fibre deforms only in the longitudinal, or tangential, direction when interacting with strain arising from an incident P-wave. This implies that DAS is a single-component (1C) sensor. The seismic amplitude recorded with DAS depends on the angle, θ , between the incident ray of the P-wave and the fibre:

$$A \propto \cos^2(\theta) \quad (2.7)$$

Therefore, an incident ray normal to the longitudinal direction of the fibre will be recorded with zero amplitude (Figure 2-15). The problem of broadside insensitivity can potentially be mitigated by wrapping the DAS fibre in a helix around a central axis (Kuvshinov, 2016). Additionally, the

promise of a novel multicomponent DAS sensor is presently under investigation (Innanen et al., 2018).

At the CaMI FRS, DAS fibre was installed in a loop passing through the site. The loop starts and ends at an interrogator unit, has an upgoing and downgoing segment of both straight and helical DAS fibre in the geophysics well, an upgoing and downgoing segment of straight fibre in the geochemistry well, and a segment of straight fibre and a segment of helical fibre in the 1.1 km trench crossing the site (Figure 2-16). Seismic data acquired at the CaMI FRS using DAS will be analysed and compared with similar data acquired using geophones in Chapter 4.

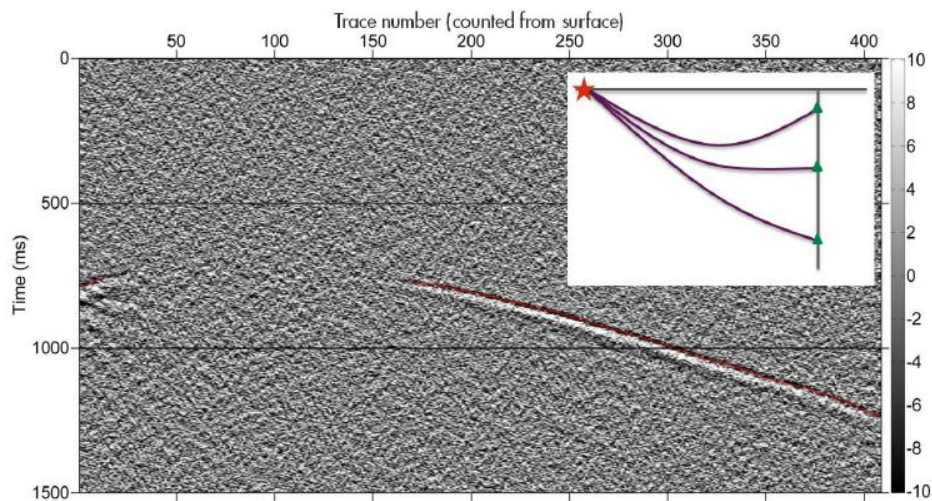


Figure 2-15: Example of DAS broadside insensitivity. Incident seismic waves are recorded with zero amplitude when normal to fibre (Mateeva et al., 2012).

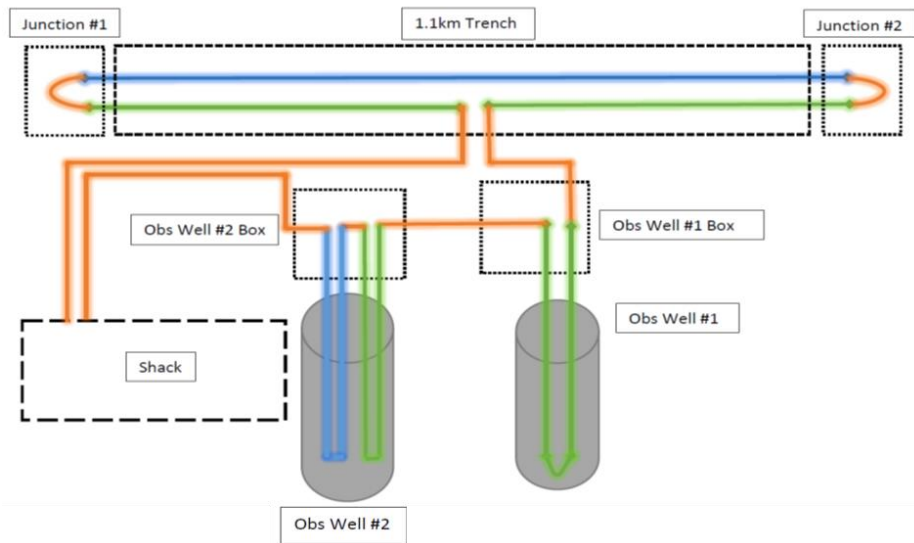


Figure 2-16: Schematic diagram of DAS fibre loop at the CaMI FRS (Lawton, Osadetz, & Saeedfar, 2016).

Chapter 3 –Source Installation

3.1 Introduction

This chapter will discuss several of the considerations made prior to the installation of GPUSA linear vibrator sources at the CaMI FRS. To find the ideal location for permanent seismic sources, a simple raytracing experiment was conducted using the baseline FRS velocity model. The impacts of CO₂ injection on the seismic signature were also investigated. Based on the results of the raytracing experiment, synthetic VSP data were generated for custom linear vibrator sweeps.

3.1 Raytracing Experiment

As discussed in Chapter 2, the capability exists for multiple source locations when acquiring seismic data with GPUSA linear vibrators. However, the process is relatively labour-intensive, as either a new helical pile must be screwed in place for a surface source, or a new borehole must be drilled for a borehole vibrator. As the objectives of this project are focused primarily on investigating the efficacy of deploying linear vibrators as a monitoring tool, rather than collecting the most complete datasets, only a single source location will be used. Therefore, special consideration must be given to where the sources will be installed at the CaMI FRS.

The target injection interval for Phase 1 of injection is the BBRS, at a depth of 300 m. For the purposes of this project, the BBRS will be targeted for a VSP survey, using straight DAS fibre in the geochemistry well, 30 m northeast of the injector, as the receiver. The geochemistry well, rather than the geophysics well, which contains 3C geophones and both straight and helical DAS fibre, was chosen to be the primary receiver well due to logistics at the CaMI FRS. Instrumentation for the permanent sources will be installed in the classroom at the site (Figure 3-1), and installing the sources closer to the classroom will be simpler, as there will be no obstacles between the

classroom and the source location, and safer, as electrical cables will be away from high-traffic areas at the site. To image the zone of highest CO₂ concentration immediately surrounding the injection well, the permanent sources will be placed along an azimuth passing through both the injector and the geochemistry well. Conveniently, this azimuth also passes through the geophysics well, located approximately 20 m southwest of the injector. This will allow for future comparisons of data acquired with DAS in each of the observation wells.



Figure 3-1: Map of the CaMI FRS showing locations of observation and injection wells and surface infrastructure. Classroom in blue, instrumentation shack in purple.

To determine the offset between the geochemistry well and the permanent source location, a simple raytracing experiment was performed using the FRS velocity model (Figure 3-2) and

codes from the CREWES Matlab toolbox, which rely on the shooting method of raytracing. The shooting method refers to iteratively adjusting the raypath from the specified source location until the receiver location is reached (Yang, 2003). The raytracing experiment was conducted for each of the observation wells, placing receivers at 1 m intervals to simulate DAS fibre in each well. The experiment was also repeated with receivers at 5 m intervals to simulate geophones in the geophysics well. The first simulated DAS receiver was placed at 50 m depth in the velocity model, which represents the fact that DAS data cannot be reliably collected in the uppermost portion of each well. This could be due to slight coiling or winding of fibres in the shallow part of the well.

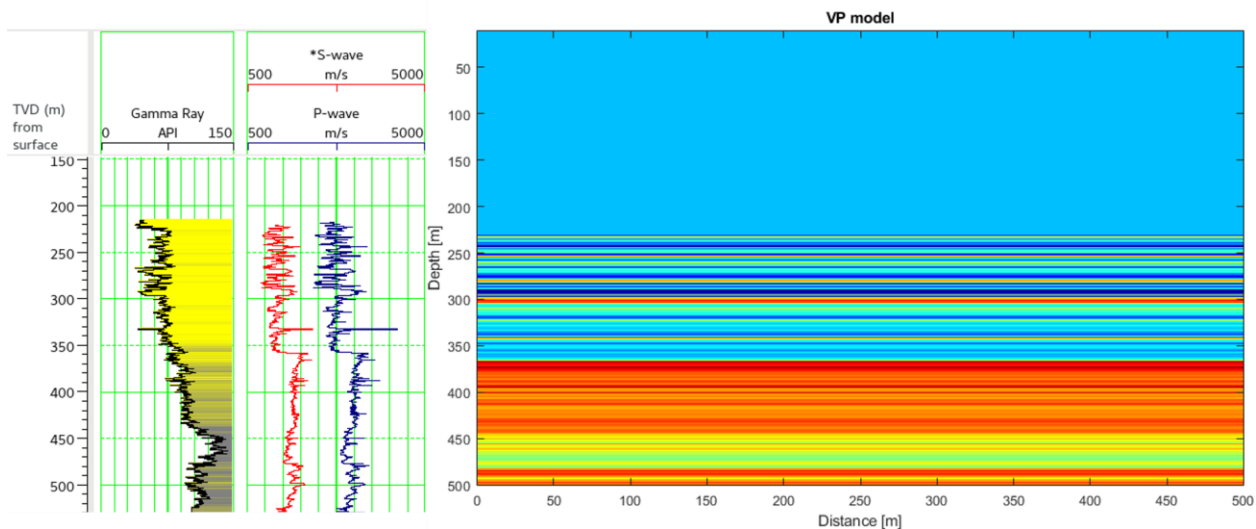


Figure 3-2: CaMI FRS P-wave velocity model derived from 10-22 well logs. Gamma ray and P- and S-wave velocity logs from 10-22 shown.

Given a known velocity model, raytracing, in the context of seismic investigations, refers to describing the pathways of seismic rays through the subsurface (Chander, 1976). In this simple raytracing experiment, a laterally homogeneous “layer-cake” velocity model is assumed. This velocity model is derived from velocity and density well logs recorded in the injector well. Snell’s

Law governs the behaviour of rays incident upon an interface during raytracing experiments (Lines & Newrick, 2004):

$$\frac{\sin(\theta_1)}{v_1} = \frac{\sin(\theta_2)}{v_2} \quad (3.1)$$

Where θ_n is the angle between the ray and a line normal to the interface in one layer, and v_n is the seismic velocity of that layer.

For this raytracing experiment, two objectives were considered in the determination of the offset of the permanent sources:

1. Maximizing the spatial extent illuminated around the injection point; and,
2. Maximizing the range of incidence angles recorded to capture potential amplitude-versus-offset (AVO) effects.

It was found that the maximum source-receiver offset possible was approximately 450 m. Offsets greater than this distance were found to produce critically refracted rays, which occurs when the quantities in Equation (3.1) result in θ_2 greater than or equal to 90° . The incidence angle where θ_2 is equal to 90° is called the critical angle, θ_c :

$$\begin{aligned} \frac{\sin(\theta_c)}{v_1} &= \frac{\sin(90^\circ)}{v_2} \\ \sin(\theta_c) &= \frac{v_1 \times (1)}{v_2} \\ \theta_c &= \sin^{-1}\left(\frac{v_1}{v_2}\right) \end{aligned} \quad (3.2)$$

Raytracing experiments showed that an offset of approximately 110 m between the geochemistry well and the permanent source will optimize both of the above objectives, allowing the zone of highest CO₂ saturation (Macquet et al., 2016) to be imaged. This location results in a source offset of approximately 60 m from the geophysics well (Figure 3-3).

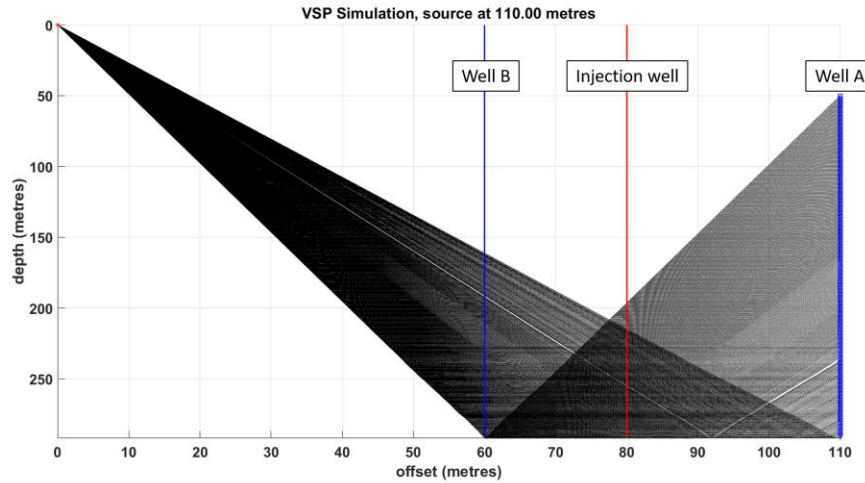


Figure 3-3: Raytracing experiment using FRS velocity model. Well A is the geochemistry well and Well B is the geophysics well. Offset between permanent source and geochemistry well is 110 m.

3.2.1 Impact on DAS

As discussed in Chapter 2, the amplitude recorded by DAS fibre has been determined to vary with the square of the cosine of the angle between the incident ray and the fibre (Mateeva et al., 2013). Simulating DAS receivers in the geochemistry well, it is expected that incidence angles between approximately $13\text{-}25^\circ$ will be recorded. This results in the amplitude of the BBRS reflector being reduced by approximately 4-18% over the depth range of the well when the offset is 110 m. For DAS fibre in the geophysics well, a variation in amplitude of only 2-6% is expected. This is likely due to the shorter offset causing subvertical raypaths for the BBRS reflector, resulting in incidence angles of less than 15° (Figure 3-4).

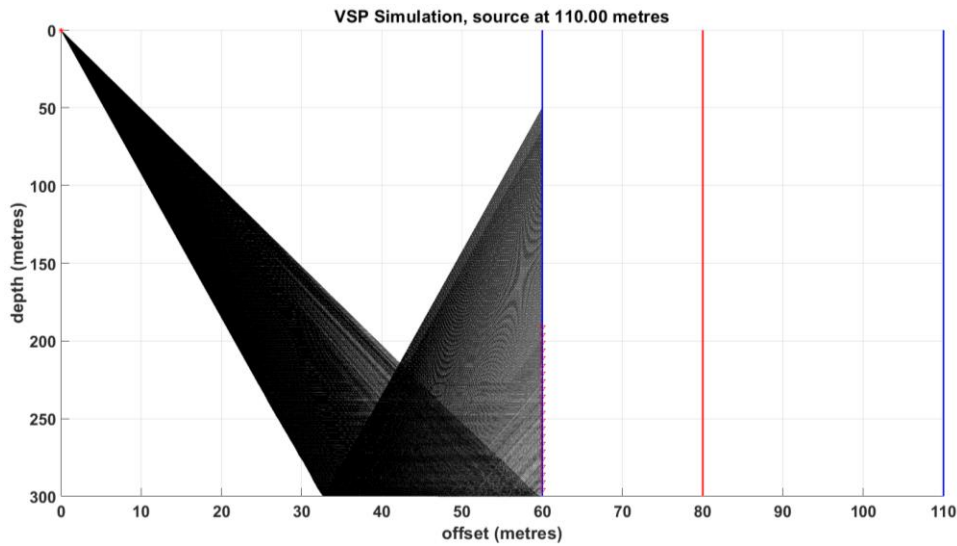


Figure 3-4: Raytracing experiment using FRS velocity model. DAS fibre as the receiver simulated by receivers at 1 m intervals in geophysics well.

3.3 Fluid Substitution

To connect between 1D well log data with 2D or 3D seismic data, synthetic seismograms are used. Synthetic seismograms are generated by using sonic and/or density well logs at a chosen well to create a reflectivity series and convolving the reflectivity series with a chosen wavelet. The sonic and density well logs from the injector well were used to create baseline synthetic seismograms for the FRS. To account for changes in the injection reservoir due to replacement of reservoir fluids with injected CO₂, a fluid substitution was performed to alter the well logs. The Fluid Replacement Modelling (FRM) process in the Hampson-Russell software package was used to generate density, compressional velocity, and shear velocity logs for varying levels of CO₂ saturation based on the density and velocity logs from the injector well. As inputs for the FRM process, the density and velocity well logs were used as the baseline response, along with porosity and mineral volumetric logs to determine the bulk modulus of the rock matrix. The baseline reservoir fluid was assumed to be water with 100% saturation.

The bulk modulus of the reservoir fluid after CO₂ injection was calculated using the Reuss average formula, following simulations performed by Macquet and Lawton (2017). The Brie formula was also tested, resulting in smaller variations in both density and P-wave velocity, which agrees with previous simulation results. For the fluid substitution, a uniform 9% reservoir porosity was assumed, along with water and CO₂ bulk moduli of 2.232 and 0.102 GPa, respectively (Macquet & Lawton, 2017).

By specifying the desired saturation of injected CO₂ to model, density and velocity logs were generated to represent 10%, 30%, and 100% CO₂ saturation cases (Figure 3-5). CO₂ saturations above 30% displayed smaller changes in the P-wave velocity log. The density and P-wave velocity logs show a clear decrease as the CO₂ saturation increases, while the S-wave velocity logs show only a slight increase due to the decrease in density.

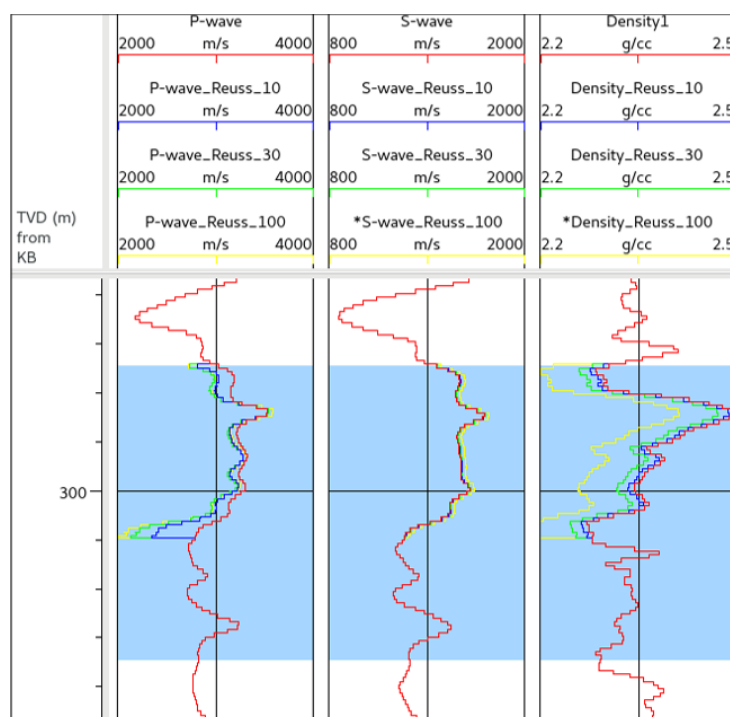


Figure 3-5: Fluid substitution results using Reuss average to model well logs at various CO₂ saturation levels (Red: baseline, green: 10% CO₂, blue: 30% CO₂, yellow: 100% CO₂).

3.3.1 Amplitude versus offset (AVO)

The process of computing synthetic seismograms results in a 1D seismic section representing the theoretical normal incidence seismic response at the well location. To incorporate incidence angles greater than 0° , the CREWES Syngram software package was used. Incidence angles over the range expected from the raytracing experiment were used in the creation of the offset synthetic seismograms. Offset synthetics were generated using the baseline suite of well logs, as well as the resultant well logs from the fluid substitution (Figure 3-6). These synthetic seismograms were generated to understand the amplitude-versus-offset (AVO) response of certain reflectors. AVO refers to how the amplitude of a reflector changes with varying source-receiver offsets and may be indicative of changes in the fluid content or lithology (Schlumberger, 2019). The stack of traces from several offsets was also computed, and the time-lapse anomaly can be observed by taking the difference between the stacks for the baseline and CO₂ saturated cases (Figure 3-7). A strong trough-peak character is observed at the base of the zone used for the FRM, which is indicative of the decrease in P-wave velocity and density observed in Figure 3-5.

The amplitude of the BBRS reflector was extracted for the baseline and post-injection cases, and the AVO curve was plotted for both cases (Figure 3-8). In each case, the amplitude is positive and decreases with increasing incident angle, known as a Class I AVO response (Zhang & Brown, 2001). However, subtle differences in the curves between the two cases may allow the AVO response to be used to determine the presence or absence of injected CO₂ in the reservoir. The intercept, or normal incidence amplitude, for the post-injection case has a higher value than the intercept of the baseline case, and the gradient, or approximate slope of the curve, is greater

than that of the baseline case. The presence of CO₂ could potentially be revealed using these AVO properties.

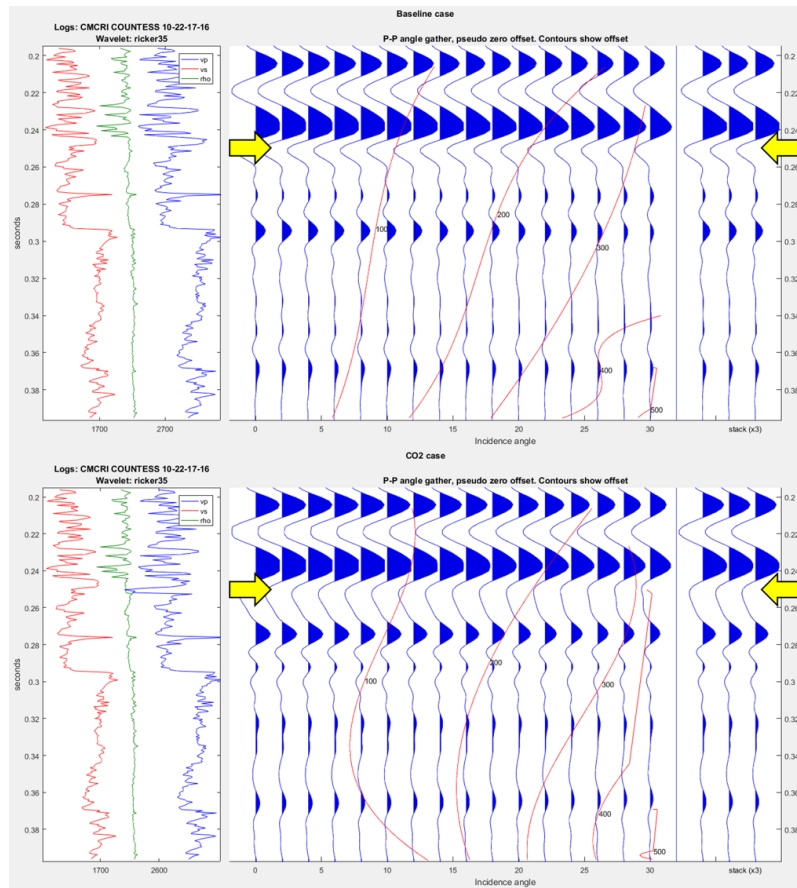


Figure 3-6: Offset synthetic seismograms for the baseline case (top) and 30% CO₂ saturation case (bottom). BBRs reflector identified by yellow arrow. The stack of all offsets is shown by the traces in the right panel of the displays.

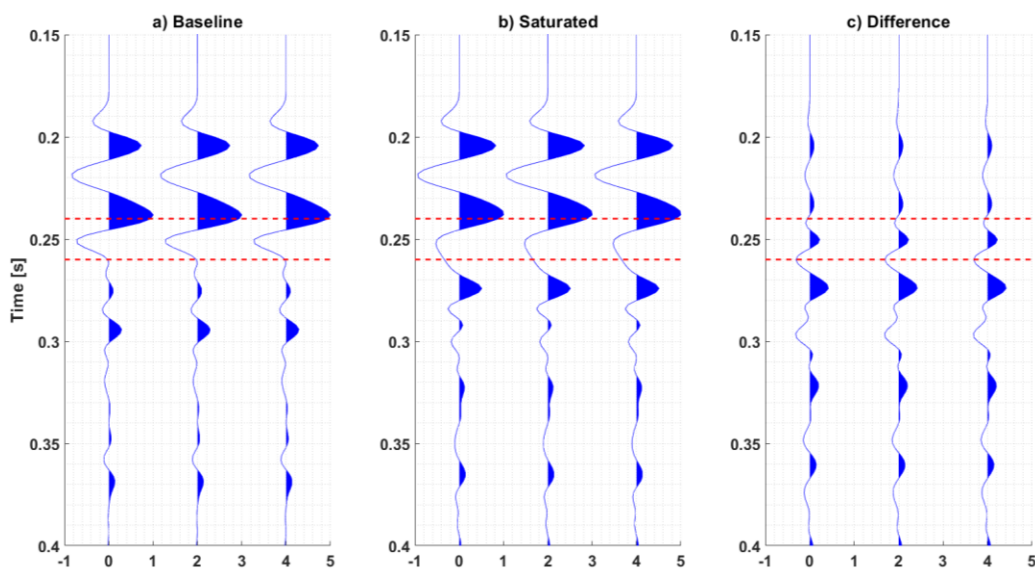


Figure 3-7: Offset synthetic seismogram stacks for the a) baseline and b) CO₂ saturated cases, and the difference (c) between the two stacks. Approximate interval used for FRM identified by red lines.

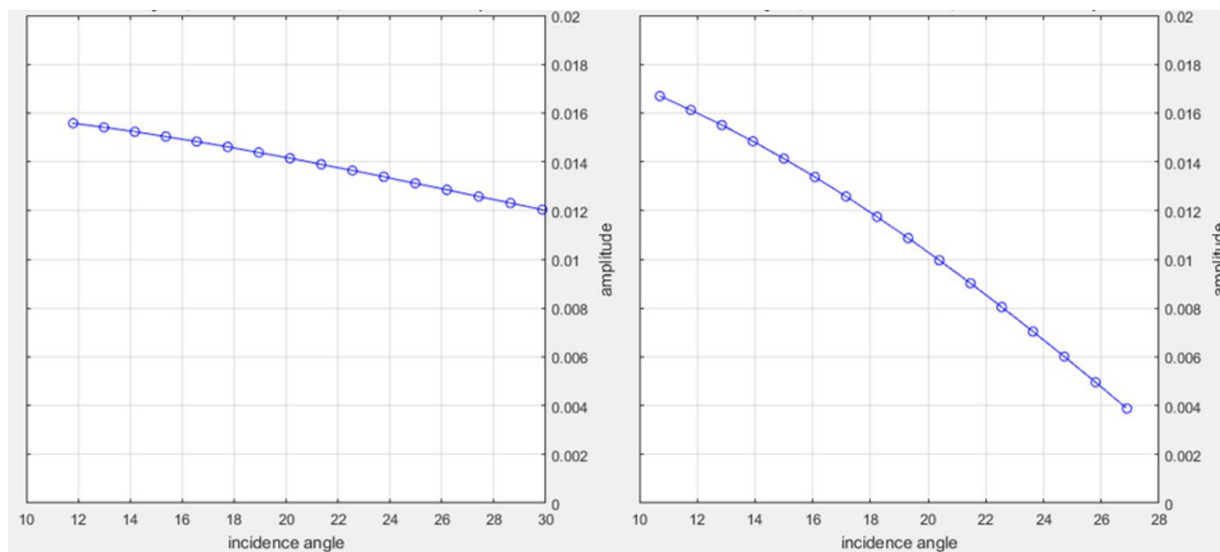


Figure 3-8: AVO curves for baseline case (left) and post-injection case (right).

3.4 Synthetic Data

To compare seismic data acquired with linear vibrators with a theoretical “ground-truth,” the forward problem must be addressed. In seismic studies, the forward problem, also known as

forward modelling, involves taking a set of known variables representing subsurface properties and generating synthetic datasets. In this case, the FRS baseline velocity model is used, along with a known wavelet. A finite-difference simulation is then performed by propagating a delta function through the velocity model, then filtering the result with a wavelet. Forward modelling in this project was first performed with a Ricker wavelet to ensure stability of the algorithm, then repeated with a synthetic permanent source sweep.

Conceptually, seismic acquisition and processing with orbital vibrator sources is very similar to conventional Vibroseis acquisition and processing. One important step in generating usable seismic data when using these sources is the cross-correlation of raw data with the sweep signature. Raw seismic data will have a strong imprint of the sweep signature present at each reflector, and cross-correlating this raw data with the sweep will collapse this imprint to a Klauder wavelet at each reflector.

Consider the convolutional model for generating a seismic trace, $s(t)$:

$$s(t) = w(t) * r(t) \quad (3.4)$$

Where $w(t)$ and $r(t)$ are the wavelet and reflectivity, respectively, as functions of time. The $*$ operator in Equation (3.3) represents convolution. Cross-correlating (\otimes) the trace with the source signature wavelet yields:

$$\begin{aligned} s_{corr}(t) &= s(t) \otimes w(t) \\ s_{corr}(t) &= w(t) * r(t) \otimes w(t) \end{aligned} \quad (3.5)$$

As cross-correlation is a convolutional process, the commutative nature of convolution allows Equation (3.4) to be re-written as:

$$s_{corr}(t) = w(t) * w(-t) * r(t) \quad (3.6)$$

Where $w(-t)$ is the time-reversed wavelet. Put simply, the correlated trace can be generated as a result of convolving the autocorrelation of the wavelet with the reflectivity series. For simplicity, forward modelling in this project was performed using the autocorrelation of a synthetic permanent source sweep, rather than cross-correlating raw synthetic data with the sweep signature.

As described in Chapter 2, the force output, and therefore, the seismic amplitude, of an orbital vibrator source varies with the square of the angular frequency. In the forward modelling of permanent source data in this project, a synthetic sweep was first generated assuming constant amplitude at all frequencies, then scaled by a factor of ω^2 (Figure 3-9). An example sweep was generated using a time-frequency relationship of 0-150 Hz over 25 s for the upsweep segment, with a symmetrical downsweep segment. The autocorrelation of this sweep displays similar characteristics when compared to a conventional Ricker wavelet (Figure 3-10) but displays high frequency oscillations along with a low frequency imprint. This low frequency imprint may have a negative impact on resultant synthetic seismic data.

Acquisition geometry for the finite difference simulation, performed using Matlab codes in the CREWES Toolbox, was set to be a VSP survey, with receivers at 1 m intervals in both the geochemistry and geophysics wells to simulate DAS in these wells, and another set of receivers at 5 m intervals in the geophysics well to simulate the 3C geophones in that well. As a result of the raytracing experiment, the source was placed 109 m away from the simulated geochemistry well and 59 m from the simulated geophysics well (Figure 3-11).

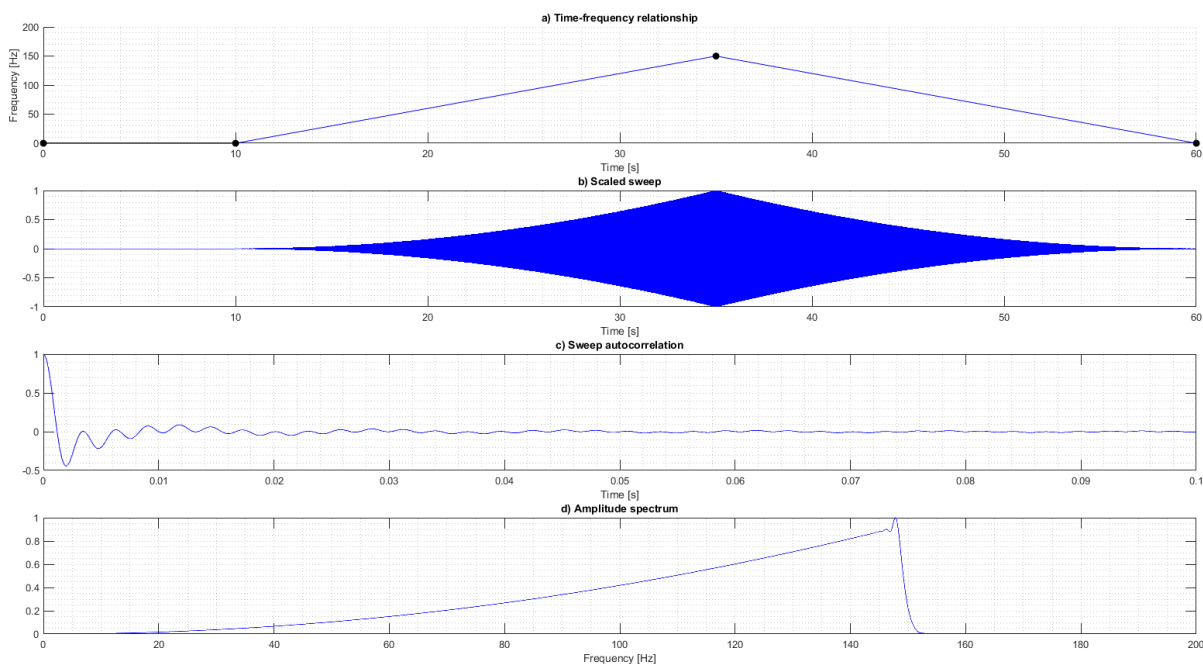


Figure 3-9: Time-frequency relationship (0-150-0 Hz over 50 s) for example synthetic permanent source sweep (a); synthetic sweep scaled by factor of ω^2 (b); positive lags of synthetic sweep autocorrelation (c); synthetic sweep amplitude spectrum (d).

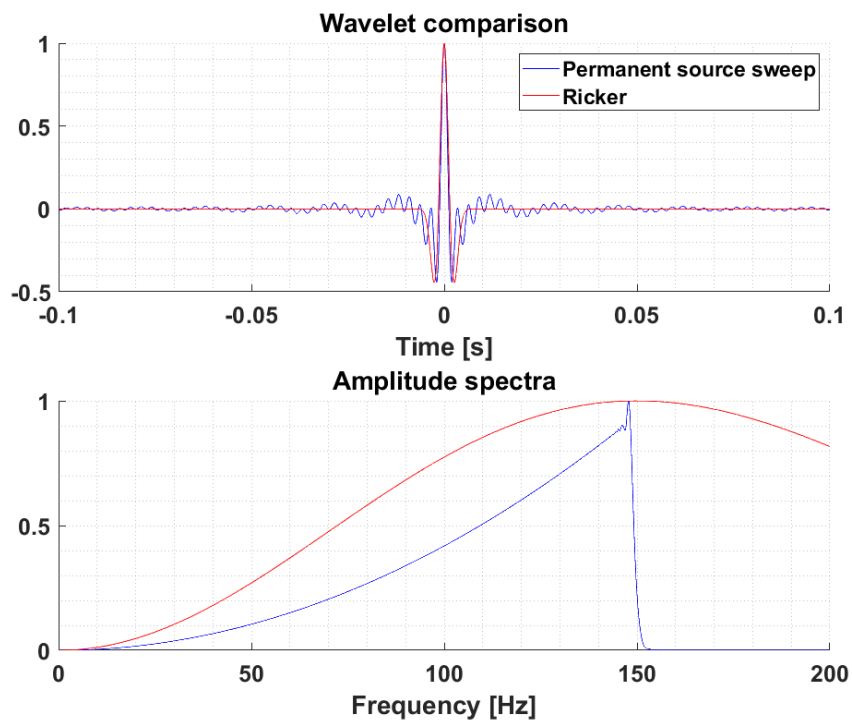


Figure 3-10: Comparison of synthetic permanent source sweep autocorrelation (blue) and 150 Hz Ricker wavelet (red).

Synthetic VSP data were generated using both the synthetic permanent source sweep and a Ricker wavelet with 150 Hz dominant frequency, and for each of the geophysics and geochemistry wells (Figure 3-12). Prominent reflectors, including the BBRS injection interval, are visible on the VSP sections created with both wavelets. Resolution appears to have improved on sections created using the higher-frequency permanent source sweep compared to the Ricker wavelet. However, the permanent source sections show a strong low frequency imprint with a “ringy” character. This character is not observed on the Ricker wavelet sections. It is anticipated that this low frequency ringiness will be observed in field data acquired using linear vibrators and will need to be accounted for during the processing of permanent source data. The synthetic VSP data was then subsequently processed, resulting in a corridor stack for each synthetic dataset (Figures 3-13 and 3-14). The corridor stacks (Figure 3-15) for each source type are similar in character, and the BBRS interval can be identified. However, the ringy character observed on the raw VSP data appears to have remained through the data processing workflow and is evident on the permanent source corridor stack.

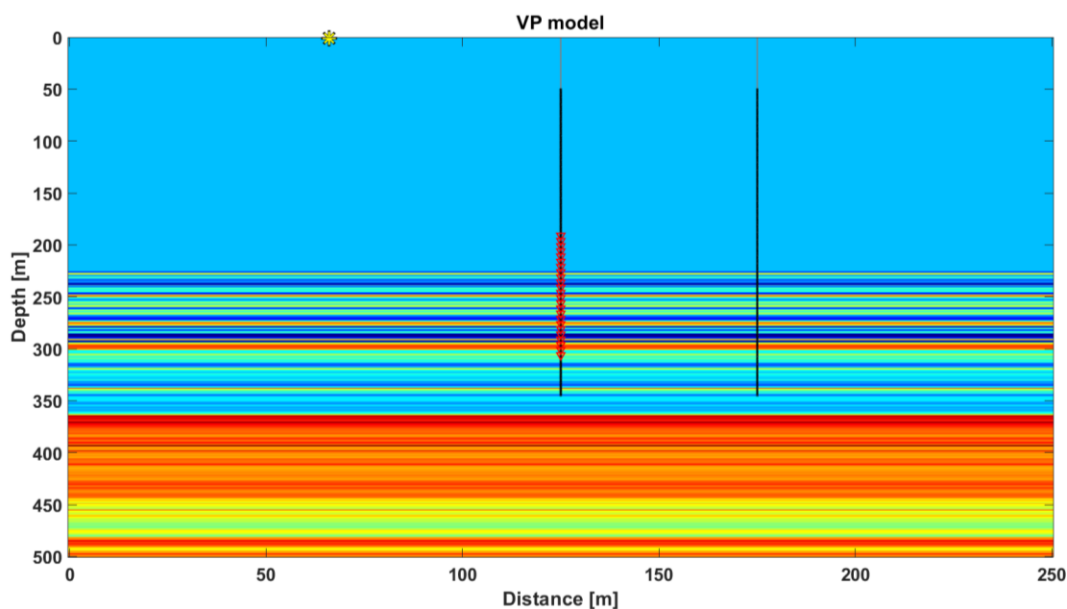


Figure 3-11: CaMI FRS P-wave velocity model with finite-difference simulation acquisition geometry overlain. Source location (yellow star) located 59 m from geophysics well (centre of figure) and 109 m from geochemistry well. Geophones in geophysics well identified by red inverted triangles. DAS receivers identified by black circles.

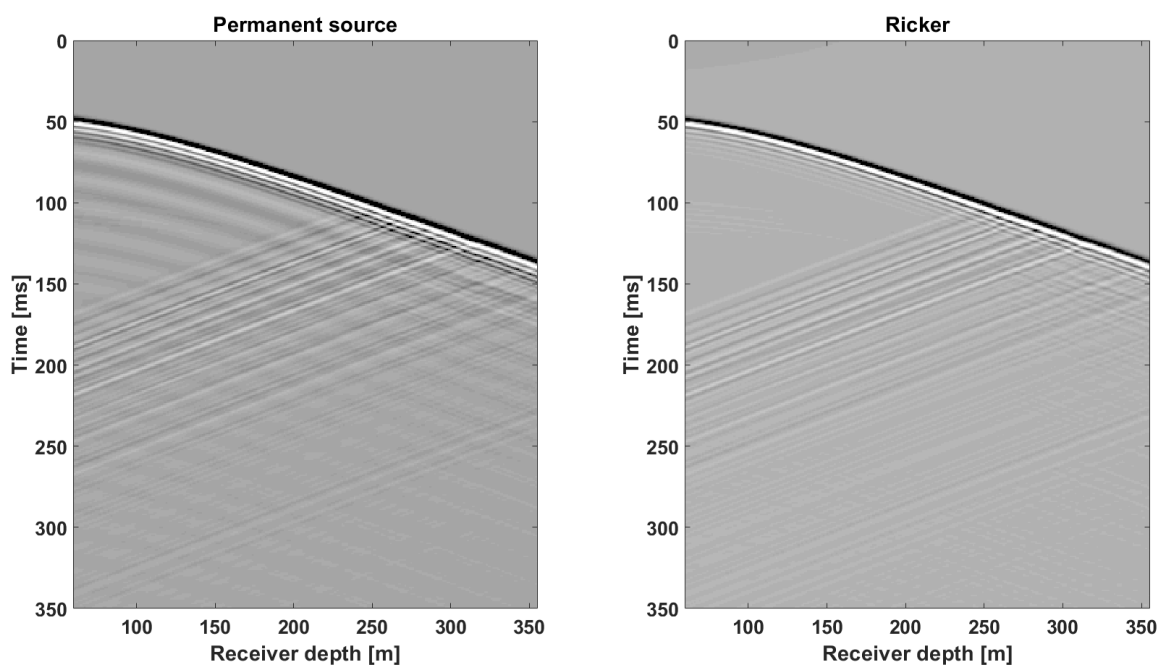


Figure 3-12: Results from finite-difference simulation using FRS P-wave velocity model. Source signature used were a synthetic permanent source sweep (left) and 150 Hz Ricker wavelet (right).

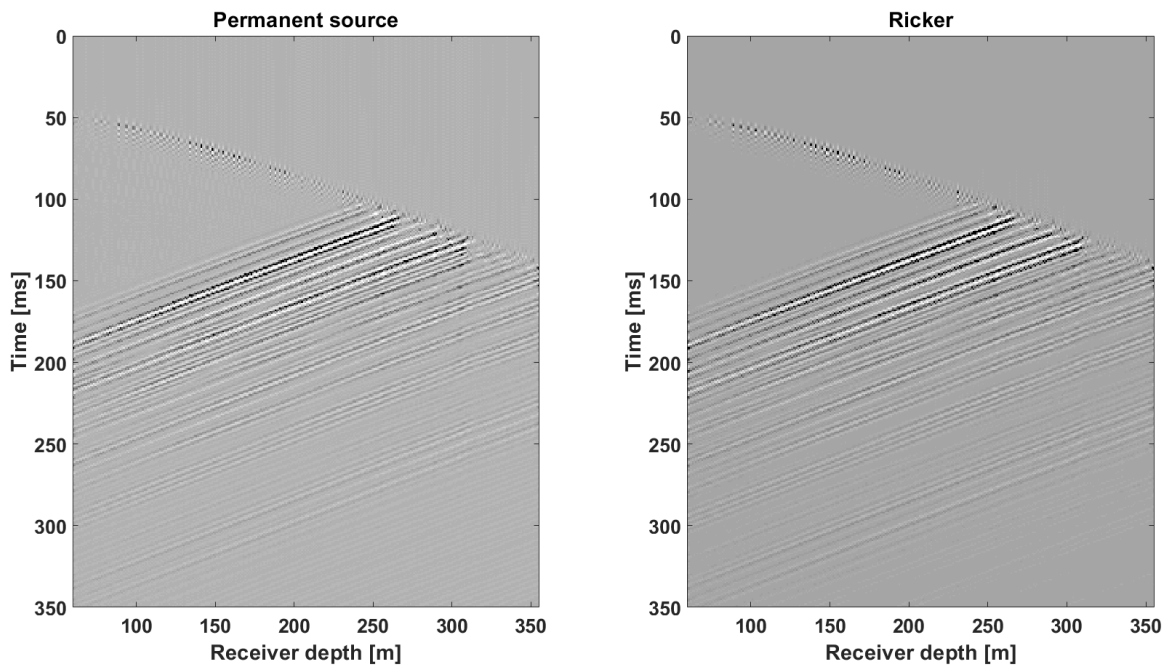


Figure 3-13: Upgoing wavefield from synthetic VSP data from finite-difference simulation for synthetic permanent source sweep (left) and 150 Hz Ricker wavelet (right).

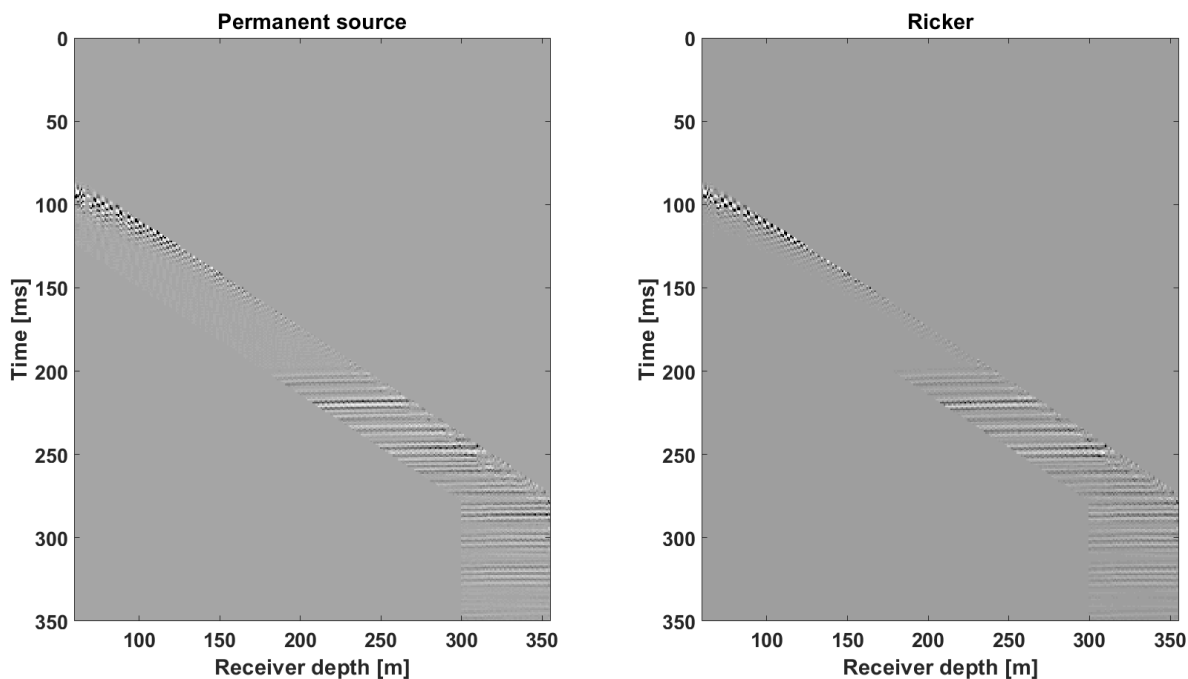


Figure 3-14: Outside corridor from synthetic VSP data from finite-difference simulation for synthetic permanent source sweep (left) and 150 Hz Ricker wavelet (right).

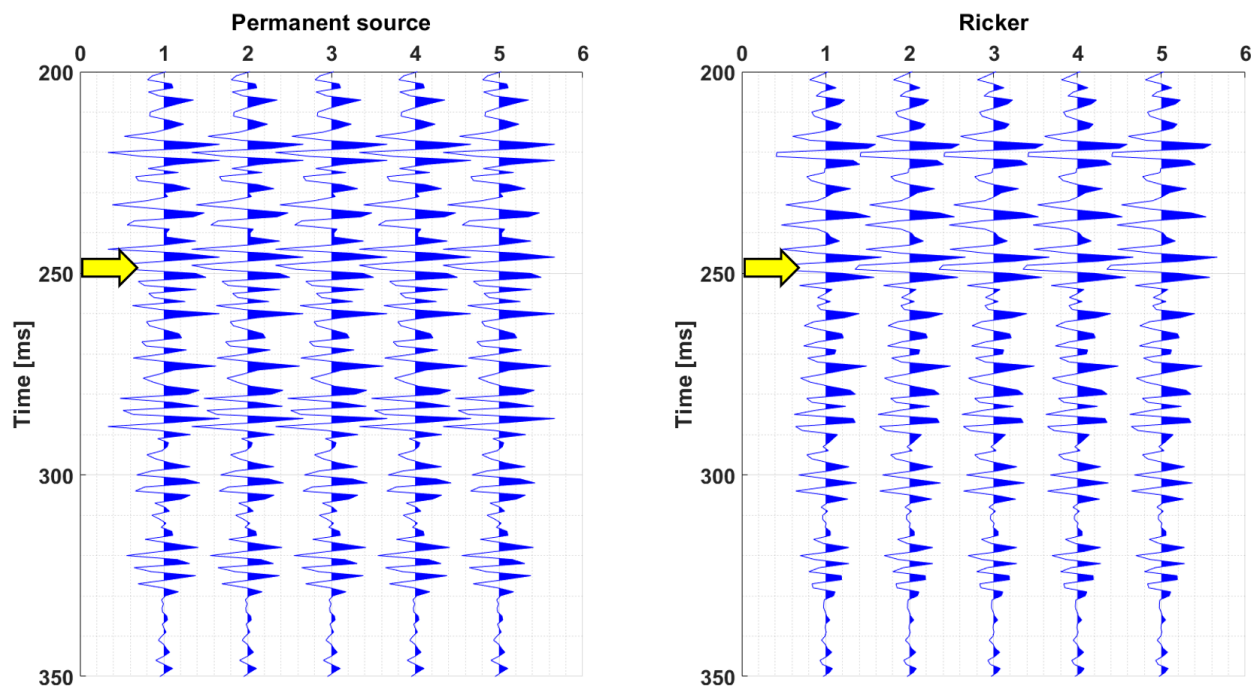


Figure 3-15: Corridor stacks from synthetic VSP data from finite-difference simulation for synthetic permanent source sweep (left) and 150 Hz Ricker wavelet (right). Approximate BBR interval identified by arrows.

Chapter 4 – Baseline Data

4.1 Introduction

In addition to computing synthetic seismic data through finite difference simulations, baseline datasets acquired with more well-understood tools will be compared against seismic data acquired with GPUSA linear vibrators in this chapter. These tools include Vibroseis sources and conventional 1C or 3C geophones. Utilizing a well-understood Vibroseis source also allows for the testing of seismic acquisition with DAS fibre as the receiver. Several seismic field acquisition programs have been conducted at the CaMI FRS. This chapter will describe three of the field experiments and will discuss the data processing workflows applied to the acquired data. A VSP processing workflow is designed and streamlined to be readily applied to future VSP datasets acquired with a linear vibrator source.

4.2 May 2017 2D Line

In May 2017, a 2D seismic line was acquired at the FRS, and was subsequently processed in October 2017 to serve as a large-scale baseline dataset to compare against data acquired with linear vibrator sources. The survey was acquired along the 1.1 km trench passing across the FRS from southwest to northeast. The source for this survey was the CREWES Envirovibe (Figure 4-1) using a 10-150 Hz sweep over 16 s with a 2 s listen time. The source interval was 10 m at the southwestern and northeastern ends of the survey line, with 20 m spacing in the central portion of the line. Multicomponent (3C) geophones were used as receivers, placed at 10 m intervals along the line (Figure 4-2). Source and receiver station elevations are shown in Figure 4-3 and show a variation of only 2 m. Only the vertical component recorded by the 3C geophones was processed.



Figure 4-1: The CREWES Envirovibe, used as the source for baseline seismic datasets (CREWES, 2011).

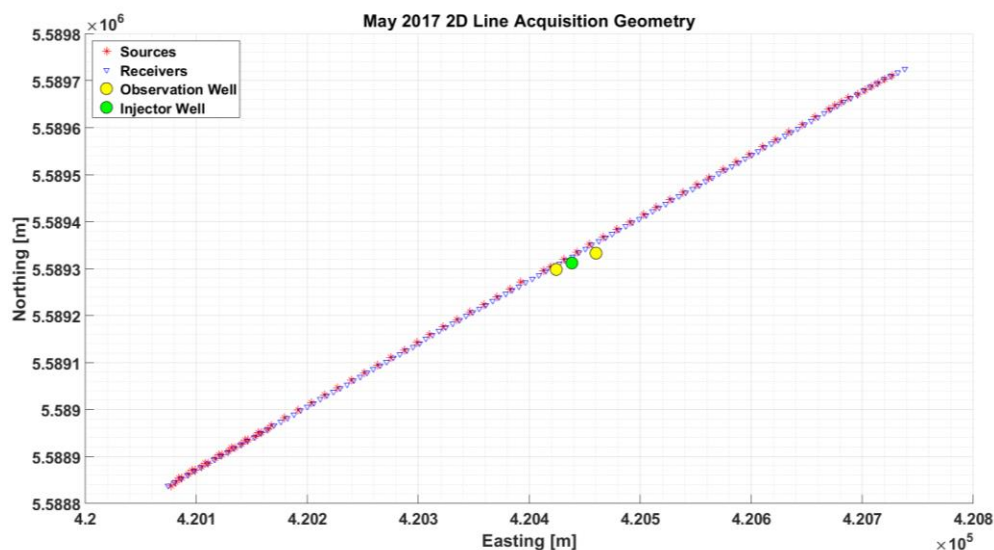


Figure 4-2: Source and receiver acquisition geometry for May 2017 2D seismic line acquisition. Observation and injection well locations indicated on the map.

An example shot record (Figure 4-4) from the southwestern end of the line (station 101) shows the data are of good quality, with deeper reflectors readily visible. However, from the computation of synthetic seismograms and forward modelling of synthetic data, the BBRS reflector is known to occur at reflection times of only 250-300 ms. The BBRS data are significantly

obscured by sources of noise on the shot record. Therefore, processing of this dataset will attempt to emphasize the shallow reflectors.

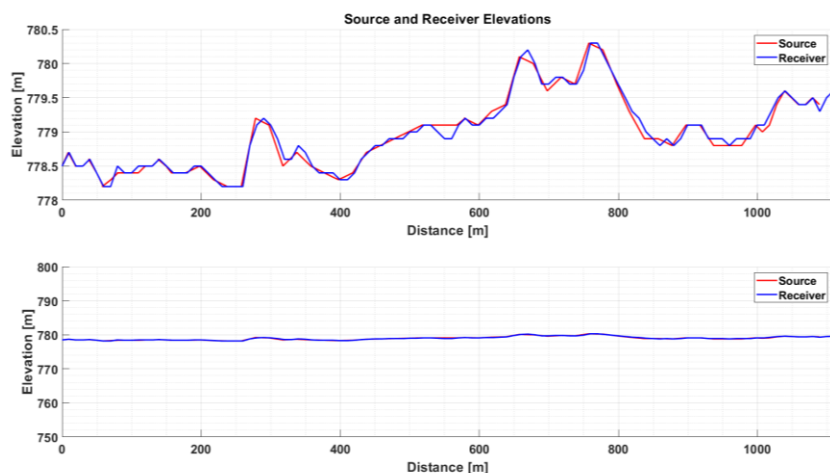


Figure 4-3: Source and receiver elevations for May 2017 2D line acquisition program.

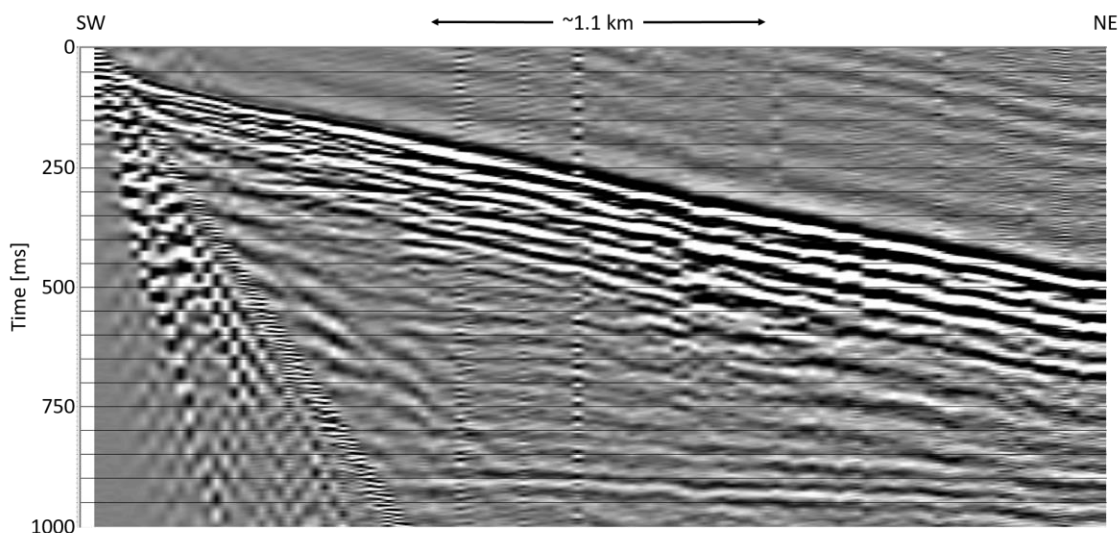


Figure 4-4: Example shot record from station 101 (southwest end of line). Deeper reflections are noticeable at approximately 900 ms. BBR interval between 250-300 ms.

The data processing flow used similar methods and parameters from previous seismic processing projects at the FRS (Isaac and Lawton, 2014b). The workflow (Figure 4-5) follows a conventional approach for processing data acquired in the Alberta Plains, where reflectors are

predicted to have minimal dip. To enhance shallow reflectors, a spatial median filter was applied to stacked data (Figure 4-6) prior to migration. The final migrated 2D section shows reasonable reflection quality from the BBRS interval (Figure 4-7). Significant curving of reflectors, or migration artifacts, are observed near the edges of the section due to the short length of the profile. Similar behaviour is also observed in the results of prior processing (Isaac & Lawton, 2014b).

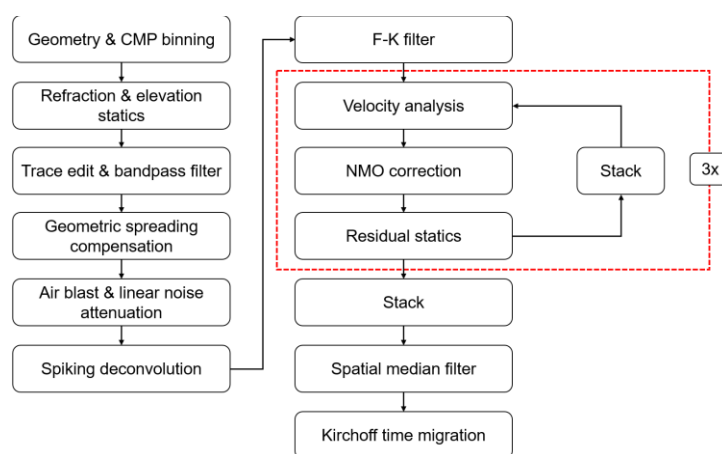


Figure 4-5: Data processing workflow for May 2017 2D line.

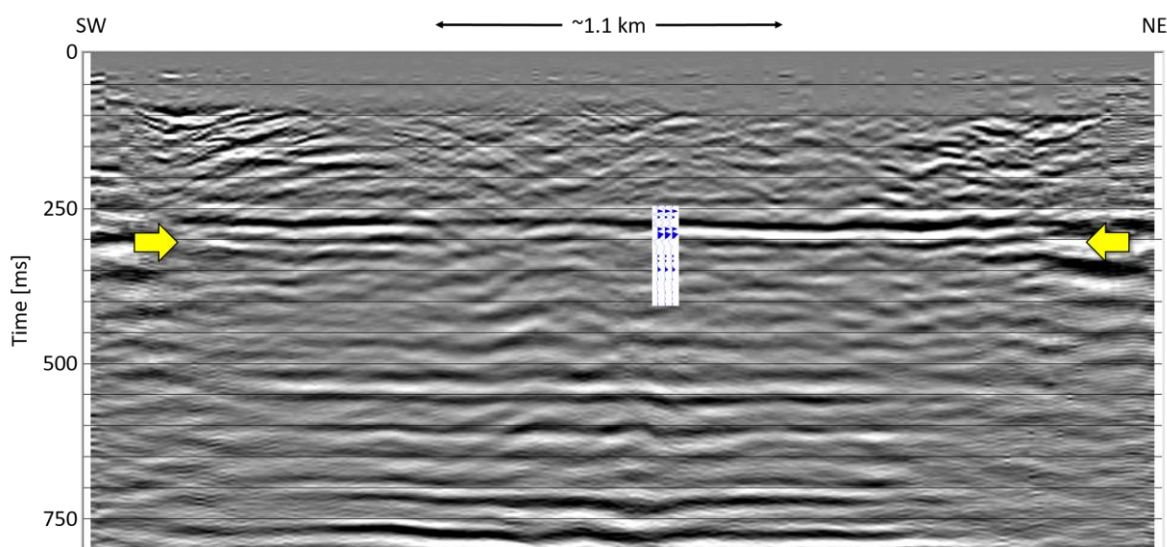


Figure 4-6: Stacked 2D line from May 2017 after application of 5-point spatial median filter to enhance shallow reflectors. BBRS between 250-300 ms. Shown with synthetic seismogram tie.

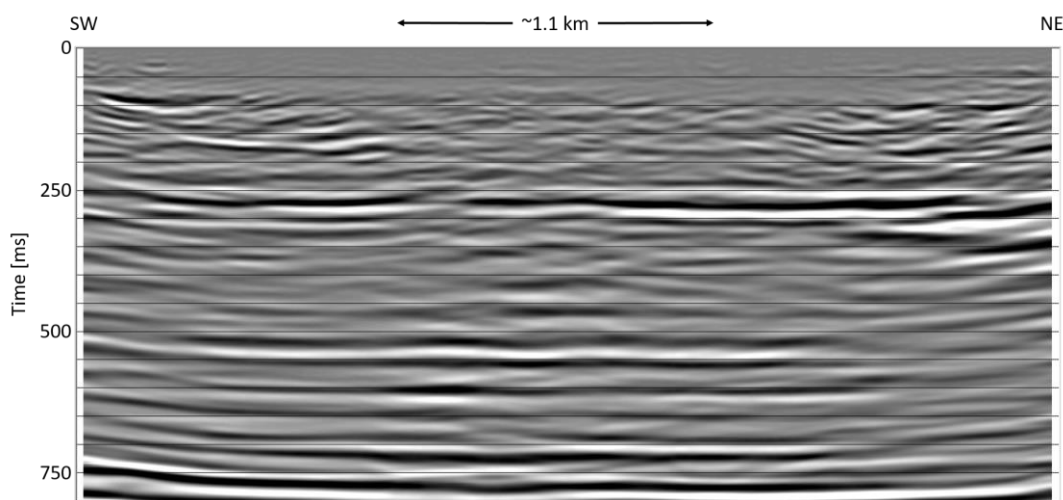


Figure 4-7: Final migrated 2D line from May 2017 survey.

4.3 Baseline VSP

In May and July 2017, several VSP datasets were acquired at the CaMI FRS using the CREWES Envirovibe as the source with a 10-150 Hz sweep. The DAS fibre loop at the site was used to record data, in addition to buried 3C geophones in the geophysics well. The 24 3C geophones are permanently installed in the geophysics well at 5 m intervals from approximately 191-306 m depth. While the entire fibre loop at the site was used, only the straight fibre segments in both the geophysics and geochemistry wells were considered for this project. The DAS and geophone data from both surveys were used to develop a VSP seismic data processing workflow for future datasets acquired using GPUSA linear vibrators, as well as to act as a baseline dataset to compare against repeated VSP surveys at the site.

Data were acquired during the survey using several source locations. However, only selected shot points (Figure 4-8) were used in the development of a VSP data processing workflow. These shot points were selected to approximate the location where the GPUSA linear vibrators were later installed based on the raytracing and forward modelling performed (Chapter 3).

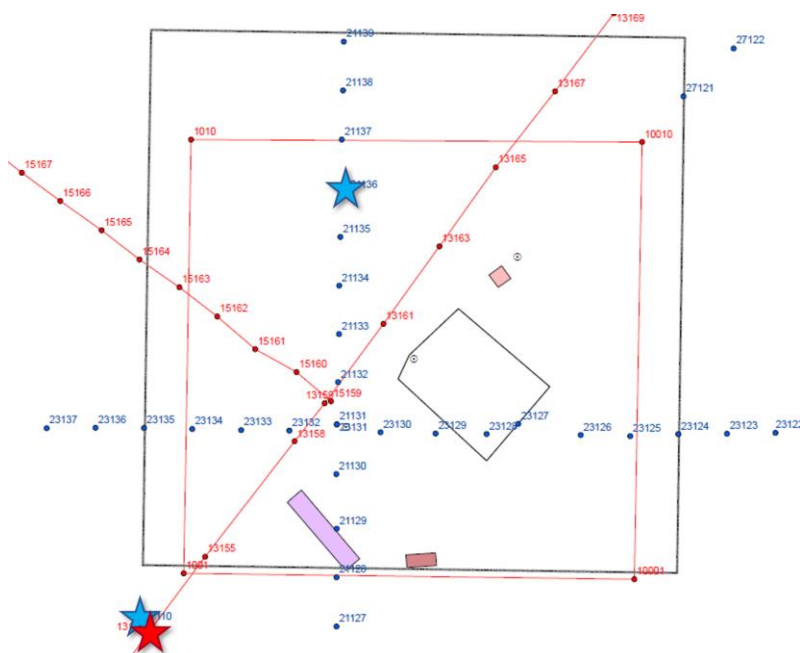


Figure 4-8: Source locations for baseline VSP datasets. Source locations for May 2017 survey (red) and July 2017 survey (blue) shown. Selected source locations for processing identified with stars.

4.3.1 Baseline geophone VSP

To compare geophone and DAS data from straight fibre in the geophysics well, only the vertical component from the 3C geophones was considered. Shot point 27110, represented by the blue star in the lower left of Figure 4-8, was selected to approximate the offset between the permanent source and the observation wells, with an offset of approximately 58 m between the source location and the geophysics well. Raw data are of good quality; however, 4 of the 24 vertical component traces malfunctioned, producing noisy traces (Figure 4-9). These traces were killed and interpolated, using simple linear interpolation from adjacent traces, before further analysis (Figure 4-10). Strong downgoing and upgoing wavefields are visible in the data.

The signal-to-noise ratio (SNR) for the raw data was estimated to be roughly 32.5, computed using a method based on the work of Kragh and Christie (2002), and of Correa et al.

(2018). This method is based on computing the root-mean-square (RMS) amplitude of a trace in a particular window (Kragh & Christie, 2002; Equation 4.1):

$$RMS(x_t) = \sqrt{\frac{\sum_{t_1}^{t_2} (x_t)^2}{N}} \quad (4.1)$$

Where x_t is a chosen time series (i.e. a seismic trace), t_1 and t_2 define the bounds of the window, and N is the number of samples in the window.

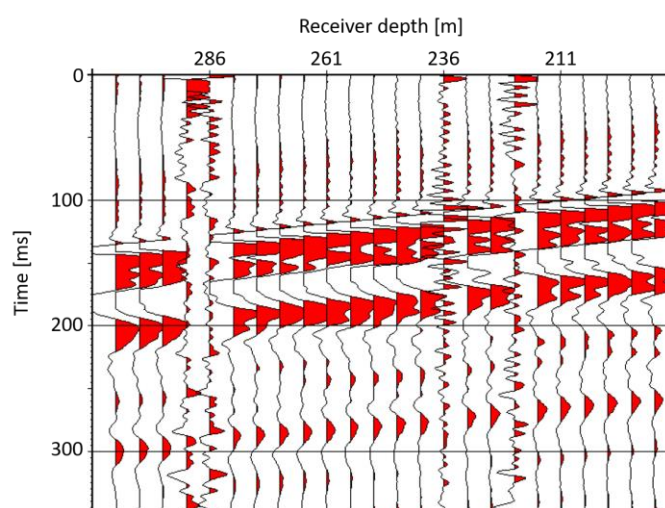


Figure 4-9: Vertical component of geophone data from shot point 27110 (approximately 58 m offset). Automatic gain correction (AGC) applied. Noisy traces observed on record.

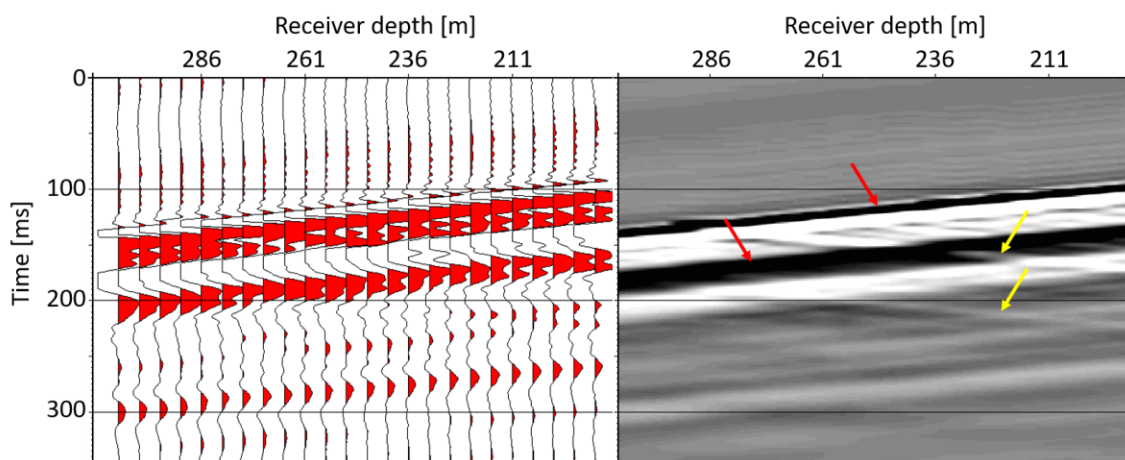


Figure 4-10: Interpolated vertical component of geophone data from shot point 27110. Downgoing wavefield (red) and upgoing wavefield (yellow) identified by arrows.

The signal component was estimated by computing RMS amplitude of a particular trace in a 50 ms window around the picked first arrival time on the recorded VSP section. Similarly, the noise component was estimated by computing the RMS amplitude of the first 50 ms of the trace. The signal component was divided by the noise component of each trace, and the SNR of the section was estimated by taking the median of these individual SNR values.

After picking the first breaks and estimating the SNR, a velocity profile was generated using the first break times and the depth of the corresponding geophone for each first break pick (Figure 4-11). Next, the VSP shot record was flattened by computing the difference between the first break time for each trace and a chosen reference time. The traces are then shifted by the calculated difference such that the first break times are aligned on the reference time, chosen to be 100 ms in this case. To isolate the downgoing and upgoing wavefields, a 5-point median filter is applied to the flattened record. The filtered record gives the downgoing wavefield, which is then subtracted from the flattened total wavefield to give the upgoing wavefield (Figure 4-12).

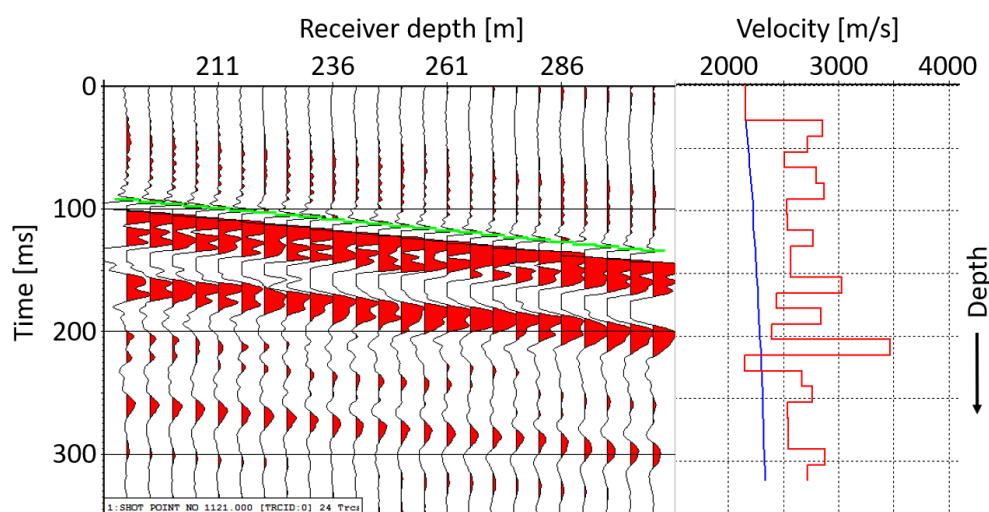


Figure 4-11: Vertical component of geophone data with first break picks overlain (green). Velocity profile shown on right. RMS velocity (blue) and interval velocity (red) displayed.

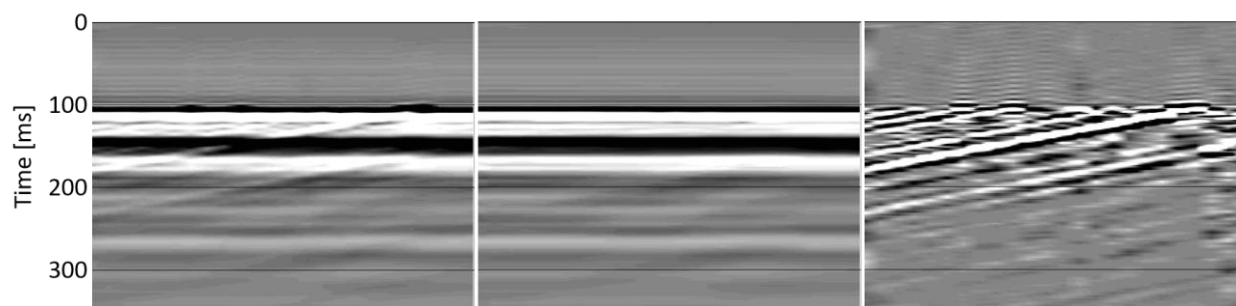


Figure 4-12: Flattened total wavefield (left), flattened downgoing wavefield (centre), and upgoing wavefield (right) from vertical component of geophone data.

In VSP datasets, the upgoing wavefield contains primary reflections from subsurface reflectors, in addition to upgoing multiple reflections. The downgoing wavefield can also contain multiples, but is typically thought to represent the source signature, as waves will travel downwards from the source directly to receivers in the well. Therefore, the downgoing wavefield can be used to design a deconvolution operator, which can then be applied to the un-flattened upgoing wavefield. In this case, the deconvolution operator was chosen to be 240 ms long. Following deconvolution, an F-K filter was applied to remove any residual downgoing energy (Figure 4-13). Normal moveout (NMO), is compensated by using the velocity profile derived previously from the first break picks. Each trace is then shifted down by the first break time, resulting in a section with the same time axis as a surface seismic section, or two-way time (TWT; Figure 4-14). The outside corridor is then isolated and stacked, resulting in the final corridor stack. The final corridor stack shows good agreement in character with a zero-offset synthetic seismogram calculated from injector well logs, albeit with a slight time shift of approximately 5-10 ms (Figure 4-15). This data processing workflow (Figure 4-16) will be used as a foundation to process DAS datasets, as well as datasets acquired with permanent sources.

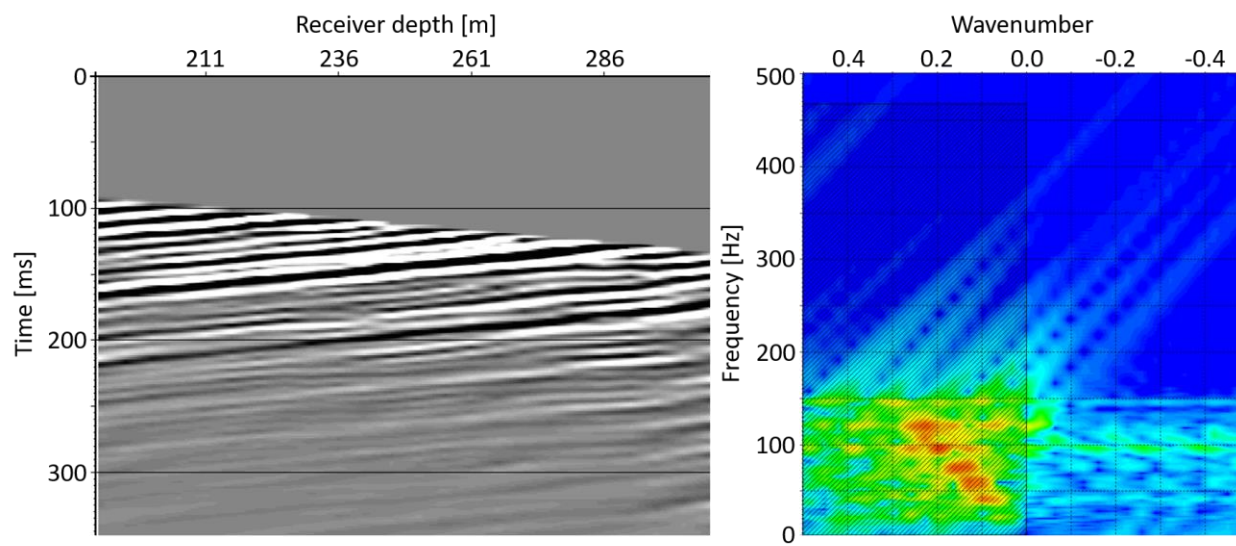


Figure 4-13: Upgoing wavefield (left) after VSP deconvolution with the downgoing wavefield and F-K filter (right) to remove residual downgoing energy. Data within the shaded region on the F-K plot was passed through the filter.

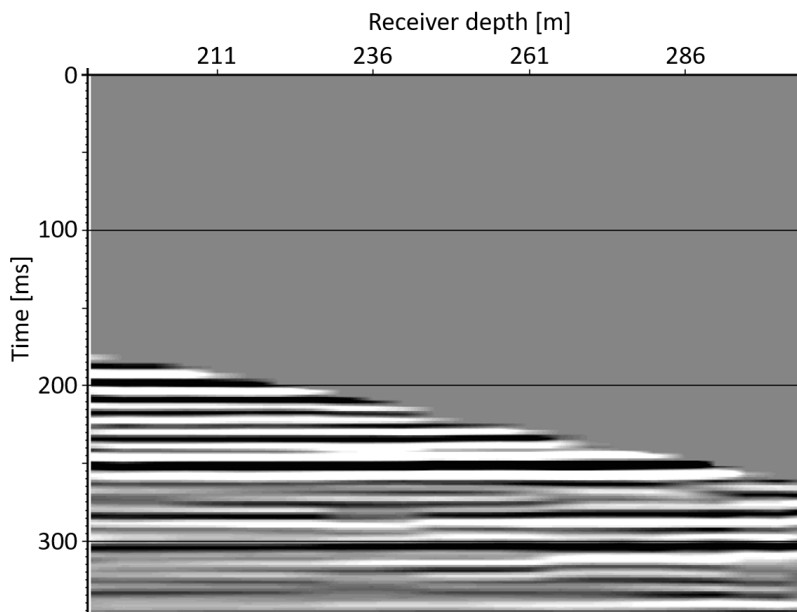


Figure 4-14: Upgoing wavefield after VSP deconvolution and NMO correction. Displayed in TWT.

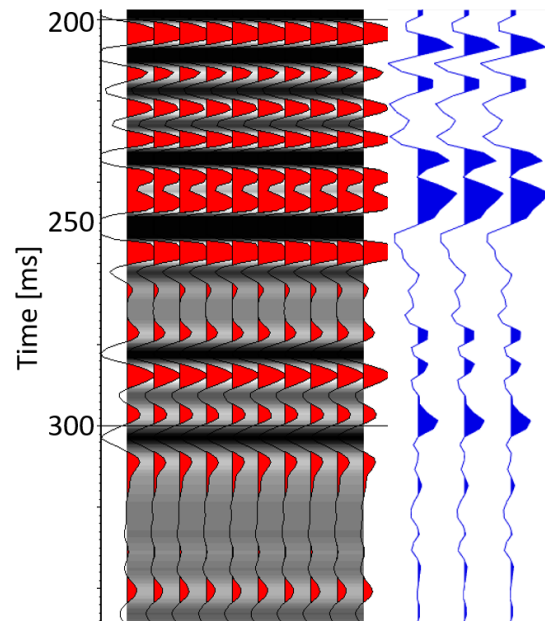


Figure 4-15: Comparison of geophone corridor stack (left) and synthetic seismogram (right), generated with a 10-150 Hz synthetic Vibroseis sweep.

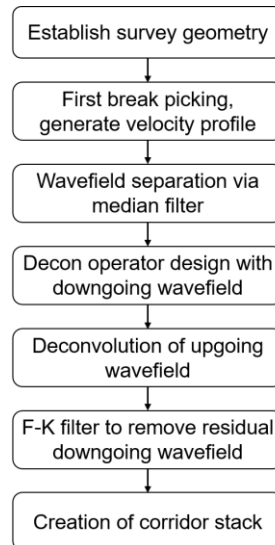


Figure 4-16: VSP data processing workflow.

4.3.2 Baseline DAS VSP

A DAS VSP dataset was selected with similar offset to the geophone VSP dataset to develop a better understanding of the differences between the two receiver types, as well as to

adapt the existing processing flow to DAS surveys. The survey used source locations parallel to the fibre trench crossing the site, with the maximum vertical fold (i.e. number of sweeps) of 3. The source location selected, shot point 13153, is located approximately 58 m southwest of the geophysics well. The DAS survey used a gauge length of 10 m and assumed a channel spacing in the fibre of 25 cm (Hall et al., 2017). The deepest DAS channel is located at 343.8 m.

The shot record for the entire fibre loop (Figure 4-17) shows clear downgoing primary wavefields for straight fibre in the geochemistry well, as well as both helical and straight fibre in the geophysics well. The “V”-shape of the data in each of the wells (Figure 4-18) represents the downgoing and upgoing segments of the fibre. A slight dimming in the downgoing first breaks on the helical fibre in the geophysics well compared to straight fibre can be observed. Additionally, the upgoing primary wavefield appears to be more prominent on the straight fibre than the helical fibre. These observations agree with previous investigations (Gordon & Lawton, 2018). The data from both helical and straight fibre in the trench shows little to no response, as vertical rays incident on the fibre will be subnormal, thus due to broadside insensitivity, the recorded amplitude will be low.

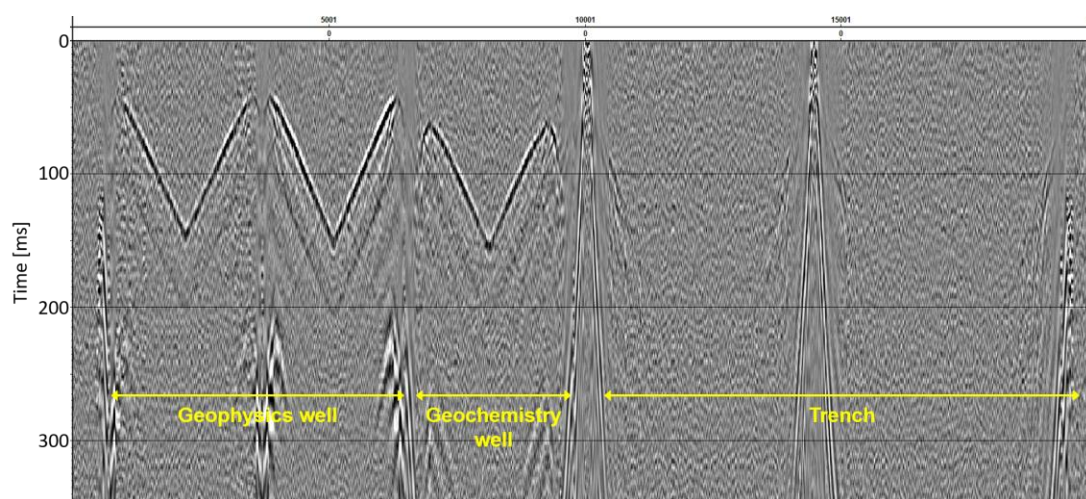


Figure 4-17: Seismic data using full DAS fibre loop from shot point 13153. AGC applied.

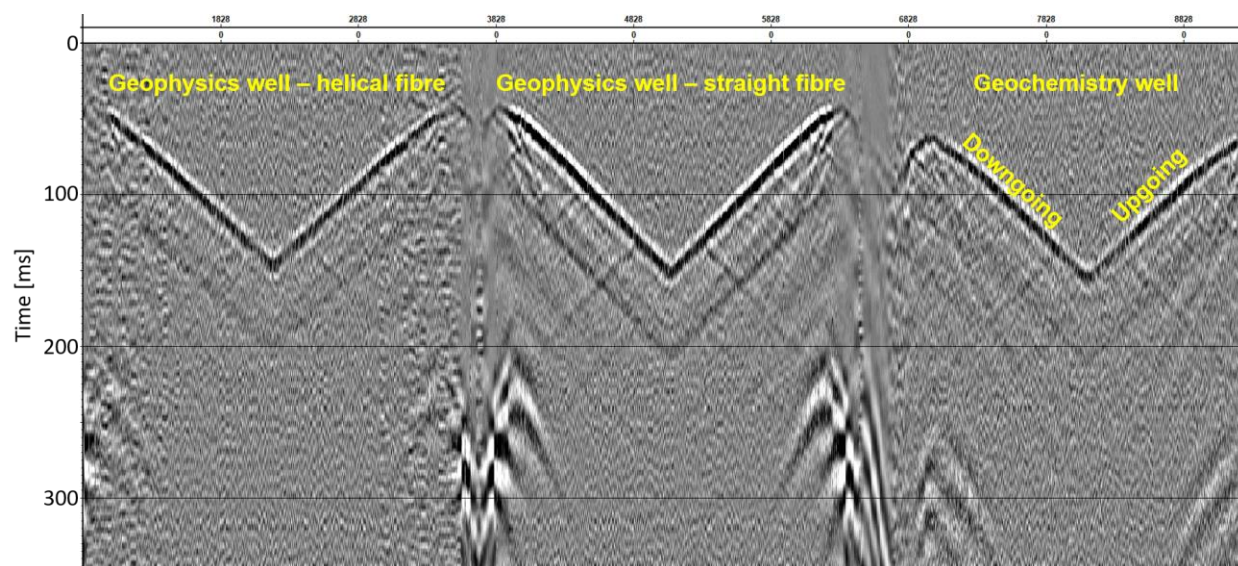


Figure 4-18: DAS seismic data from observation wells. “V”-shape of first breaks from upgoing and downgoing segments of fibre in each well. Noticeable dimming of data on helical fibre data compared to straight fibre. AGC applied.

To compare against the geophone VSP recorded at similar offset, the downgoing portion of the straight fibre in the geophysics well was isolated. The data for this portion was then clipped such that the depth of the first channel was 50 m. This was done to accommodate for the shallowest traces, where first arrival times appear to decrease with increasing depth (Figure 4-19). This results in a dataset with 1176 traces over a 294 m interval, compared to the geophone data with 24 traces over a 115 m interval. Therefore, the DAS VSP has nearly 20 times the number of channels over the same depth interval, representing an extremely densely sampled dataset.

The SNR for the truncated DAS VSP was estimated using the same method as for the geophone VSP. Calculation of the estimated SNR for the DAS VSP required preliminary manipulation of the data in order to achieve reliable and consistent first break picks. Initial first break picks were erratic, and only very generally followed the trend of first arrivals observed on the shot record. To accommodate for this, a 47-point median filter was applied to the first break

picks (Figure 4-20), resulting in a series of first break times that more closely follows the first arrivals on the shot record. The median SNR for traces in this shot record was estimated to be approximately 2.5, significantly lower than geophone data from the same offset. Visually comparing the DAS and geophone shot records confirms this, as significant background noise, potentially optical noise in the fibre, is observed on the DAS record. The discrepancy in estimated SNR between the geophone and DAS datasets could be due to seasonal differences in near-surface conditions during acquisition (Hall et al., 2017), but is more likely due to the inherently lower SNR of DAS fibre.

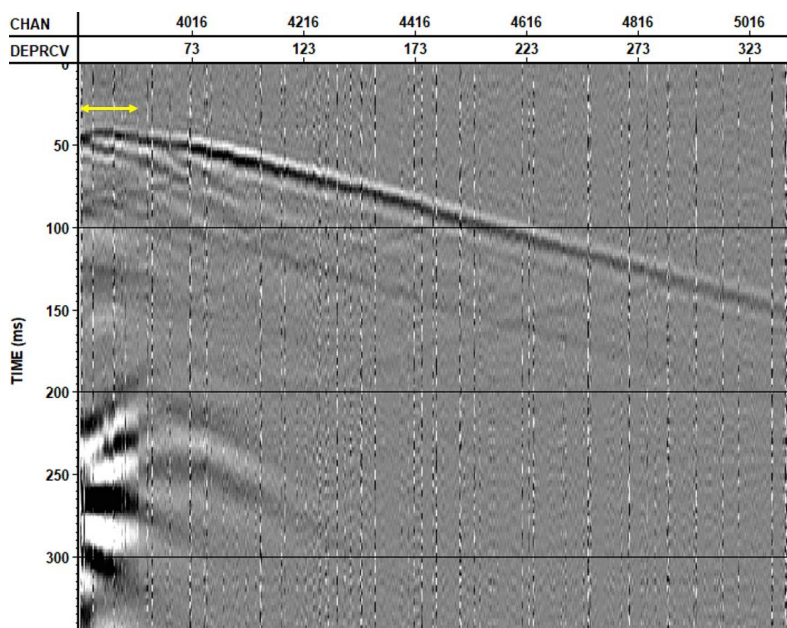


Figure 4-19: Raw DAS data from straight fibre in geophysics well. Depth segment to be removed identified by arrow. Several noisy channels observed.

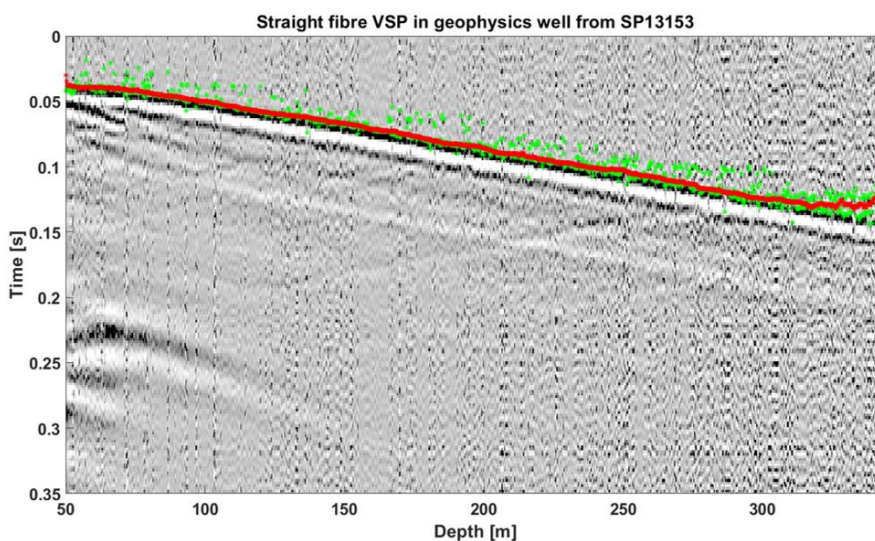


Figure 4-20: Straight fibre VSP in geophysics well with first break picks before median filter (green) and after median filter (red).

The data processing flow developed for the geophone data was applied to the DAS data, with some slight modifications. The data were first resampled spatially from 25 cm to 1 m intervals, and noisy traces on the resultant dataset were killed and interpolated (Figure 4-21). Qualitatively, the resultant image appears clearer than the raw dataset, with a more noticeable upgoing wavefield and fewer traces dominated completely by noise. However, quantitatively, the median trace SNR estimate only improved from 2.5 to 2.7, roughly an 8% increase.

Wavefield separation was performed using the same median filtering technique as with the geophone data. However, the resultant data still appears quite noisy. Following deconvolution, using the same method and parameters as for the geophone data processing, an F-K filter was applied to remove residual downgoing energy, resulting in a record with cleaner and more coherent reflectors (Figure 4-22). The remainder of the data processing flow was identical to that of the geophone data, and the character of the resultant corridor stack (Figure 4-23) agrees with both

synthetic seismograms and the geophone VSP corridor stack. Additionally, the decreased SNR for raw DAS data can be observed qualitatively by comparing the geophone and DAS corridor stacks.

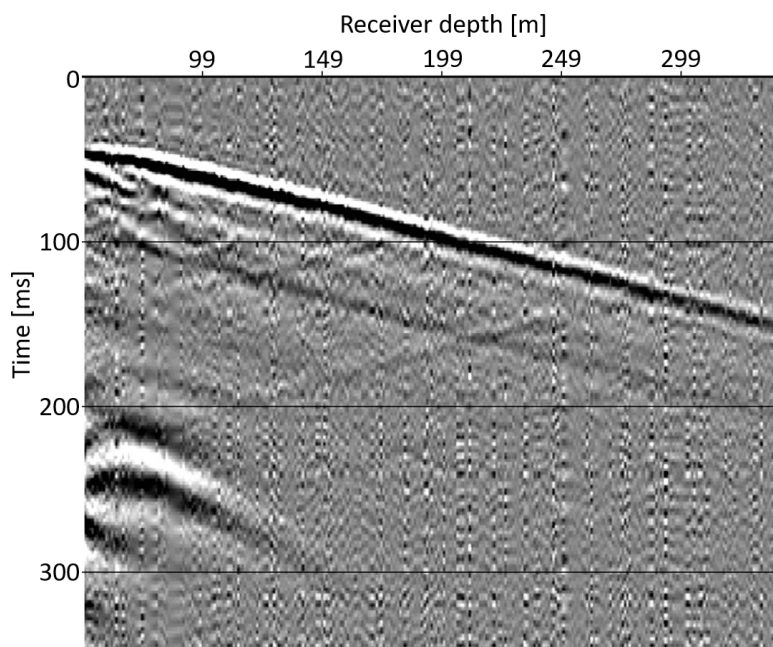


Figure 4-21: Interpolated straight fibre VSP, resampled to 1.0 m channel spacing intervals.

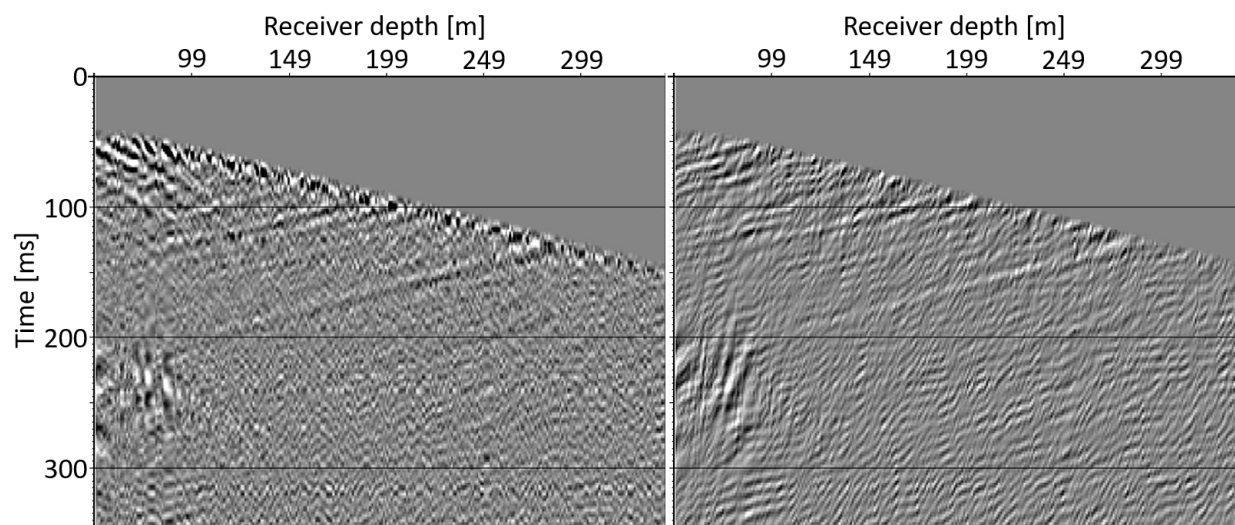


Figure 4-22: Straight fibre VSP upgoing wavefield before (left) and after (right) VSP deconvolution with downgoing wavefield and F-K filter to remove residual downgoing energy.

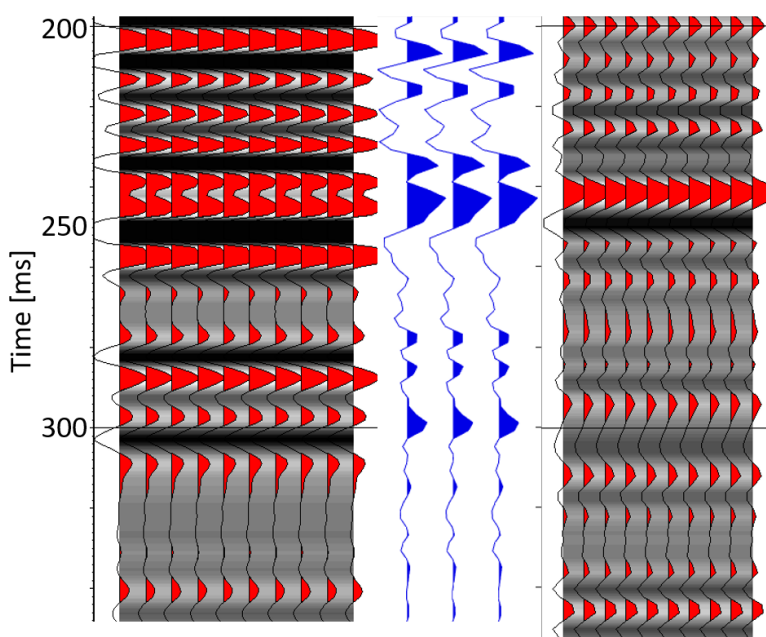


Figure 4-23: Comparison of geophone corridor stack (left), synthetic seismogram (centre), and straight fibre corridor stack (right).

The processing flow was then repeated for the same shot point for data acquired with straight fibre in the geochemistry well (Figure 4-24), an offset of approximately 109 m. The estimated SNR for the DAS data in the geochemistry well was calculated to be roughly 1.7, considerably lower than in the geophysics well. This could either be due to configuration of the fibre in the well, or because of the decay of signal amplitudes with increased offset. The resultant corridor stack from the geochemistry well (Figure 4-25) exhibits the same character as the stack from the geophysics well, but with lower signal amplitudes, likely deriving from the lower estimated SNR. Reflectors are slightly delayed in time, which is expected with increased offset.

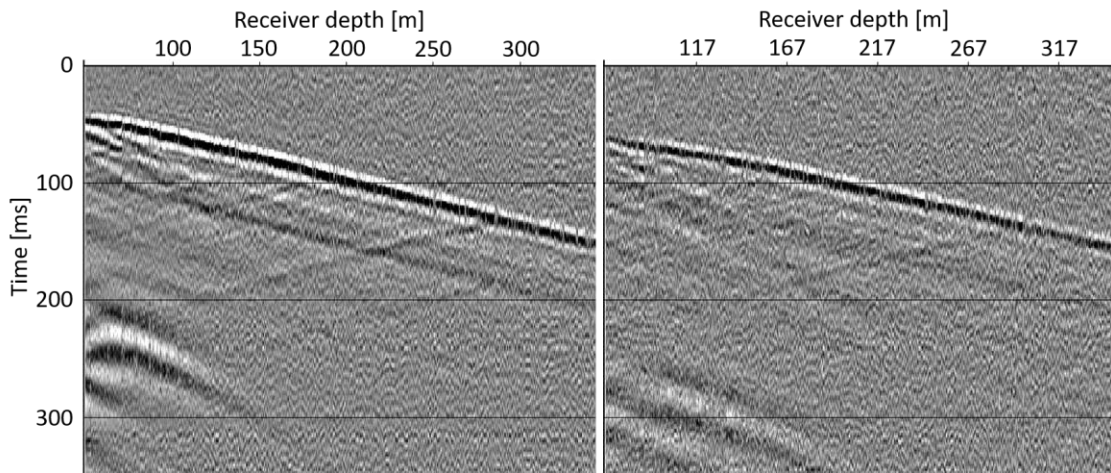


Figure 4-24: Straight fibre data from geophysics well (left) and geochemistry well (right). Decreased reflector amplitudes are observed on geochemistry well fibre. AGC applied.

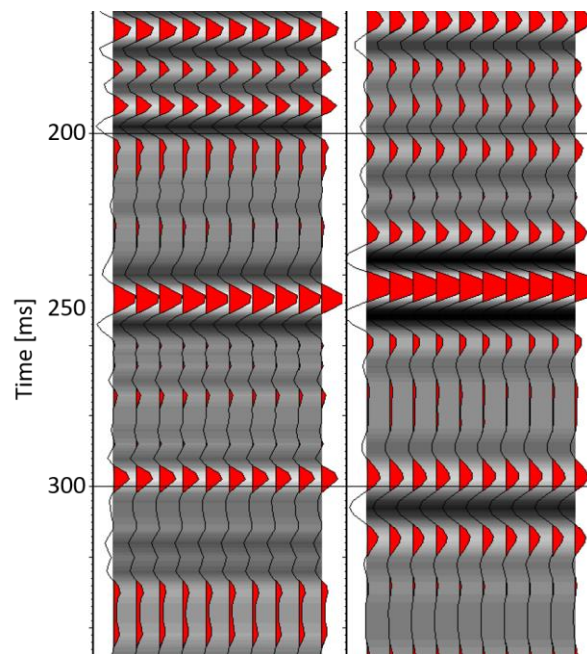


Figure 4-25: Comparison of straight fibre corridor stacks from geochemistry well (left) and geophysics well (right). Similar character observed, with lower amplitude reflectors and slight time delay for the geochemistry well corridor stack.

4.4 Implications for Permanent Sources

In an ideal scenario, time-lapse seismic data will have short time intervals between surveys, be densely sampled in the spatial domain, and have a high SNR. The use of permanent sources

will theoretically allow for rapid acquisition, while the deployment of DAS fibre allows for more dense spatial sampling of seismic data. The DAS examples in this chapter have a channel spacing which represents an increase in the number of channels per metre of nearly 20 times compared to geophone data. However, the goal of achieving high SNR data has not yet been addressed. It is anticipated that the use of permanent linear vibrators may help push the SNR of acquired data higher.

In July 2017, seismic data were acquired using the fibre loop as the receiver and a source line oriented north to south, centred on the geophysics well, and using the same sweep parameters as the May acquisition program. The maximum vertical fold of this source line was 10 (Figure 4-26), which should result in a higher SNR. A source point with an offset of 49 m from the geophysics well, station 21136, was selected to compare against the DAS VSP previously discussed, in order to investigate the effect of source effort (i.e. fold) on SNR.

The same method used previously to estimate SNR on DAS data was repeated for the data with increased source effort. While previous datasets required smoothing of first break picks to assist the picking algorithm, the initial result for this dataset was sufficient, likely due to the prominence of reflectors on the section. First break picks before and after median filtering overlap and are nearly identical (Figure 4-27). The estimated SNR for this shot record is approximately 10.2, roughly four times higher than the 3-fold shot record. While differences in near surface conditions between May and July may contribute to differences in the acquired data, the higher SNR of the July dataset clearly demonstrates the effect of source effort on SNR.

Additionally, to attempt to mitigate any seasonal impacts on the SNR between the May and July surveys, the unstacked data from station 21136 were used to investigate how the SNR changed with the addition of more sweeps (Figure 4-28). Qualitatively, the improvement in SNR can be

readily observed, as background noise appears to be reduced on the 8-sweep stacked data as compared to the 1-sweep data. Additionally, the estimated median SNR also increased from roughly 2.08 to 2.21. Typical increase in the SNR follows a \sqrt{N} relationship, where N is the number of sweeps used. This behaviour is not observed for these data, potentially due to the rudimentary estimation method employed. More accurate results could potentially be obtained by using an F-K filter on the data to separate the signal and noise components. As permanent sources give the ability to use several sweeps and stack the result, theoretically, the use of these sources can potentially push the SNR of recorded data higher than that of conventional Vibroseis data.

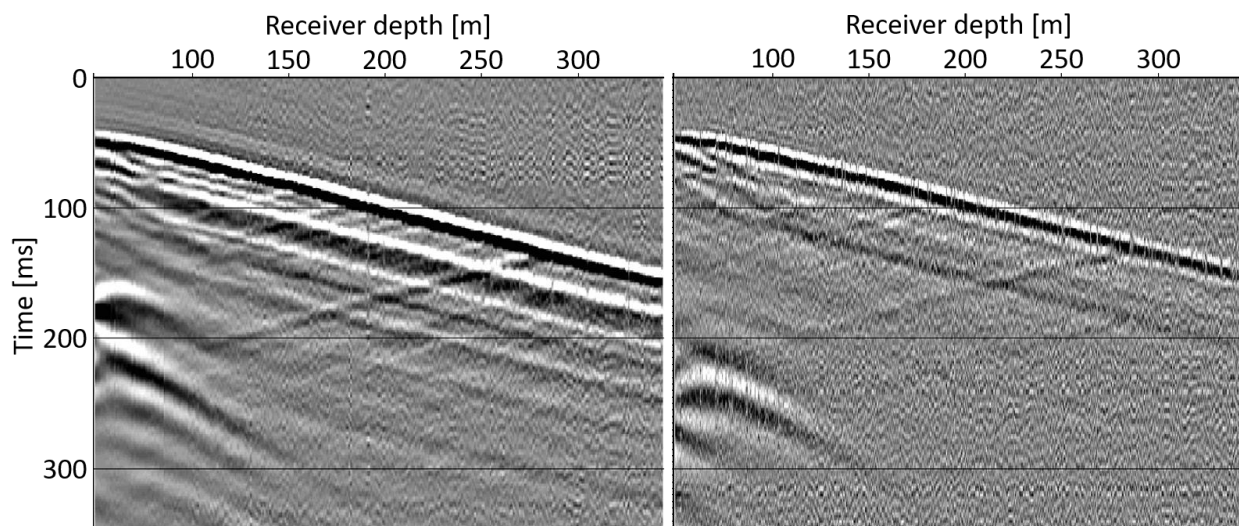


Figure 4-26: Comparison of 10-fold data (left) and 3-fold data (right) from straight fibre VSP in geophysics well.

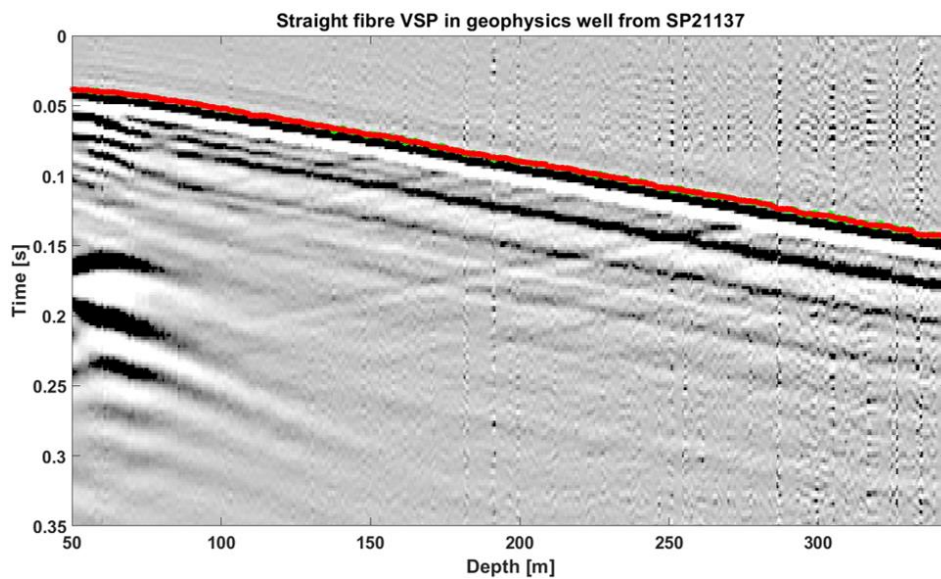


Figure 4-27: Straight fibre VSP in geophysics well with first break picks before median filter (green) and after median filter (red) overlain.

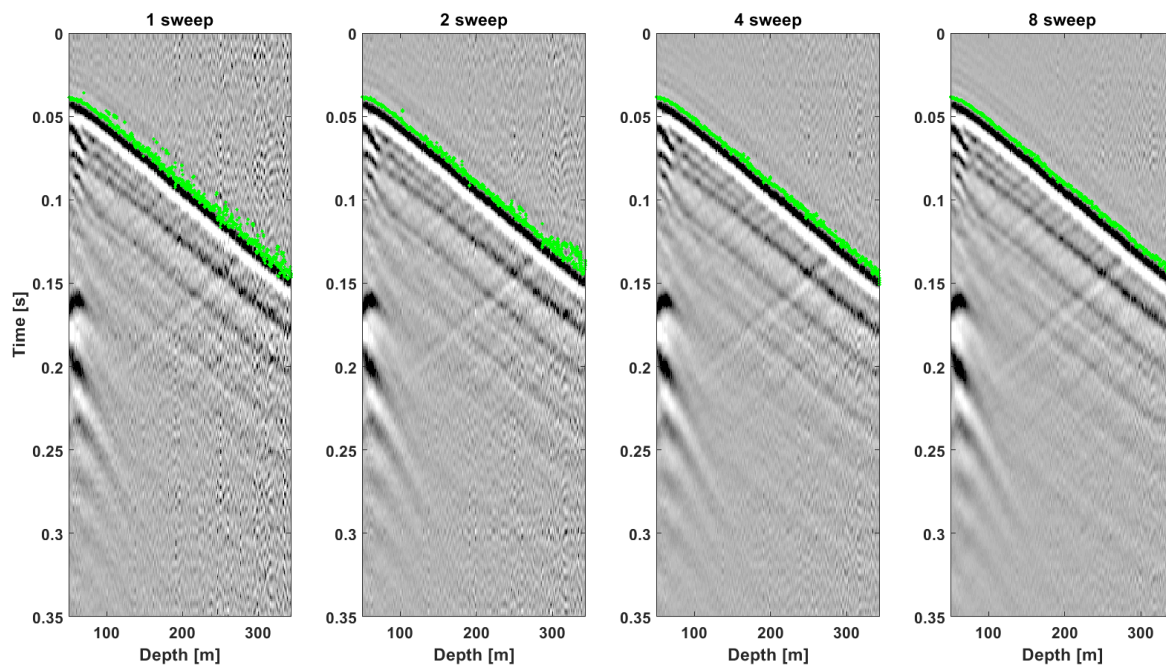


Figure 4-28: Straight fibre VSP in geophysics well with first break picks for 1, 2, 4, and 8-sweep data.

Chapter 5 – Results of Permanent Source Testing

5.1 Introduction

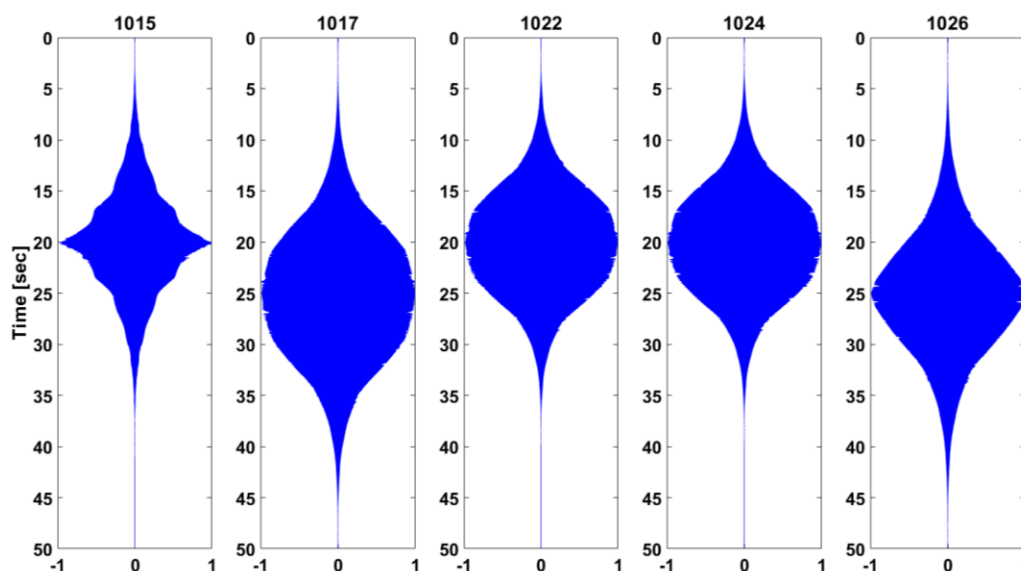
This chapter describes the initial testing of GPUSA linear vibrators at the CaMI FRS in 2018. Datasets were acquired using both the borehole linear vibrator, as well as the large surface linear vibrator. As described in Chapter 2, the borehole linear vibrator was cemented in a borehole at approximately 15 m depth, while the surface linear vibrator was mounted on a steel helical pile. The helical pile was anchored to a consolidated argillaceous layer at approximately 15 m depth. From Chapter 3, the sources were installed at approximately 110 m offset from the geochemistry well, along an azimuth passing through both the geochemistry and injection wells. This chapter will not only discuss the acquisition of permanent source data, but also some of the unique preliminary data processing steps applied to the data.

5.2 Borehole Linear Vibrator

In September 2018, the borehole linear vibrator was tested with various sweep parameters (Table 5-1). The vibrator tests were recorded with 24 3C geophones in the geophysics well, at an offset of approximately 58 m, and a short spread of 24 1C geophones centred on the source location. None of the five sweeps tested held the vibrator at its the maximum frequency. In other words, after reaching the maximum frequency, the downsweep started immediately. Sweeps 1022 and 1024 were run with identical parameters. Unfortunately, the accelerometer mounted in the source failed, thus the true source signature transmitted to the subsurface is unknown. The geophone placed next to the borehole at the surface, Station 36, was used to approximate the source signature for each sweep (Figure 5-1).

Table 5-1: Sweep parameters for borehole linear vibrator tests, September 2018

Sweep number	Maximum frequency (Hz)	Upsweep/downsweep time (s)
1015	125	20
1017	200	25
1022	200	20
1024	200	20
1026	175	25

**Figure 5-1: Traces from surface geophone nearest borehole linear vibrator (Station 36) for the five test sweeps.**

As described in Chapter 2, it is anticipated that the recorded amplitude of an orbital vibrator will have a quadratic relationship with the angular frequency. The amplitude spectra for the pilot traces for each of the five sweeps (Figure 5-2) show generally a quadratic increase in amplitude up to the maximum frequency for each sweep, followed by an abrupt decrease in amplitude to

zero. It is this sharp truncation in the amplitude spectrum that may be the source of ringy character observed in the synthetic data (Figure 3-12). The sharp truncation can be thought of as the result of filtering the spectrum with a boxcar, thus the ringiness in the time-domain data can potentially be explained by the Gibbs Phenomenon. The Gibbs Phenomenon refers to the ringing of the Fourier approximation of a signal at jump discontinuities (Weisstein, n.d.). The roll-off in amplitude towards the maximum frequency is thought to be due to the anti-alias filter in the Geode recording system used for acquisition. Aliasing refers to the inadequate sampling of a signal, and in seismic acquisition, causes the signal to be recorded at apparently lower frequencies (Lines & Newrick, 2004). The maximum frequency in the data that can be sampled without aliasing is called the Nyquist frequency (Margrave, 2013). The anti-alias filter is applied to the recorded data to filter out frequencies above the Nyquist frequency, roughly 500 Hz for the borehole vibrator tests. Typical anti-alias filters have a spectrum that begins to roll off at approximately 50% of the Nyquist frequency (Margrave, 2013); however, it appears that the anti-alias filter was more aggressive in this experiment, beginning roll off at approximately 170-180 Hz.

The average amplitude spectra for the full surface spread of geophones (Figure 5-3) is nearly identical to those of the corresponding pilot trace, exhibiting very similar changes in amplitude as frequency increases, as well as a sharp drop to nearly zero amplitude upon reaching the maximum frequency of the sweep.

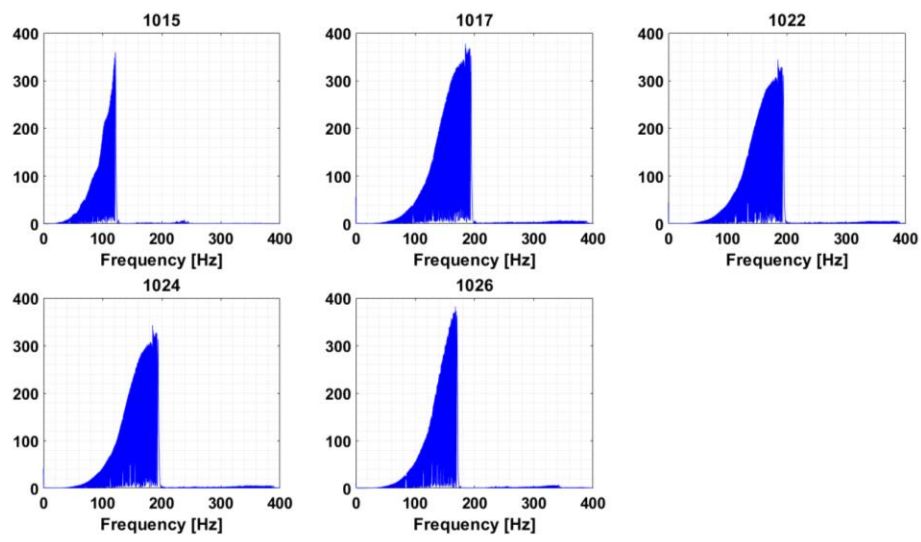


Figure 5-2: Amplitude spectra of pilot traces for the five borehole linear vibrator test sweeps.

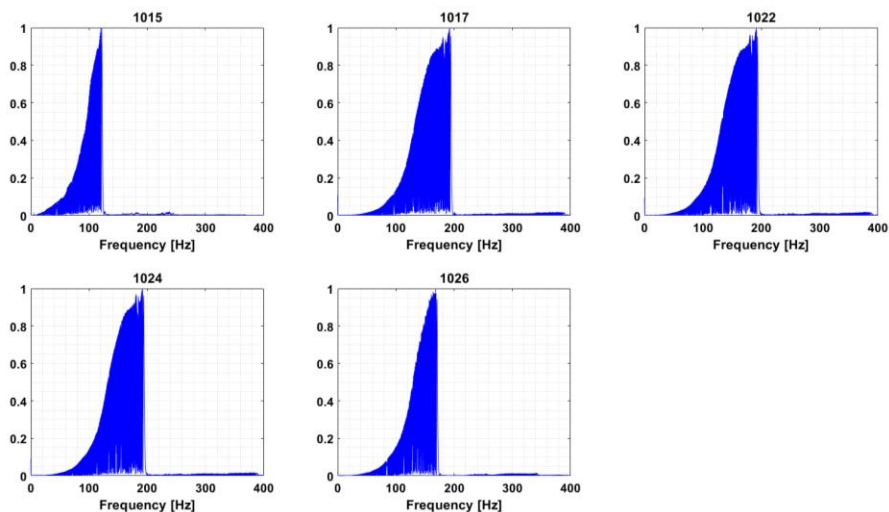


Figure 5-3: Amplitude spectra of surface 2D spread of geophones for each of the five borehole linear vibrator test sweeps.

Isolating and fitting a quadratic curve to the envelope of the amplitude spectrum confirms the dependence of amplitude on the angular frequency. A quadratic model was fit to the envelope of the portion of the amplitude spectrum less than the maximum sweep frequency (Figure 5-4).

The quadratic models fit to the amplitude spectra exhibited extremely high R^2 values, thus confirming the relationship between the observed amplitude and frequency (Table 5-2).

Table 5-2: Results of fitting quadratic models to pilot trace amplitude spectra of borehole linear vibrator tests

Sweep number	R^2
1015	0.9130
1017	0.9350
1022	0.9353
1024	0.9361
1026	0.8939

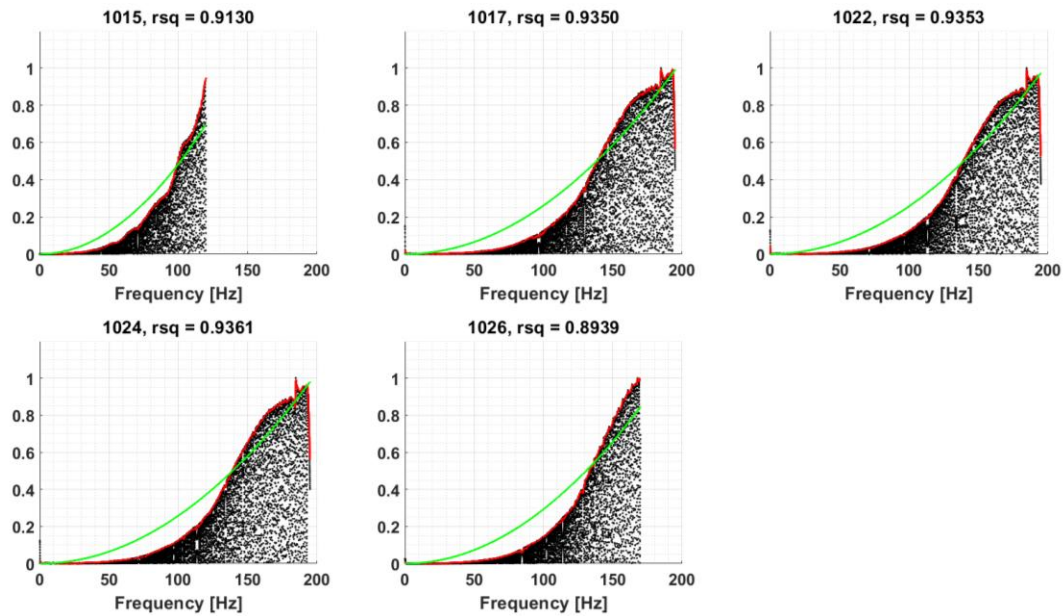


Figure 5-4: Results of fitting quadratic models (green) to the envelope (red) of the amplitude spectra (black) of each borehole linear vibrator pilot trace.

Computing the Gabor transform of the pilot traces and plotting the resultant time-frequency relationship yields promising results (Figure 5-5). The time-frequency spectrum for each sweep accurately reflects the sweep parameters listed in Table 5-1, with no visible energy outside of the dominant band. This implies that the sweep signature supplied to the borehole linear vibrator is efficiently transferred to the subsurface, with little noticeable impact from the cement, borehole casing, or other sources of noise. The Gabor spectrum plots of the uncorrelated surface spread for each sweep (Figure 5-6) show a similar character to that of the plots for the pilot traces; however, some noise has also been recorded. On each of the five displays, a high amplitude band is observed at all times at approximately 180 Hz. This is thought to be a 60 Hz harmonic. The dominant band of the Gabor spectrum can be revealed by normalizing the response of each frequency component (Figure 5-7). Although the plots are quite noisy, particularly at high frequency and for the 60 and 180 Hz harmonics, they do show that the source signature is being captured by the surface geophones.

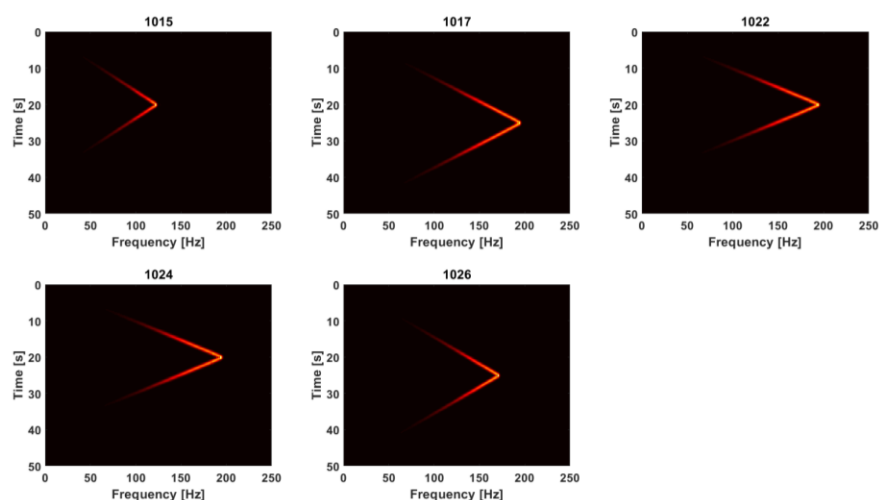


Figure 5-5: Time-frequency spectra of the pilot traces for each of the five borehole linear vibrator test sweeps.

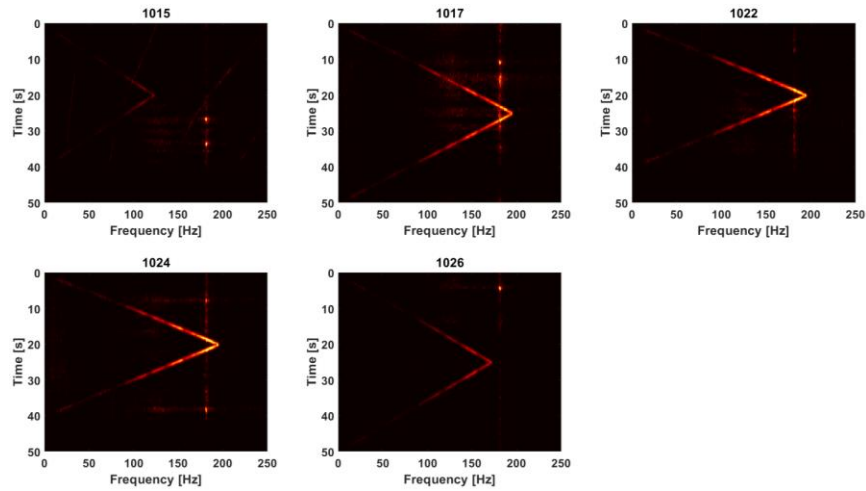


Figure 5-6: Time-frequency spectra of the surface 2D spread of geophones for each of the five borehole linear vibrator test sweeps.

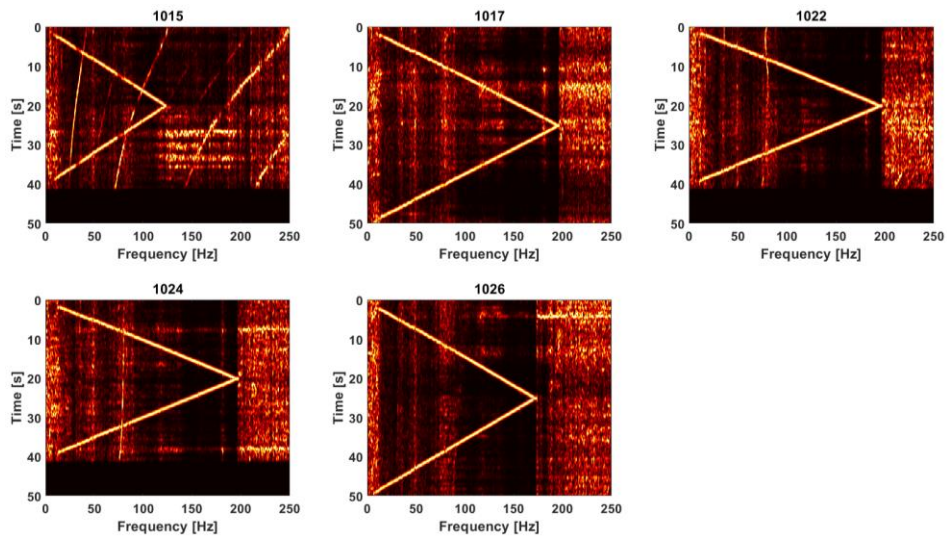


Figure 5-7: Time-frequency spectra of the surface 2D spread of geophones for each of the five test sweeps. Each frequency component of the spectra has been normalized.

5.3 Processing Considerations

Due to the unique acquisition features of deploying orbital vibrators, conventional data processing algorithms have to be modified to handle permanent source data. Unique processing considerations to create recognizable and usable datasets, such as modifications to correlation and

deconvolution workflows, will be developed based on data acquired during the initial testing of the borehole linear vibrator.

5.3.1 Correlation

During typical Vibroseis acquisition, an accelerometer is used to monitor the true motion of the baseplate. The accelerometer recording is then cross-correlated with recorded data in order to remove the overprint of the sweep in the data. Additionally, the length of the correlated record will decrease to be the difference between the length of the sweep and the total listen time of the record. Similarly, permanent seismic source should ideally have an accelerometer mounted on the source to record the ground motion. Unfortunately, the accelerometer failed during testing, and, being cemented in a borehole, is unable to be repaired. To create correlated shot records, two different methods were tested:

1. Correlate with the geophone closest to the source location (i.e. a pilot trace); and,
2. Correlate with a synthetic sweep generated from the known sweep parameters.

Using the sweep parameters from Table 5-1, synthetic sweep signatures were generated for each of the five borehole linear vibrator test sweeps. The synthetic sweeps were scaled with a quadratic amplitude modifier to satisfy the ω^2 relationship outlined in Chapter 2, as well as a cosine taper, similar to that used for Vibroseis sweeps (Figure 5-8). While not an exact match, applying both a cosine taper and ω^2 quadratic scaling to a linear sweep creates a trace that closely resembles the raw pilot trace. Theoretically, the surface casing of the source borehole could be used to better understand the source signature, as the coupling between the vibrator and the casing may cause the source signature to propagate directly to the surface through the casing, where it may be recorded. This has not yet been tested to mitigate the failure of the borehole source accelerometer.

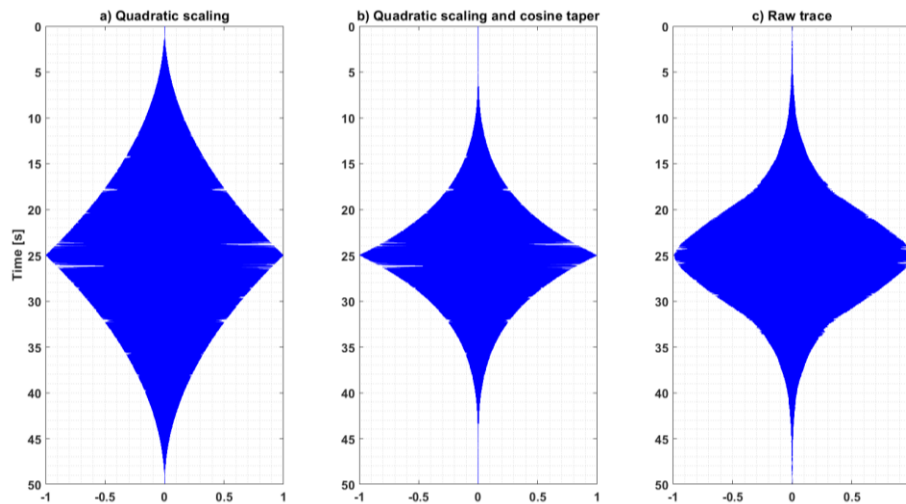


Figure 5-8: Traces used for correlation tests. All traces have a 0-175-0 Hz over 50 s time-frequency relationship. a) Linear sweep with ω^2 quadratic scaling; b) Linear sweep with cosine taper and ω^2 quadratic scaling; c) Pilot trace from sweep 1026.

Two of the three traces shown, the quadratic-scaled trace and the pilot trace, were also used to correlate the raw data, and the best sections were used for further analysis. In the ideal case where the sweep signature transferred to the ground is known exactly, the autocorrelation of this sweep signature will collapse to a signal known as a Klauder wavelet. Therefore, if the synthetic sweep created is truly representative of the sweep signature, then the autocorrelation of this synthetic sweep should be similar to that of the pilot trace. Additionally, the cross-correlation of the synthetic sweep and the pilot trace should also be a Klauder wavelet, with its maximum value at zero lag. However, computing this cross-correlation (Figure 5-9) indicates that this is not the case. Moreover, correlating both the quadratic-scaled synthetic sweep and the pilot trace with the raw borehole geophone VSP data yields significantly different results (Figures 5-10 and 5-11).

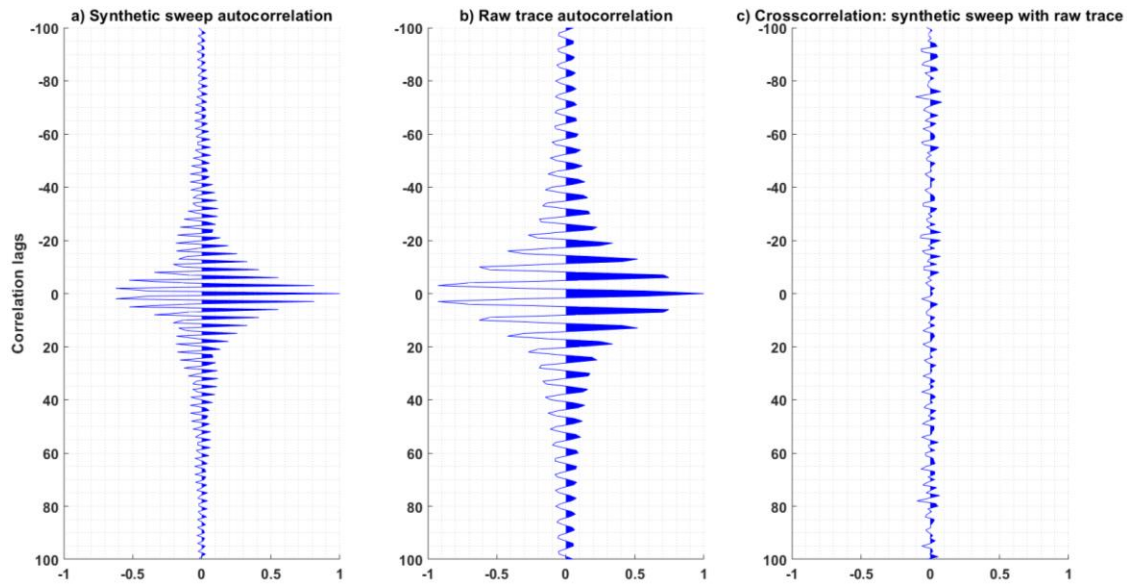


Figure 5-9: Cross-correlation results for quadratic-scaled synthetic sweep and pilot trace. a) Synthetic sweep autocorrelation; b) Pilot trace autocorrelation; c) Cross-correlation between synthetic sweep and pilot trace.

Comparing the two correlated datasets, it is evident that correlating the raw VSP data with the synthetic sweep does not produce reliable results. Correlating with the pilot trace from surface station 36 produces an image with easily identifiable first break energy and is more representative of expected VSP data. If the synthetic sweep could be altered to more closely match the pilot trace, or the borehole vibrator accelerometer could somehow be repaired, more accurate correlated sections could be produced.

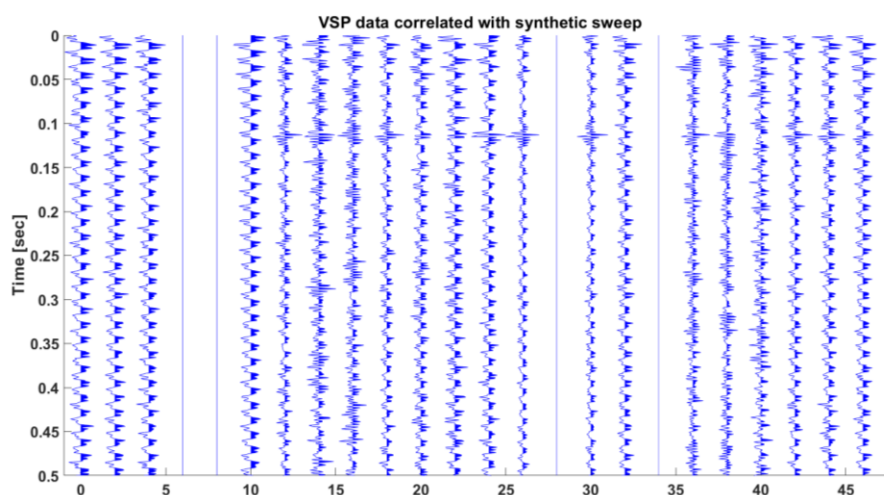


Figure 5-10: Borehole geophone data correlated with quadratic-scaled synthetic sweep.

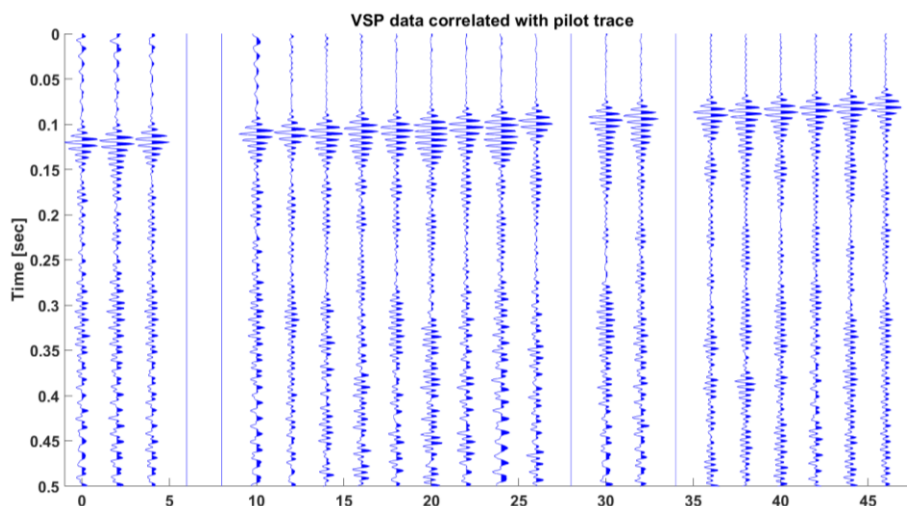


Figure 5-11: Borehole geophone data correlated with pilot trace.

5.3.2 Deconvolution

An example of recorded VSP data, using the vertical component from geophones in the geophysics well, as well as the surface spread of 1C geophones at 10 m intervals is shown in Figure 5-12. While the section displays a strong “ringy” character, the upgoing and downgoing wavefields are recognizable in the borehole geophone data (Figure 5-13). The ringy character observed in the correlated data is likely due to the quadratic amplitude characteristics of the source; i.e. the

ringiness is likely caused by the dependence of the source amplitude on ω^2 . The autocorrelation of the pilot trace is quite ringy, and this character is propagated into the correlated section.

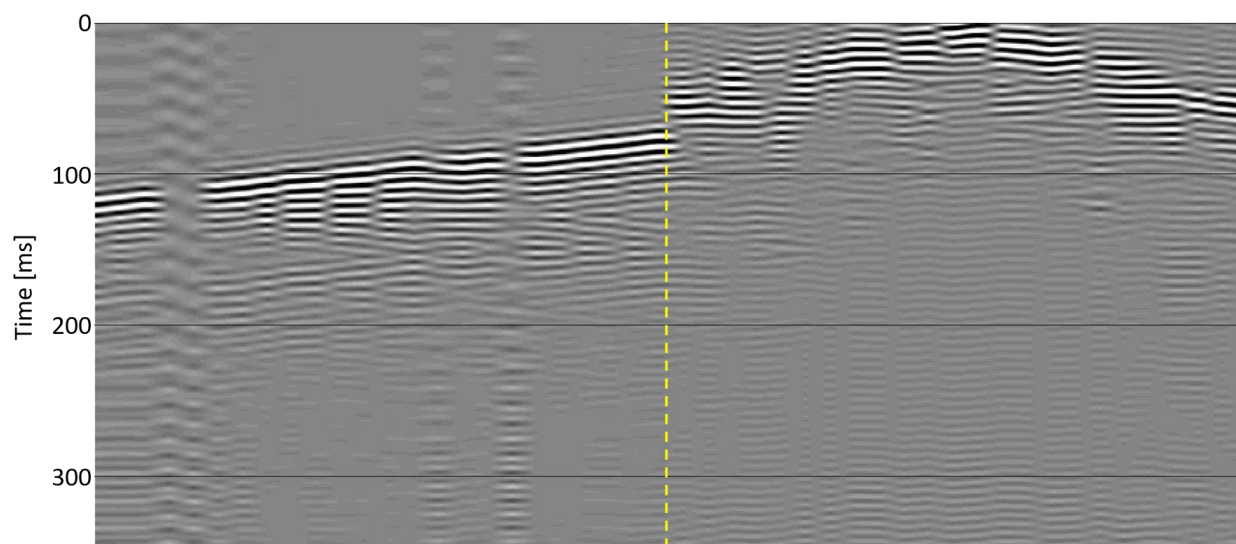


Figure 5-12: Vertical component of borehole geophones (left) and surface 1C geophones (right). Data correlated with surface pilot trace.

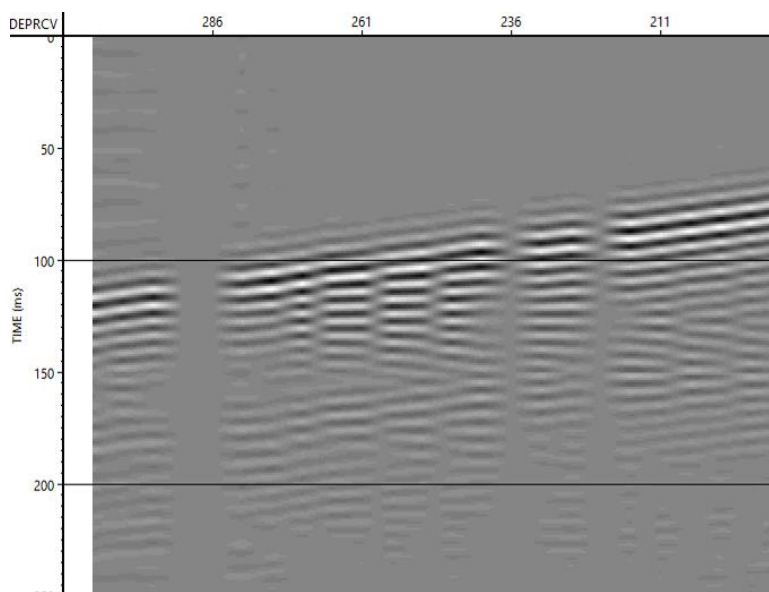


Figure 5-13: Vertical component of borehole geophone data, correlated with surface pilot trace. Dead traces have been muted.

To attempt to mitigate the ringy character of the correlated data, various deconvolution algorithms were tested, then applied to the VSP data. The pilot trace that was used for correlation

was subjected to the following algorithms: Wiener deconvolution, Gabor deconvolution, and deterministic deconvolution, using both the pilot trace and the idealized synthetic sweep (Figure 5-14). The deterministic deconvolution algorithm tested attempts to equate to the frequency domain source-signature deconvolution method used by Freifeld et al. (2016) in their work with SOV data at the Otway Project in Australia.

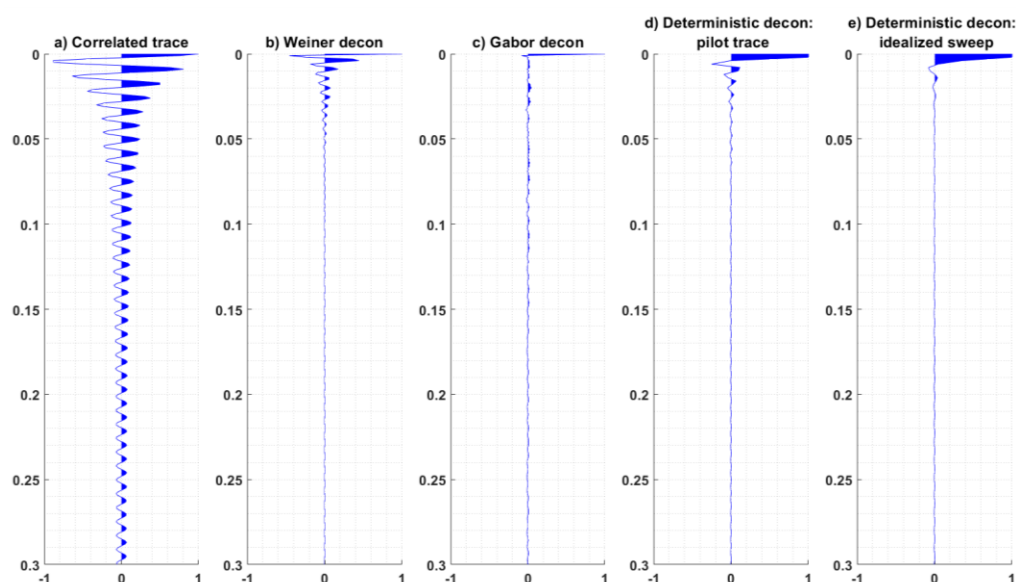


Figure 5-14: Deconvolution algorithm tests applied to correlated pilot trace. Traces displayed: a) Correlated pilot trace; b) Wiener deconvolution; c) Gabor deconvolution; d) deterministic deconvolution with the pilot trace; e) Deterministic deconvolution with the synthetic sweep.

Theoretically, the correlated pilot trace, used as a proxy for the source signature, should collapse to a delta spike function, with maximum amplitude at $t = 0$, after deconvolution. Deterministic deconvolution, whereby the spectrum of the input trace is multiplied by the inverse of the source spectrum, performs quite well when using both the pilot trace and the synthetic sweep to design the inverse operator. In both cases, low amplitude side lobes are observed, which may result in a residual ringy character in deconvolved data. Additionally, the high amplitude spike at

zero lag is quite broad for each of the deterministic deconvolution cases. Deterministic deconvolution with a synthetic sweep may have outperformed the same method using the pilot trace, as, in spite of the broader spike at zero lag, almost no ringy character is observed in the trace.

The Wiener and Gabor deconvolution methods both appear to work well, with the resultant traces from each algorithm resembling a delta function. However, the Wiener deconvolution algorithm has high-frequency side lobes on the resultant trace, which are not observed on the Gabor trace. Computing the amplitude spectra of the deconvolved traces (Figure 5-15) appears to confirm the superiority of Gabor deconvolution. The spectrum of the original trace, as expected, displays a quasi-quadratic increase up to the maximum sweep frequency. In the ideal case, the spectrum should be white after deconvolution, as the spectrum should represent the reflectivity time series of the subsurface (Margrave, 2013). Gabor deconvolution appears to have outperformed Wiener deconvolution in terms of whitening the spectrum across all frequencies. Wiener deconvolution has boosted amplitudes at low frequency, which may be beneficial for overcoming the quadratic relationship between amplitude and frequency for orbital vibrators. Additionally, the Wiener deconvolution method has introduced a high-amplitude feature at high frequency, which may be explained by the side lobes observed on the deconvolved trace in the time domain.

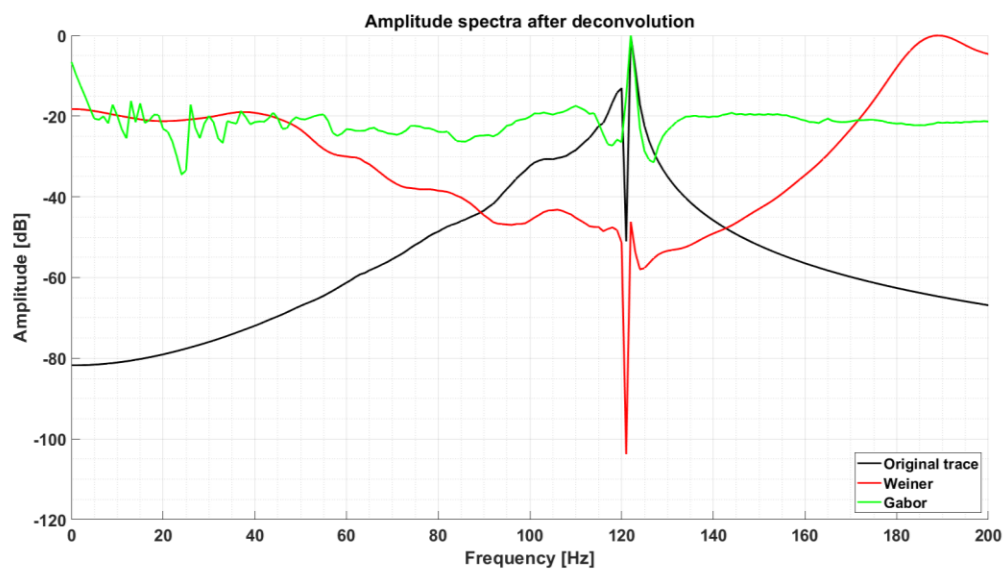


Figure 5-15: Amplitude spectra of correlated trace (black) and traces after Wiener (red) and Gabor (green) deconvolution applied.

Wiener and Gabor deconvolution were then applied to the VSP data after correlating with the pilot trace (Figure 5-16). The same parameters for each method that were applied to the pilot trace deconvolution tests were used; however, the Wiener deconvolution algorithm does not completely remove the ringy character of the shot record, particularly after the first breaks. The Gabor deconvolution algorithm appears to have removed more of the ringy character in the shot gather. Therefore, the focus for further data processing will be on the dataset with Gabor deconvolution applied to data correlated with the pilot trace.

Compared with data acquired with the same receiver geometry and source-receiver offset, the borehole linear vibrator data, after correlation and deconvolution, is similar to data acquired using a conventional linear Vibroseis sweep over approximately the same bandwidth (Figure 5-17). The VSP data processing flow developed for a Vibroseis source and borehole geophone receivers was applied to the deconvolved shot records from the borehole linear vibrator. The

resultant corridor stack from the linear vibrator data ties fairly well with the stack from the Vibroseis source and to a zero-offset synthetic seismogram (Figure 5-18). A slight time delay for major reflectors exists between the Vibroseis and borehole vibrator corridor stacks, which could be due to a different source static between the borehole source and surface Envirovibe source.

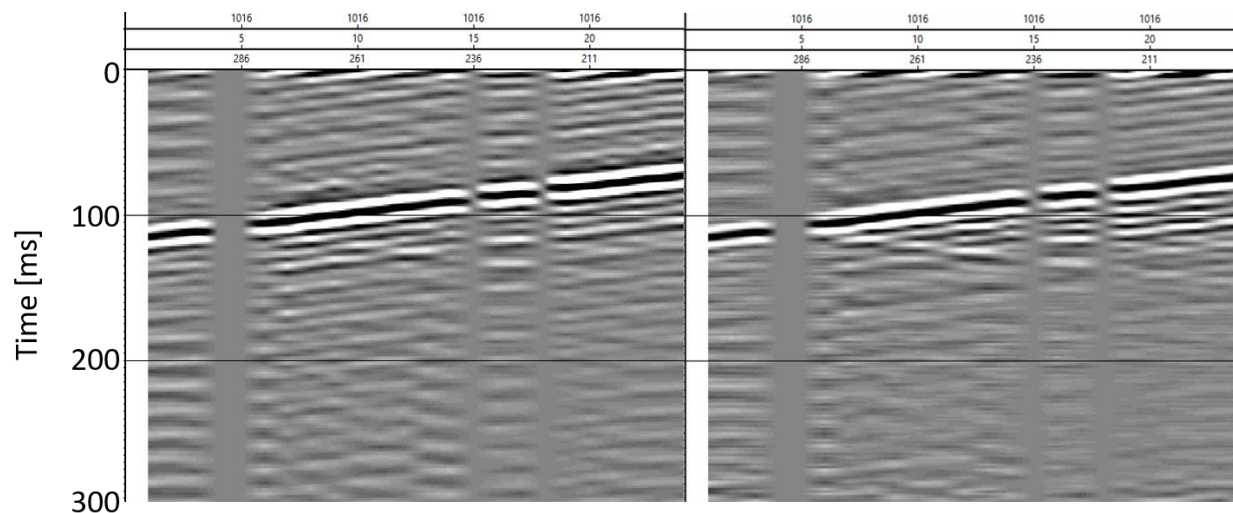


Figure 5-16: Borehole linear vibrator data with borehole geophone receivers, correlated with surface pilot trace. Wiener deconvolution (left) and Gabor deconvolution (right) applied to correlated data.

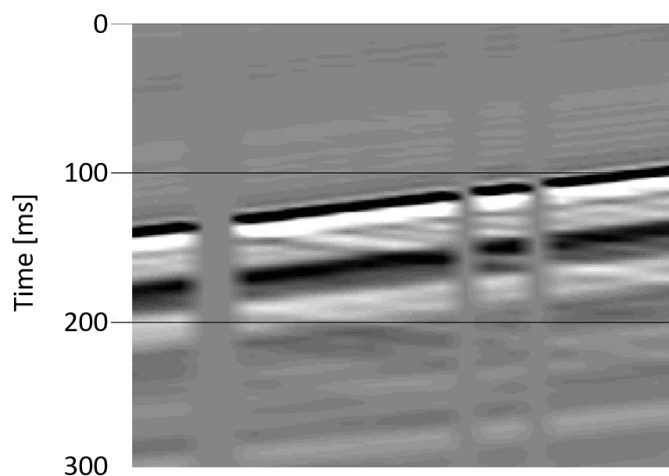


Figure 5-17: Envirovibe data recorded with borehole geophones at equivalent offset to borehole source. No deconvolution applied.

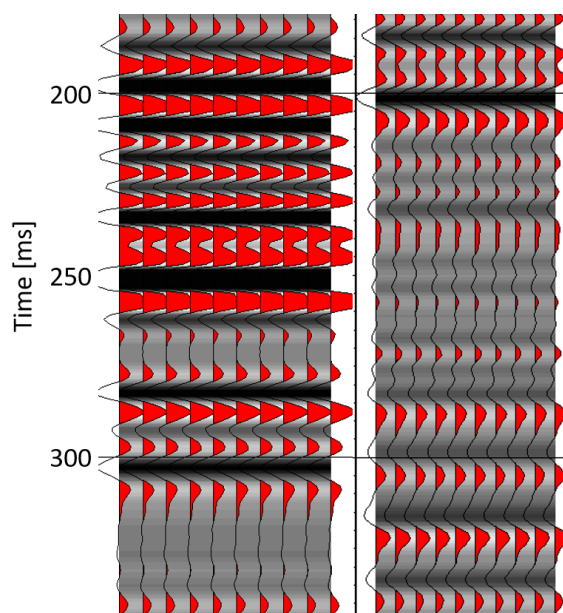


Figure 5-18: Corridor stack comparison between Vibroseis (left) and borehole linear vibrator (right) data.

5.3.3 Source effort

Increasing the source effort in seismic acquisition has shown to be beneficial in increasing the SNR. In November 2018, several borehole linear vibrator sweeps were run with the same parameters to investigate the effect of increasing the source effort for orbital vibrator sources. Ten sweeps were performed, all using a 0-150 Hz upswEEP over 20 s with a symmetric downswEEP and using the 3C geophones and a small 2D line of 1C geophones as the receivers. The line of 1C geophones had one end at the source location, rather than centred on the source as with previous tests.

Correlating the vertical component of the borehole geophone recordings with the surface pilot trace, strong horizontal noise bands are observed in Sweeps 7 and 9 (Figure 5-19). However, stacking these records with the shot records from other sweeps serves to greatly reduce this source of noise (Figure 5-20).

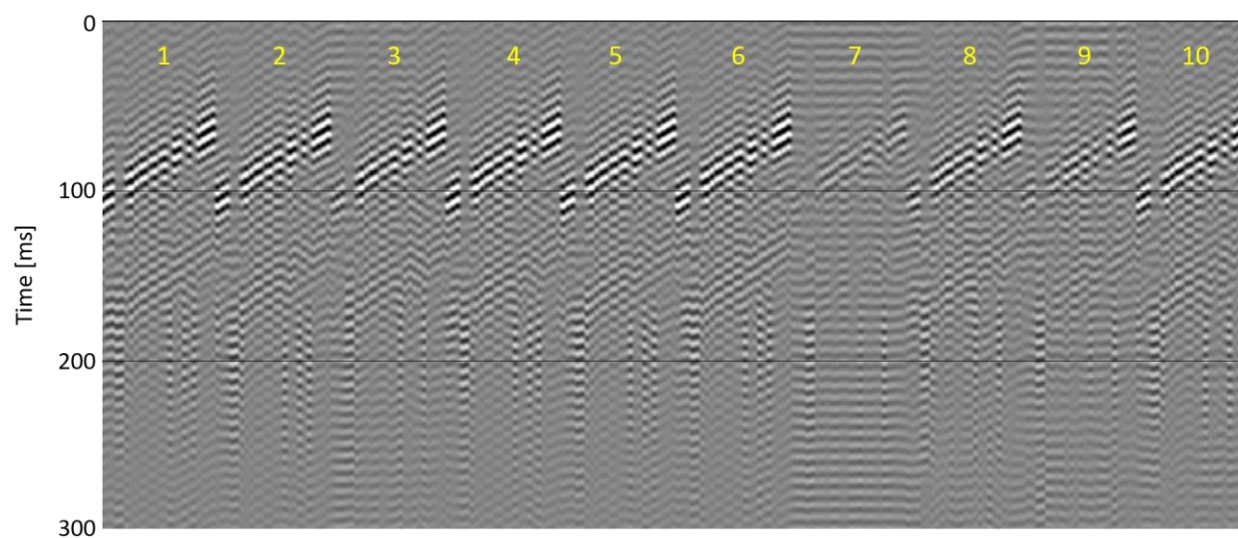


Figure 5-19: VSP data correlated with pilot traces from each sweep. Note the strong horizontal noise bands on Sweeps 7 and 9.

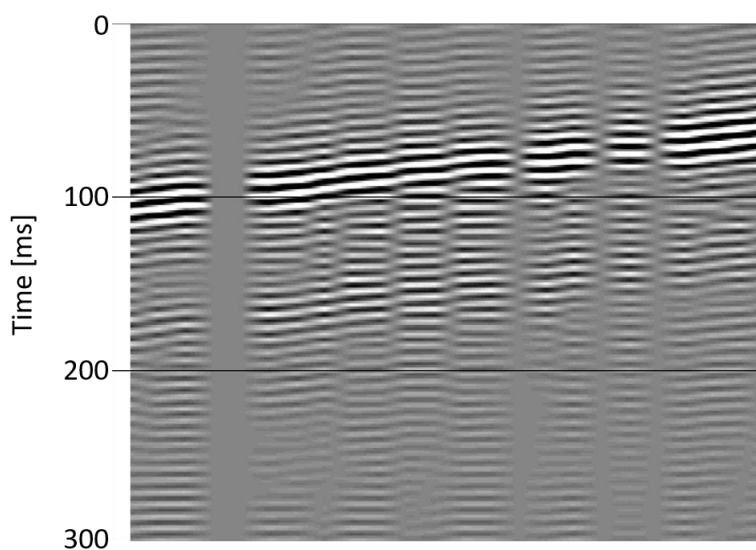


Figure 5-20: Stacked VSP gather from 10 borehole linear vibrator sweeps with same sweep parameters.

As described previously, three major processes must be applied to raw, uncorrelated data before it is able to be processed using previously developed workflows: correlation, deconvolution, and stacking. It is unclear in what order to apply these processes; however, from the study of using

a single sweep, described in the previous section, deconvolution should be applied after correlating raw data with the pilot trace. The three cases, where the stacking process is the first, second, or third step in the flow, were tested. Stacking before correlation and deconvolution drives the data close to what is expected, but still results in an unreliable dataset (Figure 5-21). The result is heavily contaminated by time-stationary noise, and the downgoing wavefield is barely visible through the noise. Additionally, the upgoing wavefield cannot be identified. In conventional Vibroseis acquisition and processing, raw records are stacked and then correlated with the sweep signature. However, it appears that the same workflow should not be applied to linear vibrator data. One potential reason for the failure of this workflow is that the true source signature is not exactly known, and correlation was carried out using a single pilot trace from an individual sweep. Small sweep-to-sweep variations may exist in the recorded pilot traces, thus, by correlating with a single pilot trace, errors may be introduced into the correlated record. With source accelerometer data, stacking before correlation could potentially be more viable, especially if the sweep signature remains effectively constant.

Stacking before deconvolution appears to have improved the resultant data (Figure 5-22). Shot records from individual sweeps were correlated with the associated pilot trace, then stacked. The horizontal noise bands observed in the previous case are greatly reduced, but the ringy character of the record still remains. The upgoing wavefield is partially visible, and the first breaks are more evident, but a ringy character is still pervasive in the data. In particular, the ringy character has obscured the exact first arrival events. Similar behaviour is observed on the dataset created by applying Gabor deconvolution to correlated records from each sweep, then stacking the results (Figure 5-23). The resultant shot record exhibits significant improvement compared to simply

stacking individual correlated records, illustrated by a more readily identified upgoing wavefield and the reduction in ringy character in the downgoing wavefield below the first breaks.

From prior analysis of borehole linear vibrator datasets, it has been demonstrated that correlating raw data with a surface pilot trace and applying Gabor deconvolution should produce optimum datasets. Additionally, analysis of Envirovibe datasets indicate that increasing the source effort should also increase the SNR. However, combining these concepts for borehole linear vibrator datasets has not proven successful. Gabor deconvolution has improved the individual correlated records by removing most of the ringy character, but the stacked record remains quite ringy. In the processing flow described by Freifeld et al. (2016), a correlation-based alignment process is applied to remove potential phase differences in datasets from different sweeps. The stacking process could therefore potentially be improved by more carefully aligning the data from each sweep prior to stacking.

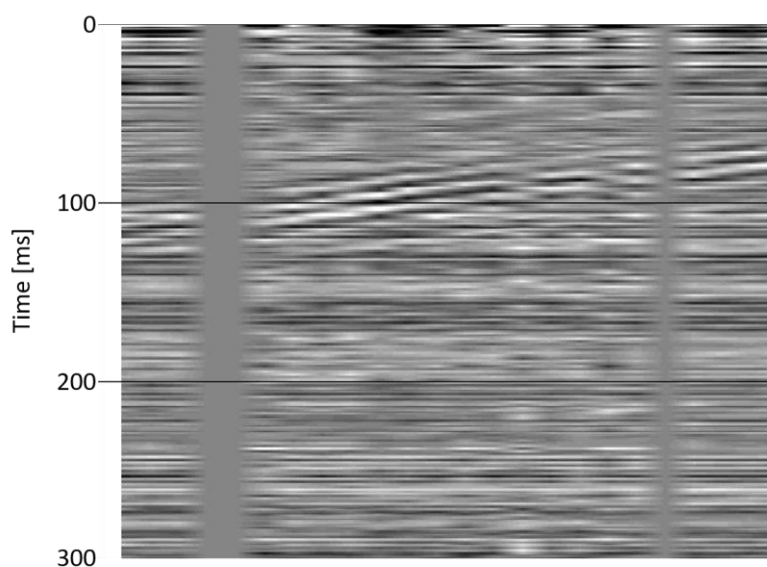


Figure 5-21: Data from ten borehole linear vibrator sweeps. Data were stacked, then correlated with a pilot trace, then Gabor deconvolution was applied.

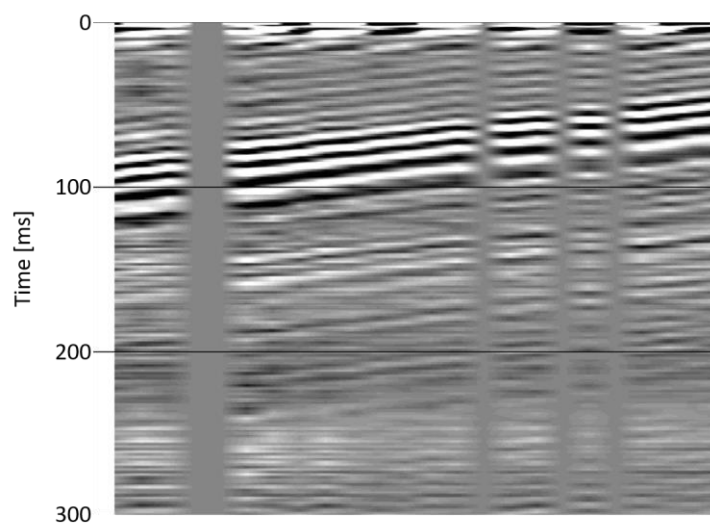


Figure 5-22: Data from ten borehole linear vibrator sweeps. Data were correlated with pilot traces from each sweep, then stacked, then Gabor deconvolution was applied.

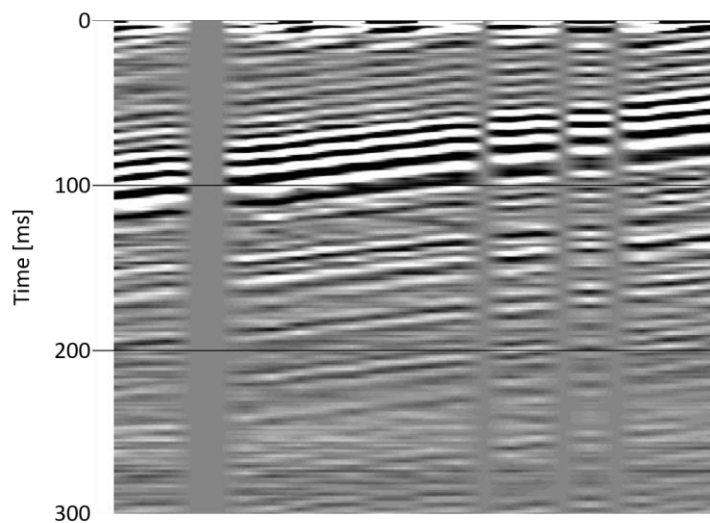


Figure 5-23: Data from ten borehole linear vibrator sweeps. Data were correlated with pilot traces from each sweep, then Gabor deconvolution was applied, and the deconvolved records were stacked.

5.4 Surface Linear Vibrator

In September 2018, the large surface linear vibrator was tested using a spread of 1C geophones on the surface, with 10 m receiver spacing along the trench at the FRS (Figure 5-24).

Six sweeps were tested, each with a 24 second sweep from 0-100 Hz (the upswing), and a 24 second decrease from 100-0 Hz. The first five records had a listen time of 2 s, resulting in a 50 s record. The last sweep tested had a 12 s listen time for a 60 s record, the maximum allowable in the SEG-Y file format. The triggering system to start recording and to start the source were not synchronised, thus a radio countdown system was used to trigger both the receiver and source systems. Therefore, a slight time lag may exist at the start of each record when comparing sweeps. Additionally, during acquisition with the surface spread of geophones, the onboard source accelerometer was not recorded. To approximate the source signature for each sweep, the geophone closest to the source location, Station 154, was used. Subsequent tests were run to record the signature of the source accelerometer.

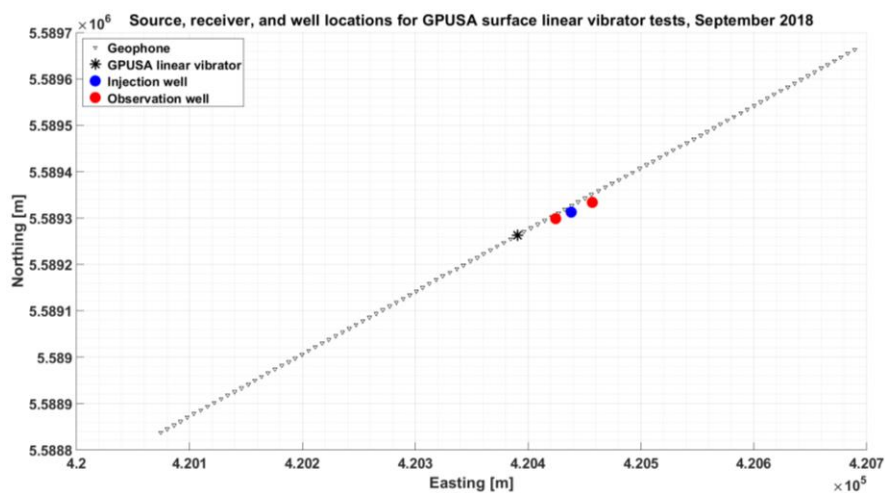


Figure 5-24: Source and receiver acquisition geometry for large surface linear vibrator testing.

Initial uncorrelated shot records do not display any useful information upon first glance when displayed in the $x-t$ domain. However, extracting selected traces for further analysis reveals unique characteristics of permanent seismic source data. Three traces were extracted from the

uncorrelated shot record (Figure 5-25): a near offset trace, closest to the source location (approximately 4.5 m offset), a mid-distance trace (approximately 270 m offset), and a far offset trace, located at the southwest end of the receiver line (approximately 530 m offset). The near offset trace, used to approximate the source signature, displays a quasi-quadratic increase in amplitude at either end of the non-zero portion of the trace, as expected based on the predicted quadratic relationship between amplitude and frequency for orbital vibrators. However, the trace appears asymmetric and quite “notchy,” with larger amplitude spikes prevalent throughout the trace. These notches could potentially mask the true quadratic increase in amplitude. The cause of these high amplitude notches is likely the helical pile upon which the source is mounted. Video recordings of the surface linear vibrator show the baseplate of the source vibrating erratically. These vibrations could potentially be explained by the fact that the helical pile is not a single piece of metal; rather it is comprised of segments that are bolted together, allowing the segments to move slightly in the subsurface. The cumulative effects of the interaction between moving segments may cause the low-frequency overprint observed on the near trace. Additionally, the video recordings show the portion of the pile above the surface vibrating, suggesting that instead of acting as a point source at the anchor point, the pile acts as a line source. To attempt to mitigate the effects of vibration between segments, a new steel pile was installed in February 2019. Rather than being bolted together, the segments of this new pile have a screw threading, allowing for stronger coupling between the segments. While the surface linear vibrator has not been tested with the new pile, it is anticipated that the erratic spectra observed in the data will be reduced.

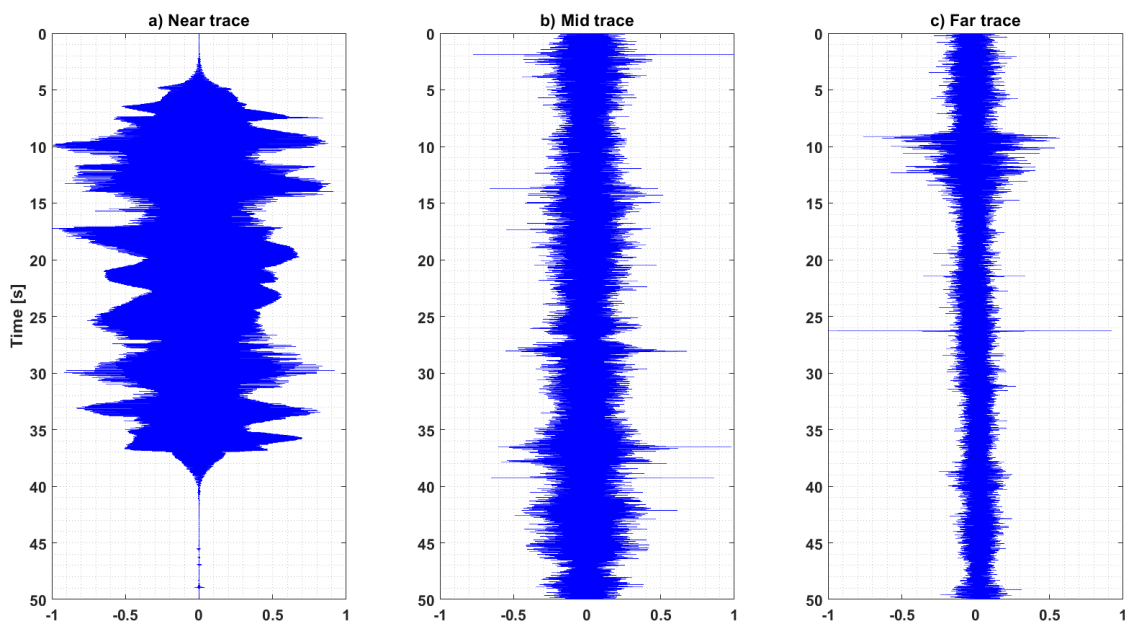


Figure 5-25: Near (a), mid (b), and far (c) offset uncorrelated traces from surface geophones for a test sweep of large surface linear vibrator.

While some meaningful information can be extracted from a time series plot of the uncorrelated near offset trace, the mid-offset and far offset traces appear to be dominated by noise. However, creating time-frequency plots (Figure 5-26) for each trace using the Gabor transform yields more information. The time-frequency plot of the near offset trace shows that it is a reasonable approximation of the source signature, as the dominant mode of the plot follows a 0-100-0 Hz pattern, the same as the sweep parameters input to the source. Several lower amplitude harmonics are also observed at frequencies above and below the fundamental mode. The time-frequency plot for the mid-offset trace shows a similar character, but at significantly lower amplitude. The plot is dominated by noise bands at approximately 90, 135, and 145 Hz. The far offset plot shows no evidence of similar behaviour to the near offset time-frequency plot and appears to be dominated by noise. This change in the character of the time-frequency plots from near to far offset could indicate that the source does not emit sufficient energy to transfer the source

signature to far offsets but is more likely due to attenuation and spherical divergence as the energy propagates to farther offsets.

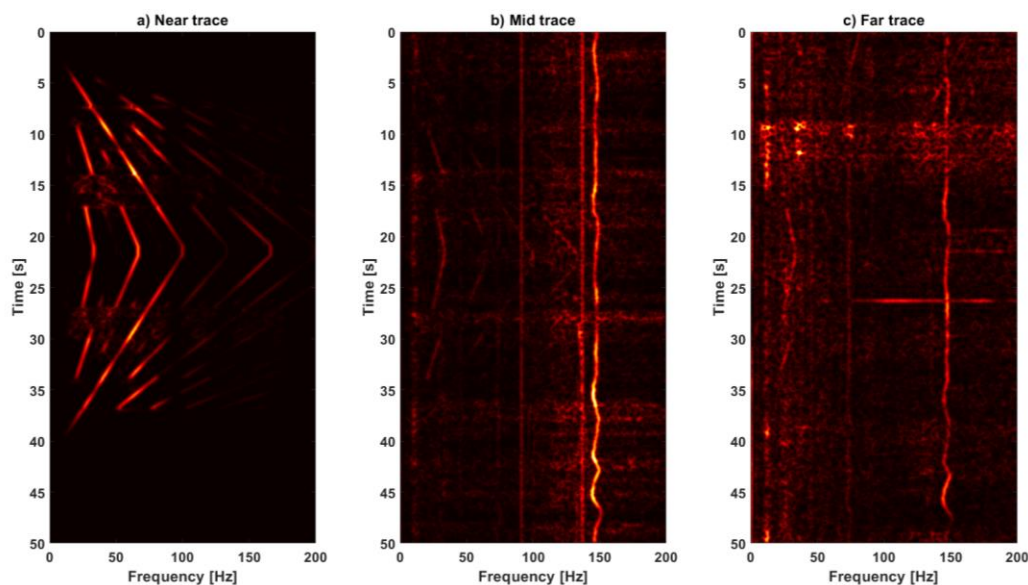


Figure 5-26: Time-frequency spectra for near (a), mid (b), and far (c) offset traces from surface geophones from a test sweep of large surface linear vibrator.

5.4.1 Source accelerometer measurements

During the acquisition of data with the large surface linear vibrator, the accelerometer mounted on the source was not always recording. Unlike the buried source, the accelerometer for the surface source was functional, and was tested immediately following the acquisition of 2D data using the surface spread of geophones. Twelve sweeps were run (Table 5-3; Figures 5-27, 5-28, and 5-29), each from 0-100 Hz with varying upswing times. Two sweeps, Sweep 5 and Sweep 6, tested a linear increase to the maximum frequency, at which point the source was shut off, and the rotating mass was allowed to come to rest naturally, and lasted roughly 30 s. Four sweeps also tested maintaining the vibrator frequency at the maximum frequency for an arbitrary amount of

time. The source accelerometer failed for two sweeps, thus the readings for these two sweeps will not be analysed further.

Table 5-3: Generalized sweep parameters for large surface linear vibrator source accelerometer tests.

Sweep number	Upsweep design	Approximate hold time at maximum frequency (s)	Downsweep design
1-4	Controlled, linear	0	Controlled, linear
5, 6	Controlled, linear	0	Uncontrolled
8, 9, 11, 12	Controlled, linear	10	Controlled, linear
7, 10	Failed	Failed	Failed

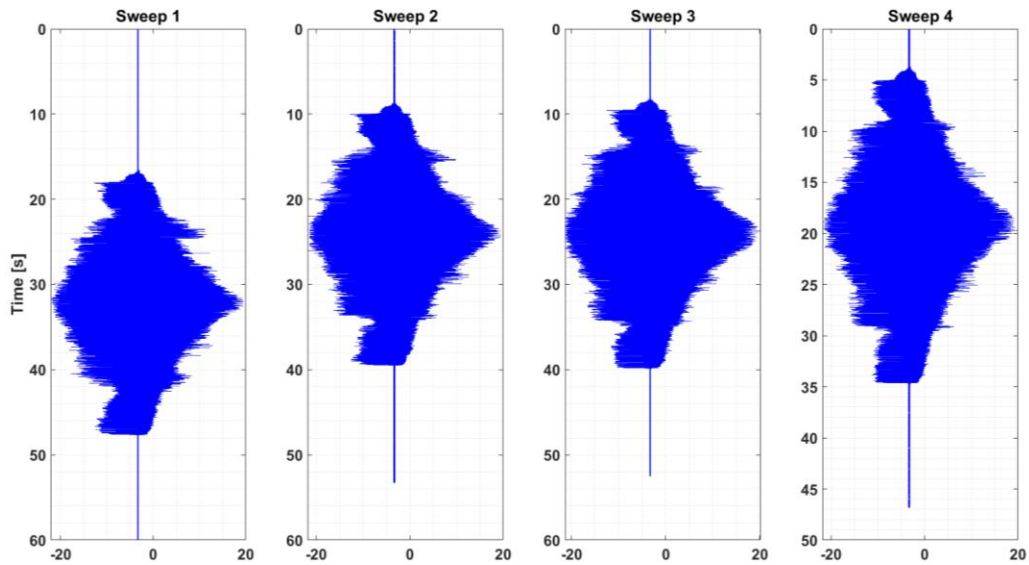


Figure 5-27: Sweeps 1-4 from large surface linear vibrator accelerometer tests.

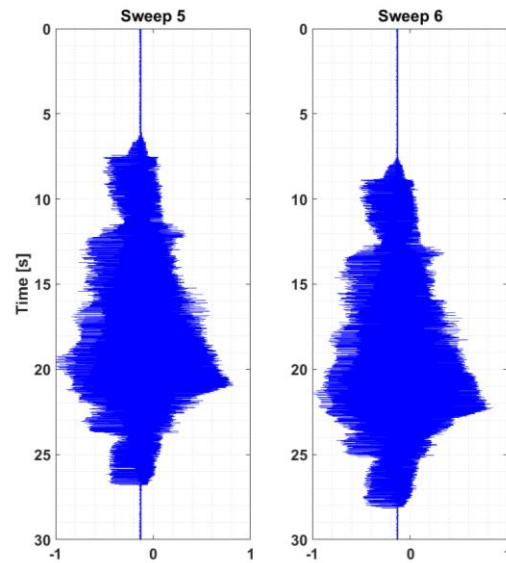


Figure 5-28: Sweeps 5 and 6 from large surface linear vibrator accelerometer tests.

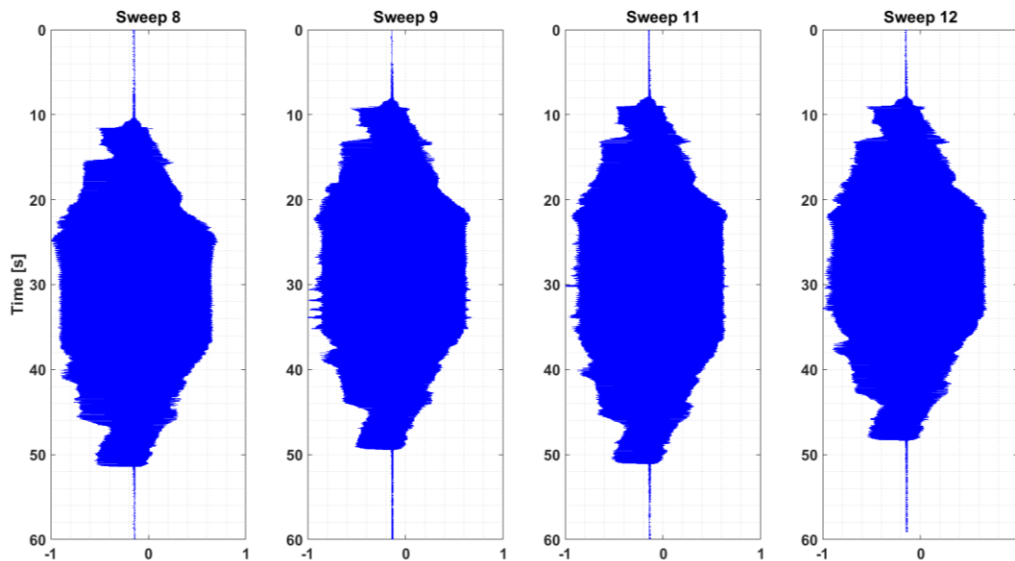


Figure 5-29: Sweeps 8, 9, 11, and 12 from large surface linear vibrator accelerometer tests.

The dominant bands of the time-frequency spectra for each of the 10 sweeps analysed accurately reflects the general sweep parameters listed in Table 5-3 (Figure 5-30). On each of the time-frequency plots, the highest amplitude band appears to be replicated at frequencies higher

and lower than the fundamental band, interpreted to be a type of harmonic recorded by the accelerometer.

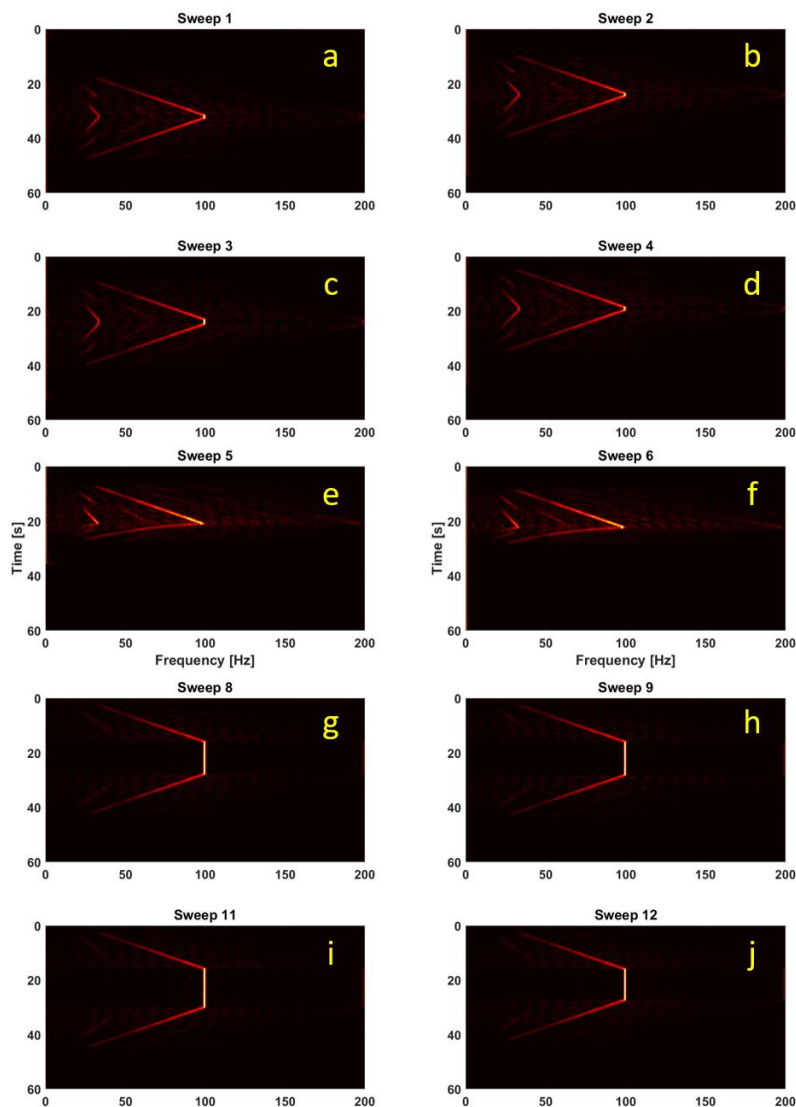


Figure 5-30: Time-frequency plots for ten large surface linear vibrator accelerometer test sweeps. Sweeps 1-4 (a-d) have a linear and symmetric upswep and downswep. Sweeps 5 and 6 (e and f) have a linear upswep and uncontrolled downswep. Sweeps 8, 9, 11, and 12 have a linear and symmetric upswep and downswep, and hold the vibrator frequency at maximum for approximately 10 s.

Comparing Sweep 1 with the uncorrelated pilot trace from the surface geophones (Figure 5-31), significant differences are observed. A time lag exists between the two traces as the

triggering mechanisms for the source and the recording systems were not synchronized. The accelerometer reading appears to increase in amplitude in a quasi-quadratic manner, reaching maximum amplitude approximately halfway through the sweep. This behaviour is expected as the upsweep and downsweep segments were intended to be symmetric. As described previously, the pilot trace is quite notchy, likely caused by erratic vibrations in the source baseplate or helical pile. The discrepancy between these two traces implies that the source accelerometer is not properly recording this high-amplitude vibration. This appears to be confirmed by considering the time-frequency spectra for these traces (Figure 5-32). The harmonics observed on the accelerometer time-frequency plot are of considerably lower amplitude than those on the pilot trace plot, leading to the conclusion that the impacts of the baseplate and pile are mitigated by recording with the source accelerometer. Additionally, that the harmonics are observed on both the accelerometer and pilot trace readings implies that the harmonics are likely not due to vibrations from the pile. If the harmonics were caused solely by the steel pile, the accelerometer would not record these harmonics as it is connected via the baseplate to the pile. While not easily observed on video recordings, vibration of the ground surface surrounding the pile occurs at discrete frequencies, implying that the harmonics observed could be a response of the near surface to the pile harmonics. The fundamental harmonic frequency of a 15 m steel pile, assuming a P-wave velocity of 5000 m/s in steel and the pile is fixed at one end (i.e. the anchor point in the subsurface), is computed to be approximately 83 Hz, and the third harmonic is computed to be 250 Hz. The mass of the source on top of the pile may serve to decrease these harmonic frequencies, thus possibly explaining the high amplitude harmonic bands on the time-frequency plots.

The data recorded by the surface spread could be considered as resulting from two separate sources, one being the orbital vibrator itself, and the other being the vibrating helical pile.

Examining the amplitude spectra for both the accelerometer and the pilot trace (Figure 5-33) may help explain this phenomenon. The source accelerometer spectrum exhibits a quasi-quadratic increase in amplitude up to the maximum amplitude at the maximum frequency of 100 Hz, with a high-amplitude spike observed at approximately 30 Hz. However, the pilot trace spectrum is contaminated by lower-frequency spikes, potentially supporting the theory of a “secondary source”. A spike in amplitude is observed on the pilot trace spectrum at approximately 100 Hz. By overlaying the accelerometer spectrum on the pilot trace spectrum and aligning the amplitudes of the 100 Hz spikes (Figure 5-34), it could potentially be argued that the spectrum of the pilot trace represents a combination of the spectra of two distinct sources.

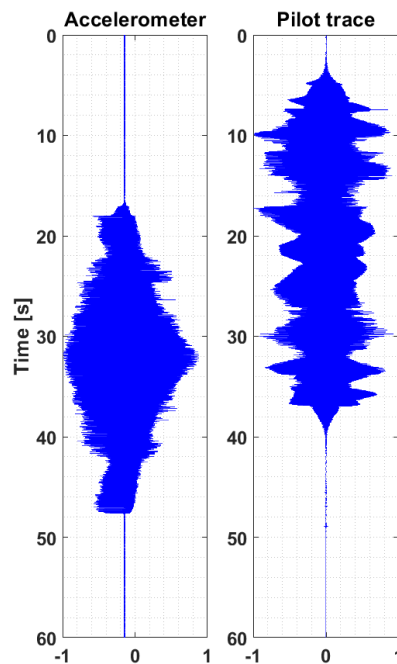


Figure 5-31: Uncorrelated traces from large surface linear vibrator tests. Source accelerometer (left) and pilot trace (right) shown.

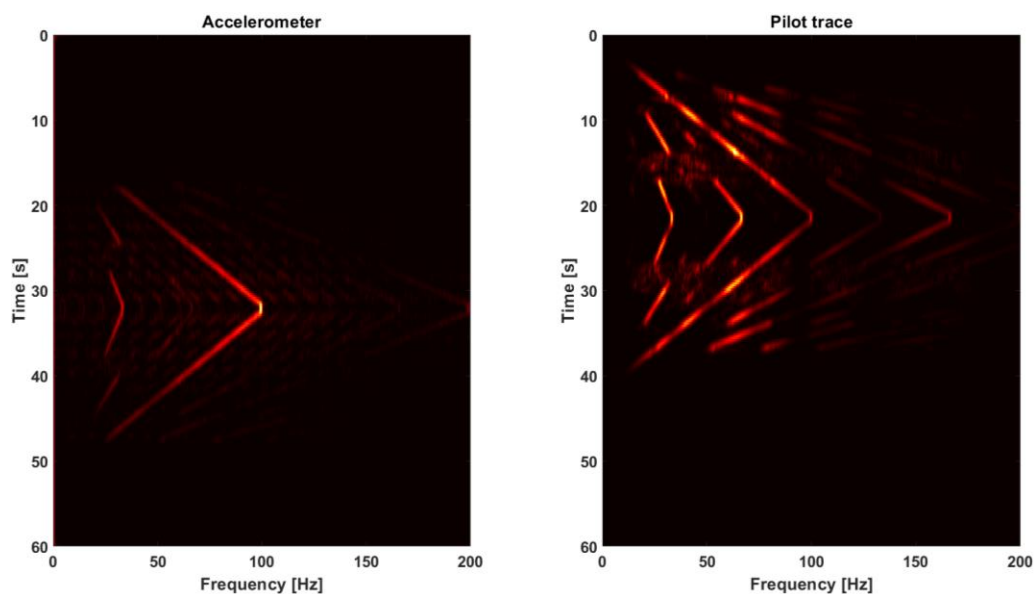


Figure 5-32: Time-frequency plots from large surface linear vibrator accelerometer (left) and surface geophone pilot trace (right).

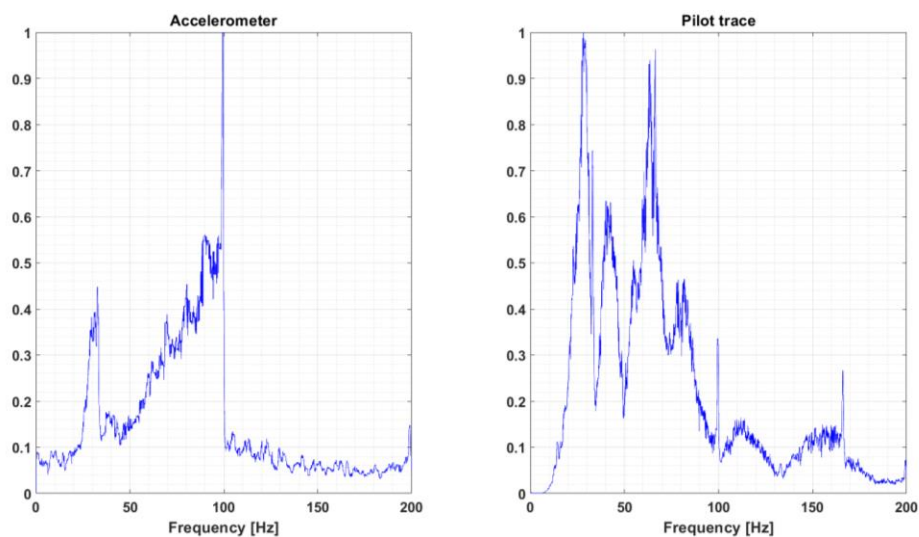


Figure 5-33: Normalized amplitude spectra from large surface linear vibrator accelerometer (left) and surface geophone pilot trace (right).

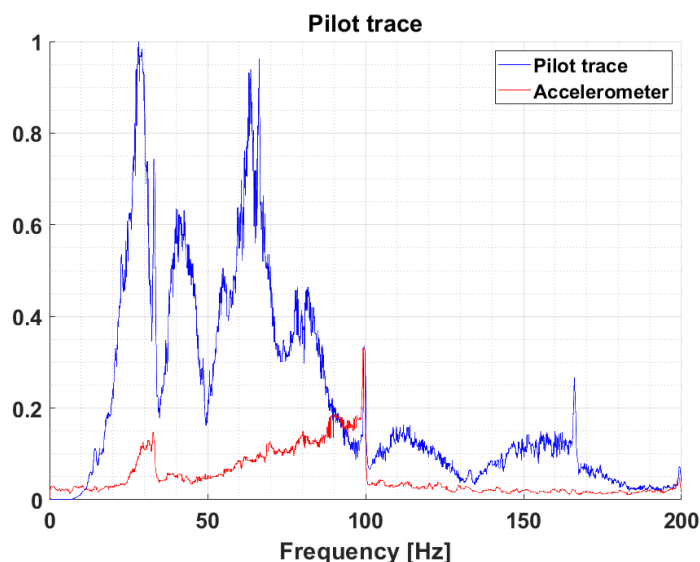


Figure 5-34: Amplitude spectrum from geophone pilot trace during large surface linear vibrator testing (blue) with source accelerometer amplitude spectrum overlain.

In Vibroseis acquisition, recorded data are cross-correlated with the sweep signature to remove the overprint of the wavelet. It has also been shown that, for borehole linear vibrator data, correlating raw data with a pilot trace may produce reliable datasets, provided a deconvolution algorithm is applied post-correlation to remove pervasive ringy character in the data. Correlating data from the surface spread of geophones acquired during testing of the large surface linear vibrator appears to support correlating with a pilot trace. In fact, correlating the data with a pilot trace (Figure 5-35) appears to produce superior results than correlating with a source accelerometer measurement (Figure 5-36). While still quite ringy, by correlating with a pilot trace, the first breaks can roughly be identified on the shot record, along with air blast and primary reflections (Figure 5-37). Correlating with the pilot trace may actually be preferred, as the spread of geophones will record the source signature as well as the vibration of the helical pile, while the accelerometer does

not record the pile vibration. Therefore, the pilot trace may more accurately represent the total source signature that is actually being emitted into the subsurface.

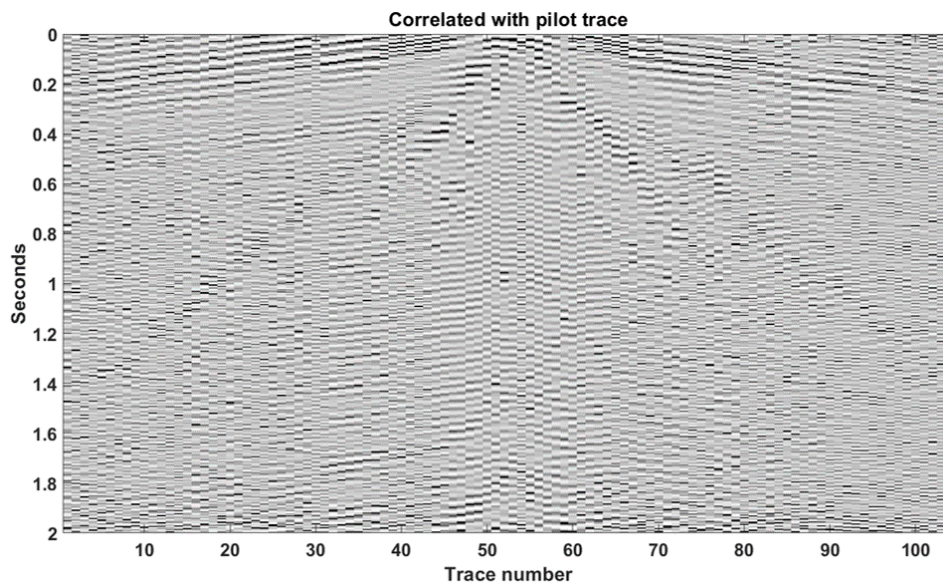


Figure 5-35: Surface spread of geophones correlated with large surface linear vibrator pilot trace.

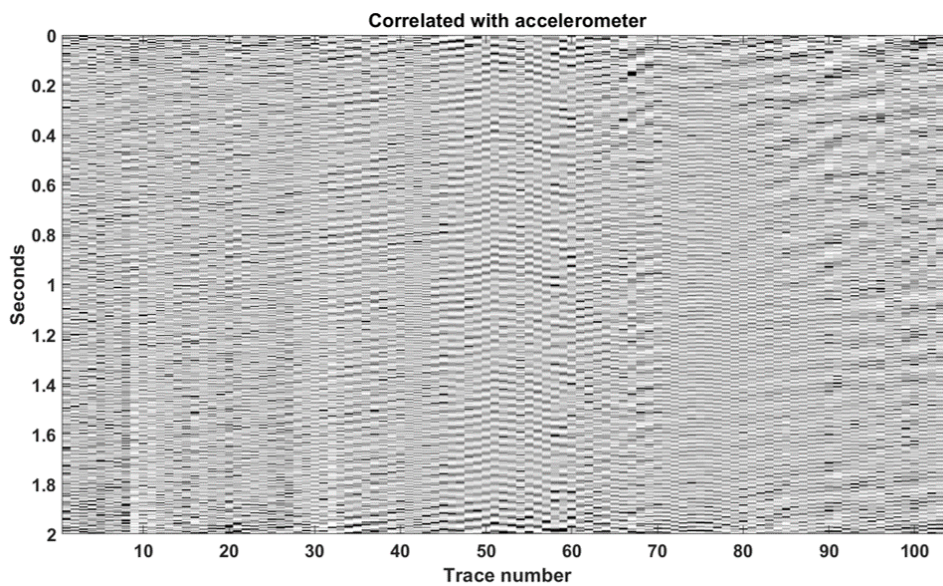


Figure 5-36: Surface spread of geophones correlated with large surface linear vibrator accelerometer recording.

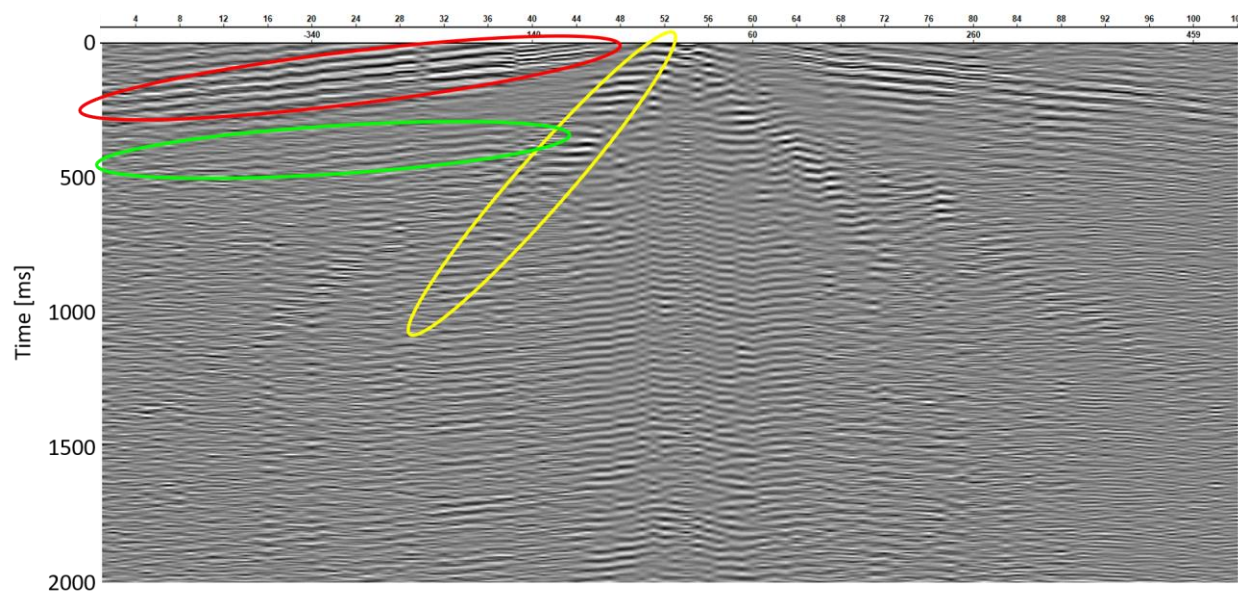


Figure 5-37: Surface spread of geophones correlated with large surface linear vibrator pilot trace. Approximate locations of first breaks (red), air blast (yellow), and primary reflections (green) identified.

Chapter 6 – Conclusions

To mitigate the negative consequences of anthropogenic global climate change, emissions of CO₂ into the atmosphere must be reduced. Carbon capture and sequestration can be an effective tool to contribute to achieving this goal and represents 7% of the total reduction in emissions required to achieve the Sustainable Development Scenario proposed by the International Energy Agency (International Energy Agency, 2018a). Time-lapse seismic surveys have been demonstrated to be a powerful tool for studying how subsurface reservoirs change in response to some stimulus, including in carbon sequestration projects. To improve upon existing time-lapse surveys, data must be acquired rapidly and with high repeatability measures in order to understand the migration and conformance of injected CO₂. A novel orbital vibrator seismic source has been developed to make these improvements and was deployed and tested at the Containment and Monitoring Institute's Field Research Station.

6.1 Observations from Baseline Data

In May and July 2017, baseline seismic datasets were acquired at the CaMI FRS using both a 2D surface line and VSP receiver geometries and a Vibroseis source. Multicomponent geophones and DAS fibre were used as the receivers, and data from each receiver type were compared. Vibroseis source locations for VSP datasets were selected to approximate the offset between the proposed locations of orbital vibrators and the observation wells at the site. Estimating the signal-to-noise ratio of geophone and DAS VSP data from the same source location demonstrated one of the inherent disadvantages of using fibre data. The geophone data exhibited an SNR estimate approximately 13 times greater than for the DAS data. However, DAS data offers much denser output trace spacing compared to typical geophones as receivers.

A VSP data processing workflow was developed using data from geophone receivers, resulting in a corridor stack that exhibits very similar character to zero-offset synthetic seismograms derived from the injector well logs. Applying the same workflow, with some modifications, to DAS data results in a corridor stack that compares well with both the geophone corridor stack and the synthetic seismogram.

As the orbital vibrator sources installed at the CaMI FRS rely on the power of stacking the results of several sweeps to increase the SNR in recorded data, the impact of increasing the source effort of DAS data was examined. It was found that, for the same source-receiver offset, increasing the number of Vibroseis sweeps from 3 to 10 increased the SNR estimate from approximately 2.5 to 10.2. Additionally, picking first break times became much simpler, and reflections in the raw shot record were much more apparent.

6.2 Permanent Source Results

Initial tests of the borehole source were encouraging, in spite of the source accelerometer failing. A trace from a surface geophone nearest the source borehole was used to approximate the source signature. The amplitude spectrum was computed for each of the five test sweeps, and three different model types were fit to the envelope of the spectra. It was found that a quadratic model best fit the amplitude spectrum for each of the traces, confirming the theoretical quadratic relationship between amplitude and frequency for orbital vibrator sources. Additionally, the time-frequency spectra of both the pilot traces and the surface geophones for each of the test sweeps accurately reflect the sweep parameters supplied to the system. Due to the absence of a source accelerometer reading, the pilot trace was used to correlate the raw data. The resultant shot records are contaminated by a ringy character, which was mitigated by deconvolution. Several

deconvolution algorithms were tested, including a deterministic deconvolution using the pilot trace, Wiener deconvolution, and Gabor deconvolution. It was found that Wiener and Gabor deconvolution outperformed the other algorithms when applied to the pilot trace, and Gabor deconvolution was superior to Wiener deconvolution when applied to correlated shot records. Deconvolved corridor stacks from the borehole vibrator source were comparable to Vibroseis corridor stacks at similar source offset from the well.

Testing of the large surface linear vibrator in September 2018 indicates that while the source accurately transfers the intended signature to near-offset receivers, the signature dissipates rapidly with offset. The source accelerometer of this source was functional, and the resultant measurements indicate significant coupling issues with the current source deployment. The trace from the source accelerometer exhibits a quasi-quadratic increase in amplitude with frequency, while the pilot trace is extremely notchy and asymmetrical. The pilot trace time-frequency plot is contaminated by high-amplitude noise, believed to be harmonics from the steel pile upon which the source is mounted. These harmonics are of extremely low amplitude on the time-frequency plot for the accelerometer. It is believed that the pile is acting as a secondary source, with vibrations between segments in the pile dominating the vibrator source signature.

- The source signature supplied to the borehole linear vibrator is captured by a surface spread of geophones, proven by the time-frequency plots of the surface geophone spread.
- The quadratic dependence of the source amplitude on the angular frequency of the rotating mass is confirmed by the superior R^2 value for quadratic models fit to borehole linear vibrator traces.
- In the absence of source accelerometer measurements, linear vibrator data can be correlated with a surface geophone pilot trace to generate usable datasets.

- The application of Gabor deconvolution to correlated datasets serves to reduce the “ringy” character present. Further improvement is expected by employing a source-signature deterministic deconvolution using the source accelerometer reading.
- The large surface linear vibrator may lack enough power to adequately transfer the source signature to receivers at large offsets.
- The current pile deployment for surface linear vibrators acts as a secondary source due to the vibration between pile segments. A new type of pile is expected to mitigate this problem.
- Generally, permanently-installed linear vibrator sources show promise for the rapid acquisition of time-lapse seismic surveys. However, more work is needed to improve the deployment of the sources and to fine-tune data processing workflows.

6.3 Future Work

One modification that could improve the operation of the orbital vibrator system is greater control over the time-frequency relationship supplied to the VFD system. Currently, the user selects four points in time-frequency space to create the sweep. Allowing for more points to be used in the time-frequency relationship could allow for improved low frequency content in the amplitude spectra by spending more time in low frequency ranges, similar to the ACROSS system.

The vibration of the segments of the helical pile represents a major hurdle in the use of surface linear vibrators when the pile segments are bolted together, as this vibration contaminates the sweep signature transmitted by the source. To attempt to mitigate this effect, a new pile was installed in early 2019. The segments of this pile have a screw threading, likely improving the coupling between the segments. As of the writing of this thesis, the surface linear vibrator has not

yet been tested using this new pile. New datasets acquired with a source mounted on this pile should be compared with existing datasets to determine if the type of pile deployed is the cause of the severe ringiness in the data and harmonics on the time-frequency plots.

The main theoretical advantage of deploying linear vibrator sources is to stack a large number of records together to improve the SNR. As shown with initial borehole vibrator tests, recorded data must be correlated and deconvolved prior to further processing. Based on the results of adding the stacking process to this pre-processing workflow, it is unclear in what order to apply these steps. It appears that correlating raw records, followed by deconvolution and stacking produces the best result; however, the stacked shot record is still quite ringy. In Vibroseis acquisition, uncorrelated records are first stacked, then correlated with the sweep signature. The pre-processing workflow should be re-examined and should likely resemble workflows for Vibroseis data.

After source deployment and data pre-processing has been improved, the linear vibrator sources should be tested using DAS fibre as the receiver. It has been demonstrated in this project and in the literature that increasing the source effort causes an increase in the SNR for DAS data. Deploying linear vibrators in conjunction with DAS should result in rapidly-acquired, densely-sampled datasets with high SNR.

References

- Arts, R., Chadwick, A., Eiken, O., Thibeau, S., & Nooner, S. (2008). Ten years' experience of monitoring CO₂ injection in the Utsira Sand at Sleipner offshore Norway. *First Break*, 26(1), 65–72.
- Bianchi, T., Forgues, E., Meunier, J., Huguet, F., & Bruneau, J. (2004). Acquisition and Processing Challenges in Continuous Active Reservoir Monitoring. *SEG Annual Meeting Expanded Abstracts*, 1–4.
- Byerley, G., Monk, D., Aaron, P., & Yates, M. (2018). Time-lapse seismic monitoring of individual hydraulic frac stages using a downhole DAS array. *The Leading Edge*, 37(11), 802–810. <https://doi.org/10.1190/tle37110802.1>
- CGG. (2008). *Continuous High-Resolution Reservoir Monitoring* (pp. 1–2). pp. 1–2.
- Chander, R. (1976). Seismic-ray tracing. *Physics Education*, 11, 365–370.
- CO₂CRC. (2019). Otway Research Facility. Retrieved from <http://www.co2crc.com.au/otway-research-facility-2/>
- Containment and Monitoring Institute. (2019). Projects. Retrieved from <http://www.cmcghg.com/cami/projects/>
- Correa, J., Freifeld, B. M., Revzner, R., Wood, T., Tertyshnikov, K., & Bona, A. (2018). Continuous DAS VSP monitoring using surface orbital vibrators : field trials for optimal configuration at the CO₂CRC Otway Project CO₂CRC Otway Project. *80th EAGE Conference and Exhibition 2018*, (June 2018).
- Cotton, J., Forgues, E., & Hornman, J. C. (2012). Land Seismic Reservoir Monitoring: Where is the steam going? *SEG Annual Meeting Expanded Abstracts*, 1–5. <https://doi.org/10.1190/segam2012-1539.1>
- CREWES. (2011). Research Facilities. Retrieved from https://www.crewes.org/About_CREWES/Research_Facilities/
- Daley, T. M., & Cox, D. (2001). Orbital vibrator seismic source for simultaneous P - and S - wave crosswell acquisition. *Geophysics*, 66(5), 1471–1480. <https://doi.org/10.1190/1.1487092>
- Dou, S., Pevzner, R., Ajo-Franklin, J., Daley, T., Robertson, M., Wood, T., ... Freifeld, B. (2016). Surface orbital vibrator (SOV) and fiber-optic DAS: Field demonstration of

- economical, continuous-land seismic time-lapse monitoring from the Australian CO₂ CRC Otway site. *SEG Annual Meeting Expanded Abstracts*, 5552–5556.
<https://doi.org/10.1190/segam2016-13974161.1>
- Eaid, M., Li, J., & Innanen, K. (2017). A coupled DAS shaped-fibre and 3D elastic finite difference wave model. *CREWES Research Report*, 29, 12.1-12.19.
- Eiken, O., Ringrose, P., Hermanrud, C., Bamshad, N., Torp, T. A., & Høier, L. (2011). Lessons Learned from 14 years of CCS Operations: Sleipner, In Salah and Snøhvit. *Energy Procedia*, 4, 5541–5548. <https://doi.org/10.1016/j.egypro.2011.02.541>
- Encyclopaedia Britannica. (2018). Piezoelectricity. Retrieved from <https://www.britannica.com/science/piezoelectricity>
- EPGeology. (2014). Well Shoot and Vertical Seismic Profile (VSP) Examples. Retrieved from http://www.epgeology.com/gallery/image_page.php?album_id=4&image_id=116
- Freifeld, B. M., Pevzner, R., Dou, S., Correa, J., Daley, T. M., Robertson, M., ... Gurevich, B. (2016). The CO₂CRC Otway Project deployment of a Distributed Acoustic Sensing Network Coupled with Permanent Rotary Sources. *78th EAGE Conference and Exhibition 2016*, (June), 2–6. <https://doi.org/10.3997/2214-4609.201600577>
- Furre, A.-K., Eiken, O., Alnes, H., Vevatne, J. N., & Kiær, A. F. (2017). 20 Years of Monitoring CO₂-injection at Sleipner. *Energy Procedia*, 114(November 2016), 3916–3926.
<https://doi.org/10.1016/j.egypro.2017.03.1523>
- Google. (n.d.). Map of Alberta showing Calgary, Brooks, and the FRS. Retrieved from maps.google.ca
- Gordon, A., & Lawton, D. C. (2018). Walk away VSP processing of DAS and geophone data at CaMI Field Research Station, Newell County, Alberta. *CREWES Research Report*, 30, 12.1-12.22.
- Gordon, A., Lawton, D. C., & Eaton, D. (2016). VSP Azimuthal Travel Time Analysis at the Field Research Station near Brooks, AB. *CREWES Research Report*, 28, 25.1-25.20.
<https://doi.org/10.3997/2214-4609.201701943>
- Government of Canada. (2016). The Paris Agreement. Retrieved from <https://www.canada.ca/en/environment-climate-change/services/climate-change/paris-agreement.html>

- Hall, K. W., Bertram, K. L., Bertram, M., Innanen, K., & Lawton, D. C. (2018). CREWES 2018 multi-azimuth walk-away VSP field experiment. *CREWES Research Report*, 30, 16.1-16.14.
- Hall, K. W., Lawton, D. C., Daley, T., Freifeld, B., & Cook, P. (2017). Source distance and source effort on DAS data. *CREWES Research Report*, 29, 26.1-26.15.
- Hornman, J. C., Mateeva, A., Potters, J. H. H. M., & Lopez, J. L. (2015). New Concepts for lowering the Cost of frequent seismic Reservoir monitoring onshore. *SEG Annual Meeting Expanded Abstracts*, 5518–5522. <https://doi.org/10.1190/segam2015-5826463.1>
- Huang, F., Bergmann, P., Juhlin, C., Ivandic, M., Lüth, S., Ivanova, A., ... Zhang, F. (2018). The first post-injection seismic monitor survey at the Ketzin pilot CO₂ storage site: results from time-lapse analysis. *Geophysical Prospecting*, 66(1), 62–84. <https://doi.org/10.1111/1365-2478.12497>
- Innanen, K., Lawton, D., Hall, K. W., Bertram, K. L., Bertram, M., & Bland, H. (2018). Design and deployment of a prototype multicomponent DAS sensor. *CREWES Research Report*, 30, 23.1-23.18.
- International Energy Agency. (2018a). Carbon capture, utilisation and storage. Retrieved from <https://www.iea.org/topics/carbon-capture-and-storage/>
- International Energy Agency. (2018b). World Energy Outlook 2018. Retrieved from <https://www.iea.org/weo2018/>
- IPCC. (2013). *Climate Change 2013: The Physical Science Basis. Contribution of Working Group I to the Fifth Assessment Report of the Intergovernmental Panel on Climate Change*. Retrieved from <https://www.ipcc.ch/report/ar5/wg1/>
- IPCC. (2018). Special Report: Global Warming of 1.5C - Summary for Policymakers. Retrieved from <https://www.ipcc.ch/sr15/chapter/summary-for-policy-makers/>
- Isaac, J. H., & Lawton, D. C. (2014a). Preparing for experimental CO₂ injection: Geology of the site. *CREWES Research Report*, 26, 42.1-42.9. Retrieved from www.cmcghg.com
- Isaac, J. H., & Lawton, D. C. (2014b). Preparing for experimental CO₂ injection: Seismic data analysis. *CREWES Research Report*, 26, 43.1-43.8.
- Kasahara, J., & Hasada, Y. (2017). *Time Lapse Approach to Monitoring Oil, Gas, and CO₂ Storage by Seismic Methods*. Cambridge, MA: Elsevier.

- Kragh, E., & Christie, P. (2002). Seismic repeatability, normalized rms, and predictability. *The Leading Edge*, 21(7), 640–647.
- Kuvshinov, B. N. (2016). Interaction of helically wound fibre-optic cables with plane seismic waves. *Geophysical Prospecting*, 64(3), 671–688. <https://doi.org/10.1111/1365-2478.12303>
- La Follett, J. R., Wills, P., Lopez, J. L., Przybysz-Jarnut, J. K., & van Lokven, M. (2015). Continuous seismic reservoir monitoring at Peace River: Initial results and interpretation. *SEG Annual Meeting Expanded Abstracts*, 5440–5444. <https://doi.org/10.1190/segam2015-5883275.1>
- Lawton, D. C., Osadetz, K. G., & Saeedfar, A. (2017). Monitoring technology innovation at the CaMI Field Research Station, Brooks, Alberta. *GeoConvention Expanded Abstracts*, 1–4. <https://doi.org/10.3997/2214-4609.201701930>
- Lawton, D., Osadetz, K. G., & Saeedfar, A. (2016). *CaMI Field Research Station*.
- Li, G. (2003). Time-Lapse (4-D) Seismic Monitoring of Massive CO₂ Flood at Weyburn Field, S.E. Saskatchewan. *GeoConvention Expanded Abstracts*.
- Lines, L. R., & Newrick, R. T. (2004). *Fundamentals of Geophysical Exploration*. Tulsa, OK: Society of Exploration Geophysicists.
- Liu, E., Crampin, S., & Queen, J. H. (1991). Fracture detection using crosshole surveys and reverse vertical seismic profiles at the Conoco Borehole Test Facility, Oklahoma. *Geophysical Journal International*, 107(3), 449–463. <https://doi.org/10.1111/j.1365-246X.1991.tb01406.x>
- Macquet, M., & Lawton, D. C. (2017). Reservoir simulations and feasibility study for seismic monitoring at CaMI.FRS. *CREWES Research Report*, 29, 56.1-56.26.
- Macquet, M., Lawton, D. C., Dongas, J., & Barraza, J. (2016). Feasibility study of time-lapse seismic monitoring of CO₂ sequestration. *CREWES Research Report*, 28, 49.1-49.15.
- Margrave, G. F. (2013). *Methods of Seismic Data Processing*.
- Mateeva, A., Lopez, J., Mestayer, J., Wills, P., Cox, B., Kiyashchenko, D., ... Grandi, S. (2013). Distributed acoustic sensing for reservoir monitoring with VSP. *The Leading Edge*, 32(10), 1278–1283.
- Molenaar, M. M., Hill, D., Webster, P., Fidan, E., & Birch, B. (2012). First Downhole Application of Distributed Acoustic Sensing for Hydraulic-Fracturing Monitoring and

- Diagnosics. *SPE Drilling & Completion*, 27(01), 32–38. <https://doi.org/10.2118/140561-pa>
- Nakatsukasa, M., Ban, H., Kato, A., Shimoda, N., White, D., & Nickel, E. (2018). VSP acquisition with combined fiber-optic DAS and permanent seismic source ACROSS for permanent reservoir monitoring at the Aquistore site. *SEG Annual Meeting Expanded Abstracts*, 5273–5277. <https://doi.org/10.1190/segam2018-2995929.1>
- Queißer, M., & Singh, S. C. (2013). Full waveform inversion in the time lapse mode applied to CO2 storage at Sleipner. *Geophysical Prospecting*, 61(3), 537–555. <https://doi.org/10.1111/j.1365-2478.2012.01072.x>
- Schlumberger. (2019). Oilfield Glossary. Retrieved from <https://www.glossary.oilfield.slb.com/>
- Stanton, A. N. (1931). *Patent No. US1790080A*. Retrieved from <https://patents.google.com/patent/US1790080A/en>
- Stewart, R. R. (2001). VSP: An In-Depth Seismic Understanding. *CSEG Recorder*, 26(7), 79–83. Retrieved from <http://www.cseg.ca/publications/recorder/2001/09sep/sep01-vsp.pdf%5Cnpapers://8a7341e4-9daa-4c0d-bcf2-2d9b813974af/Paper/p9828>
- Takanashi, M., Kato, A., & Kasahara, J. (2014). Towards a new approach for time-lapse seismic using permanent seismic source ACROSS and elastic full waveform inversion. *SEG Annual Meeting Expanded Abstracts*, 4863–4867.
- Weisstein, E. W. (n.d.). Gibbs Phenomenon. Retrieved from MathWorld--A Wolfram Web Resource website: <http://mathworld.wolfram.com/GibbsPhenomenon.html>
- Wilkinson, H. (2017). *Automated High Power Permanent Borehole Seismic Source Systems for Long-Term Monitoring of Subsurface CO2 Containment and Storage*.
- Yang, W. (2003). *A Basical Study on Two-point Seismic Ray Tracing* (pp. 1–8). pp. 1–8. Retrieved from <http://www.ees.nmt.edu/outside/courses/GEOP523/Docs/yang.pdf>
- Young, H. D., & Freedman, R. A. (2008). *University Physics with Modern Physics*. San Francisco: Pearson Addison Wesley.
- Zhang, H., & Brown, R. J. (2001). A review of AVO analysis. *CREWES Research Report*, 13(1), 357–380.